NMR STUDIES OF SUPERCRITICAL CO_2 IN CARBON SEQUESTRATION AND IMMISCIBLE TWO PHASE FLOW IN POROUS MEDIA

by

Cody Allen Prather

A thesis submitted in partial fulfillment
of the requirements for the degree

of

Master of Science

in

Mechanical Engineering

MONTANA STATE UNIVERSITY
Bozeman, Montana

May 2015

©COPYRIGHT

by

Cody Allen Prather

2015

All Rights Reserved

ACKNOWLEDGEMENTS

I would like to acknowledge my family for their unwavering support and encouragement and my wife, Kyllie Smith, for being there every step of the way. I would also like to thank my colleagues within the MRM lab for their advice, assistance, and friendship. Finally, I would like to recognize my mentors, Dr. Sarah Codd and Dr. Joseph Seymour, for giving me such a wonderful opportunity and for their exceptional guidance and scientific inspirations.

TABLE OF CONTENTS

1. INTRODUCTION AND BACKGROUND 1

Trapping Mechanisms 2
Solubility Trapping (Viscous Fingering Phenomena) 4
Capillary Trapping 5

2. NUCLEAR MAGNETIC RESONANCE THEORY 8

Introduction to Nuclear Magnetic Resonance (NMR) 8
Spin Physics 8
Excitation 10
Laboratory Frame of Reference 11
Rotating Frame of Reference 12
Detection 14
Faraday's Law of Induction 14
Fourier Transforms 15
Quadrature Detection 17
Discrete Fourier Transform 20
Relaxation 20
Longitudinal Relaxation 20
Transverse Relaxation 21
Bloch Equations 25
Basic Pulse Sequences and Spin Manipulation 25
Signal Averaging 25
Phase Cycling 26
Spin Echo 28
CPMG 29
Inversion Recovery 30
Gradients and K-space 31
Gradients 31
K-space 33
ZTE 37
Selective Excitation 38
Translational Motion 40
PGSE 44
Q-Space and Propagators 46

3. ZTE SEQUENCE OPTIMIZATION 51

Introduction 51
Parameter Manipulation 52
Image Reconstruction and Analysis 55

TABLE OF CONTENTS - CONTINUED

Phantom Resolution Experiments 56
Introduction 56
Experimental Setup and Procedure 56
Results and Discussion 57
Conclusions 60

4. T1 AND T2 PRESSURE DEPENDENCE STUDY 61

Introduction 61
Experimental Setup and Procedure 61
Setup 61
Procedure 63
Pulse Sequences 63
Results and Discussion 64
Conclusions 66

5. VISCOUS FINGERING EXPERIMENTS 67

Introduction 67
Experimental Setup and Procedure 68
Setup 68
Procedure 69
Pulse Sequences 71
Results and Discussion 73
Imaging of CO_2 Pulse through Saturated Rock Core 73
Viscous Fingering Experiment 75
Conclusions and Future Work 81

6. CAPILLARY TRAPPING EXPERIMENTS 83

Introduction 83
Experimental Setup and Procedure 83
Setup 83
Procedure 85
Pulse Sequences 87
Results and Discussion 88
AFLAS and FEP Sleeves 88
ZTE Data 91
T2 Distribution Data 99
5mm Core T2 Distribution Data 103
Conclusions and Future Work 105
Future Work 106

TABLE OF CONTENTS - CONTINUED

7. TWO PHASE FLOW EXPERIMENT 108

Introduction 108
Experimental Setup and Procedure 110
Setup 110
Procedure 111
Pulse Sequences 111
Results and Discussion 113
NMR Data 116
Conclusions and Future Work 123
Future Work 123

REFERENCES CITED 125

APPENDICES 129

APPENDIX A: ZTE Optimization Data 130
APPENDIX B: T1 and T2 Pressure Dependence Data 133
APPENDIX C: Viscous Fingering Data 136
APPENDIX D: Capillary Trapping Data 140
APPENDIX E: Two Phase Flow Data 164

LIST OF FIGURES

Figure Page

1: CO_2 emissions from fossil fuels 2

2: Stratigraphic trapping 3

3: Viscous fingering regimes and numerical simulation reproduced from [12] 5

4: Residually trapped CO_2 in rock pores 7

5: Nuclei angular momentum and precession 9

6: Spin state distribution 10

7: Evolution of magnetization (lab reference frame) 12

8: Evolution of magnetization (rotating reference frame) 13

9: Electromagnetic induction in a solenoid 14

10: Precession of magnetization in solenoid 15

11: FT addition theorem 16

12: Quadrature detection scheme 17

13: Real and imaginary signal and spectrum 19

14: Longitudinal relaxation 21

15: Transverse relaxation 22

16: Relaxation vs. molecular tumbling rate 23

17: Phase cycling representation 27

18: Spin-echo sequence and spin manipulations 28

19: CPMG pulse sequence with echo envelope 29

LIST OF FIGURES - CONTINUED

Figure Page

20: Inversion recovery pulse sequence and spin manipulations 30

21: Tube of water with and without gradients applied 32

22: Evolution of spin phase under the application of a gradient..... 33

23: Pure 2D phase encoding sequence with k-space trajectory 35

24: Read and phase encoding 2D sequence with k-space trajectory 36

25: Three dimensional ZTE pulse sequence used in experiments 38

26: Linear magnetic field gradient with position dependent ω..... 40

27: Gradient echo sequence depicting the evolution of spins..... 41

28: Spin echo sequence with gradient pulses and effective gradient..... 42

29: Uncompensated (top) and compensated (bottom) gradients..... 44

30: PGSE sequence 45

31: Diffusion Propagator..... 49

32: Three dimensional ZTE pulse sequence with hard RF pulse..... 52

33: Background subtraction for ZTE images..... 56

34: Signal intensity vs. position for 3 rubber phantom samples 58

35: Signal intensity vs. position for 6.3mm phantom sample..... 58

36: Signal intensity vs. position for 3.15mm phantom sample..... 59

37: Signal intensity vs. position for 1.68mm phantom sample..... 59

38: Experimental setup for pressure dependence study..... 62

39: Pressure versus T_2 relaxation for doped DI H2O 65

LIST OF FIGURES - CONTINUED

Figure Page

40: Pressure versus T_1 relaxation for doped DI H2O 66

41: Experimental setup for viscous fingering experiment 68

42: Multi-slice multi-echo (MSME) pulse sequence 72

43: Expectation of 1D ZTE data for CO_2 pulse 74

44: 1D ZTE data for CO_2 front moving through rock core 74

45: 2D ZTE data for CO_2 front moving through rock core 75

46: Before and after images from pressure inversion incident 76

47: Relaxation map with red and blue lines indicating where T_2 progressions were taken from 77

48: T_2 1D average across length of sample for all 34 scans 78

49: T_2 progression of scans at position 18mm versus time 78

50: T_2 progression of scans at position 62mm versus time 79

51: 1D average signal intensity vs. position (MSME scans) 80

52: 1D average signal intensity vs. position (ZTE scans) 81

53: Experimental setup and cross section of core holder 84

54: T2 distribution comparisons between AFLAS and FEP 89

55: ZTE images of AFLAS time evolution reaction to CO_2 90

56: AFLAS sleeve failure 91

57: 1D profiles indicating W phase along rock core length (air/H_2O) 92

LIST OF FIGURES - CONTINUED

Figure Page

58: 1D profiles indicating W phase along rock core length (CO_2/ H_2O) 93

59: 1D profiles indicating W phase along rock core length ($scCO_2$/ H_2O) 93

60: NW phase initial vs. NW phase residual 99

61: Illustration for defining larger and smaller pores associated with transverse relaxation times 100

62: T_2 distribution evolution for drainage/imbibition of air/water at 75.86bar and ambient temperature 101

63: T_2 distribution evolution for drainage/imbibition of CO_2/water at 75.86bar and ambient temperature 101

64: T_2 distribution evolution for drainage/imbibition of $scCO_2$/water at 75.86bar and 35^oC 102

65: T2 distribution comparison of 5mm and 27mm cores 104

66: Immiscible two phase flow regimes: (a) Bubbly (b) Slug (c) Froth (d) Annular (e) Dispersed 109

67: Two phase flow setup diagram 111

68: Example of pressure drop acquisition and steady state (SS) region 113

69: Capillary number vs. pressure gradient (preliminary) 114

70: Capillary number vs. pressure gradient (recent) 115

71: FID data (pressure overlaid) for V = 0.595 ml/min 117

72: MSME data (pressure overlaid) for V = 0.595 ml/min 118

73: FID data (pressure overlaid) for V = 0.188 ml/min 121

LIST OF FIGURES - CONTINUED

Figure Page

74: MSME data (pressure overlaid) for V = 0.188 ml/min) 122

LIST OF TABLES

Table Page

1: Phantom FWHM comparison to actual thickness..... 60

2: Berea Sandstone Properties 85

3: Non-wetting phase fraction in Berea rock core #2 95

4: Non-wetting phase fraction in Berea rock core #3 95

5: Average NW phase fractions of all four runs of air, CO_2, and $scCO_2$..... 97

ABSTRACT

Nuclear magnetic resonance (NMR) was used to research mechanisms related to two-phase flow in porous media. Experiments were conducted to further understand; 1) the capillary trapping mechanism that occurs during sequestration of CO_2 in deep underground sandstone reservoirs, 2) the viscous fingering phenomena that occurs when $scCO_2$ convectively dissolves in brine under reservoir conditions, and 3) flow patterns and fluid mechanisms in immiscible two-phase flow in porous media for the two pressure gradient regimes formed under different capillary numbers.

Capillary trapping is a prominent mechanism for initially trapping CO_2 in pore structures of deep underground rock formations during the sequestration process. Because of its significant role in securing CO_2 underground, it is important to characterize and understand the residual saturation and distribution of CO_2 within the pore structure. A setup was developed in which drainage and imbibition of a Berea Sandstone core takes place within an NMR spectrometer under reservoir conditions. NMR results provide comparisons between the different nonwetting fluids used and help characterize the capillary trapping of each nonwetting fluid. In conclusion, $scCO_2$ is trapped 13% less efficiently than air or CO_2, and the nonwetting fluid is preferentially trapped in larger pores.

Viscous fingering is a significant long-term trapping mechanism that further increases storage security by enhancing mass transfer through convective dissolution. A setup was developed in which $scCO_2$ could dissolve into a water saturated bead pack, under reservoir conditions, within the NMR spectrometer. NMR results track spatial changes in T_2 relaxation time and signal intensity. The results are inconclusive and the phenomena could not be directly observed but results do suggest dissolution is occurring during the experiment.

Immiscible two-phase flow in porous media is unpredictable and existent in many industries. Therefore, determining flow patterns and understanding the fluid mechanisms from a capillary number/pressure gradient relationship could prove valuable. A setup was developed in which an immiscible two-phase flow through a bead pack was monitored, for different capillary numbers, with NMR techniques. NMR results provide snapshots of the water saturation distribution within the bead pack. The results suggest there’s a consistent slug-type flow pattern during the steady state.

1. INTRODUCTION AND BACKGROUND

This work presents research utilizing nuclear magnetic resonance (NMR) techniques to study a dynamic macroscopic system at a laboratory level. NMR is a versatile tool used to non-invasively study a wide variety of both static and dynamic systems in many areas of science and is most extensively used in the medical industry, known in the medical industry as magnetic resonance imaging (MRI). It finds its use in this thesis with its ability to image fluid transport in porous media in real time and to extract information regarding pore structure. The primary focus of this thesis is to study the trapping mechanisms of CO_2 when it is pumped into deep underground saline sandstone reservoirs for secure storage at supercritical conditions.

Anthropogenic CO_2 emissions are becoming increasingly prevalent in our society and the increase in atmospheric concentrations of this greenhouse gas are believed to contribute to the observed global warming [1]. Figure 1 illustrates the significant increases in the amount of CO_2 emissions from fossil fuels. A currently investigated viable means of reducing anthropogenic CO_2 emissions is through a method called carbon capture and storage (CCS) [2]. CCS is the process by which CO_2 is captured and securely stored in deep underground saline aquifers or in depleted oil and gas fields. When CO_2 is injected into these deep underground reservoirs it is stored in a supercritical state. That is, at temperatures and pressures above the critical point of CO_2. Supercritical fluids exhibit both properties of gases and liquids. It has transport properties comparable to gases and densities similar to liquids [3, 4]. Thus, CO_2 in its supercritical state will have a much larger storage capacity, it’s denser, than in its gaseous state while at the

same time enhancing mass transfer, it's more miscible, and is therefore ideal for geologic sequestration.

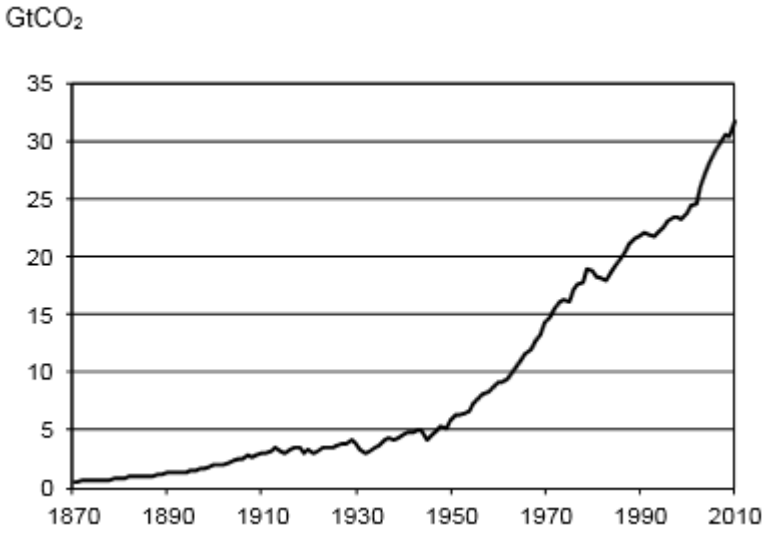


Figure 1: CO_2 emissions from fossil fuels[1]

Trapping Mechanisms

There are four dominant trapping mechanisms that contribute to the long term storage of CO_2: structural trapping (stratigraphic trapping), capillary trapping (residual trapping), solubility trapping and mineral trapping. Structural trapping is where the buoyant CO_2 plume becomes immobilized underneath an impermeable cap rock, essentially stopping the upward migration of the CO_2 plume from reaching the surface [5]. This is depicted in the following figure.

[1] http://www.iea.org/publications/freepublications/publication/CO2EmissionsFromFuelCombustionHighlights2013.pdf

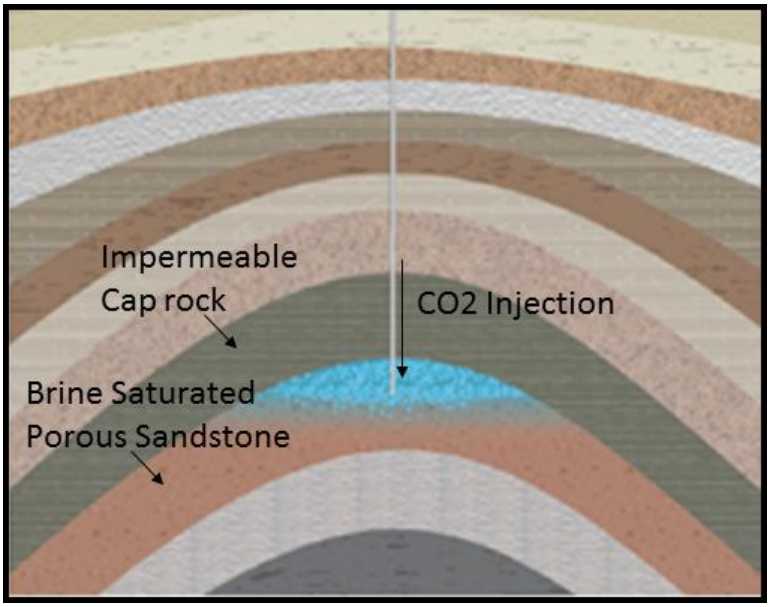


Figure 2: Stratigraphic trapping[2]

Capillary trapping is the mechanism that traps ganglia (tiny droplets of CO_2) within the pores of the rock. This happens primarily after injection stops at which point water begins to imbibe back into the CO_2 plume, immobilizing a fraction of the trailing end of the CO_2 plume [5-11]. Solubility trapping is the dissolution of the trapped CO_2 into the surrounding brine, a process that takes considerable time but lessens the amount of CO_2 that could migrate upwards due to buoyant forces [5, 12]. Lastly, mineral trapping happens when the dissolved CO_2 reacts with the minerals in the rock creating solid carbonate minerals that precipitate into the pores. This process has the longest time scale of all the other trapping mechanisms [5].

[2] http://www.co2crc.com.au/aboutccs/stor_trapping.html

Solubility Trapping (Viscous Fingering Phenomena)

This thesis focuses on two trapping mechanisms, the first being solubility trapping. Solubility trapping is the result of the residually trapped CO_2 dissolving into the surrounding brine, which further increases the storage security. After CO_2 has been pumped underground into the reservoir it begins to migrate upwards towards to cap rock due to a greater buoyancy than the brine. The CO_2 also begins to dissolve into the surrounding brine through processes of diffusion and dispersion. As this CO_2 dissolves into the brine it creates a denser layer that at some point becomes unstable and convective overturning occurs. This is called convective dissolution.

Figure 3 depicts this phenomena of convective dissolution in which downwelling and upwelling plumes are created, the so called viscous fingering, after the interface becomes unstable and saturated fingers begin to coalesce. These downwelling plumes of CO_2/brine are denser thus driving the plume downwards. This downward plume increases the surface area for dissolution thus enhancing the mass transfer, increasing the dissolution rate. This increase in the dissolution rate further ensures the storage security.

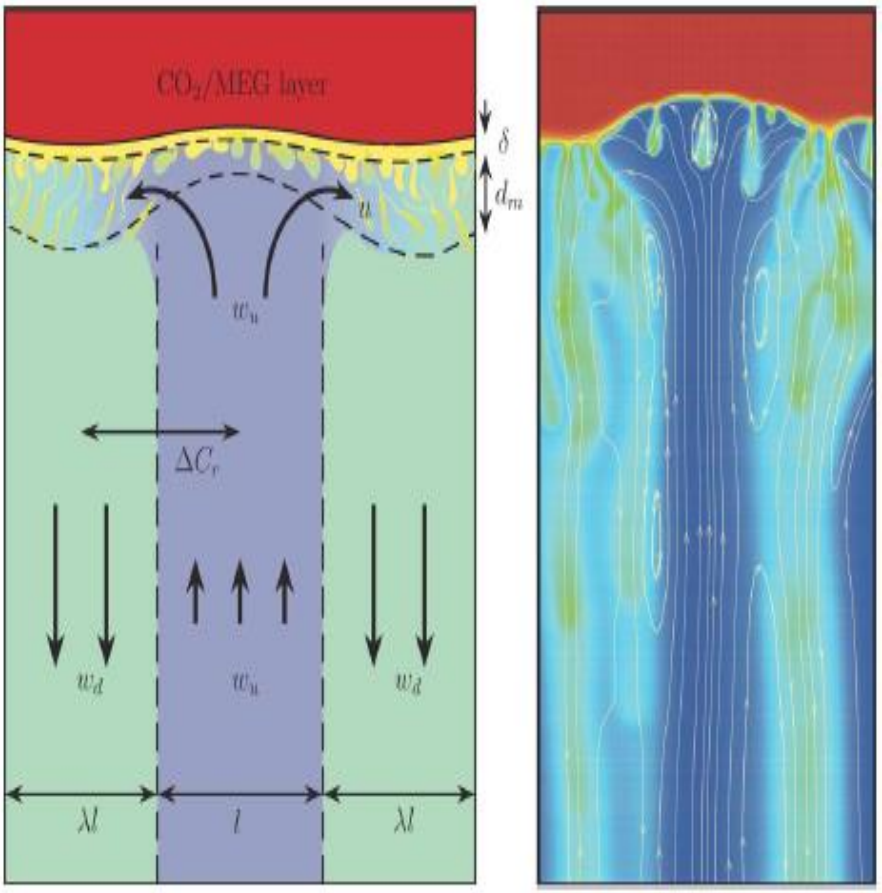


Figure 3: Viscous fingering regimes and numerical simulation reproduced from [12]

Capillary Trapping

Because solubility trapping and mineral trapping occur on long timescales and are dependent on the security and the amount of CO_2 trapped during the capillary trapping stage, it is therefore important to understand this mechanism and determine the residual saturation of CO_2 trapped within the pores in order to optimize CO_2 injection and trapping security. Hence, capillary trapping is the other focus of this thesis. CO_2 becomes trapped when the capillary forces are greater than the pressure gradient and buoyant forces, essentially when the surface tension is greater than the viscous forces. The capillary number is a dimensionless quantity that represents the ratio of viscous forces to capillary

forces, thus at low capillary numbers the trapping of CO_2 occurs. It is defined as equation [1 where μ is the dynamic viscosity, V is the superficial velocity, and γ is the surface tension.

$$Ca = \frac{\mu V}{\gamma} \quad [1]$$

In the case where CO_2 is the nonwetting (NW) phase in a deep sandstone saline aquifer, CO_2 ganglia are produced via snap-off at which point it becomes residually trapped [13]. This is depicted in Figure 4 when an upward migrating plume of CO_2 leaves behind residually trapped ganglia of CO_2 via snap-off. Snap-off is an important phenomena in geologic sequestration because it prevents the separated CO_2 ganglia from continuing to migrate upward with the rest of the plume, reducing the risk of leakage. Snap-off occurs in the pore throats, a constriction in the pathway, interconnecting larger pore bodies when a piston-like flow is not possible. Essentially, when the capillary pressure in the pore throat is greater than the capillary pressure across the NW phase front in the pore body, snap-off occurs and the NW phase becomes trapped within the pore body [13-15]. Once trapped the wetting phase fluid, brine in this case, is allowed to flow around the trapped bubble, indicated in the zoomed in portion of Figure 4.

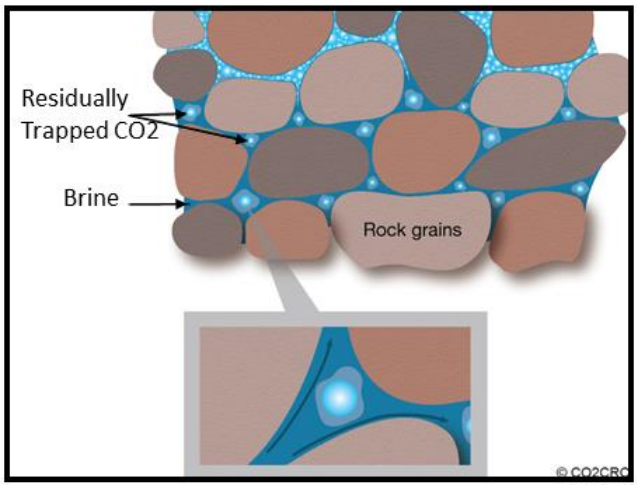


Figure 4: Residually trapped CO_2 in rock pores[3]

[3] http://www.co2crc.com.au/images/imagelibrary/stor_diag/residual-trapping_media.jpg

2. NUCLEAR MAGNETIC RESONANCE THEORY

Introduction to Nuclear Magnetic Resonance (NMR)

The first evidence of nuclear magnetic resonance was established in 1938 by Isador Rabi, who through the use of a molecular beam apparatus determined magnetic moments of nuclei utilizing an oscillating adjustable radio frequency field. NMR was further expanded by Felix Bloch and Edward Purcell in 1945 for the discovery of nuclear magnetic resonance in condensed matter, specifically for the hydrogen nuclei [16]. Nuclear magnetic resonance is the phenomena in which electromagnetic radiation is absorbed and emitted from nuclei when a weaker oscillating magnetic field is applied at a specific radio frequency in a primary static magnetic field. NMR has come a long way in the last 75 years and because of its noninvasive techniques has found application in many areas of science such as chemistry, fluid dynamics, geology, and most predominately in the medical industry, known as magnetic resonance imaging (MRI). This chapter will discuss the concepts of NMR and provide an understanding of the tool used in the experiments presented in this thesis. Most of the information found in this chapter was obtained from [16] where more detailed information can be found.

Spin Physics

Before understanding how nuclear magnetic resonance (NMR) works it is important to understand a little about the nuclear spins themselves. The entirety of NMR is built upon the interactions of the atomic nuclei within static and applied oscillating magnetic fields. This interaction requires the nuclei to possess a property called spin, or

angular momentum. Think of a hydrogen nuclei as our earth with the angular moment vector being the rotational axis with precession about another axis aligned with the magnetic field. Our hydrogen nuclei behaves in much the same way within a magnetic field, B_0, as shown in the figure below. As seen from the figure, this precession, or rotation, may be very hard to see if the angular momentum vector was aligned with the B_0 vector. In order to see this precession, a torque must be applied to the angular momentum vector rotating it away from the B_0 axis.

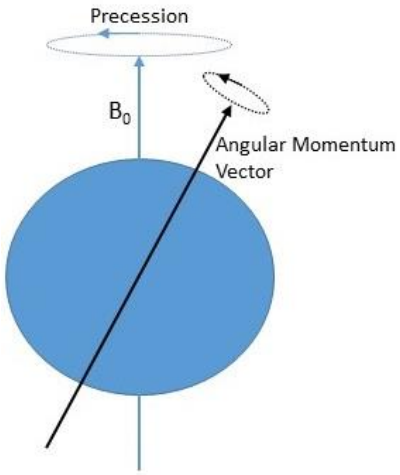


Figure 5: Nuclei angular momentum and precession

Spin is described by the angular momentum quantum number I. In the Stern-Gerlach experiment, nuclei's with I= ½ were found to reside in what is called spin up, ½, and spin down, -½, states. Nuclear spins impart magnet moments proportional to their angular momentum vector and spin state. When there are spins outside of a magnetic field their vectors are oriented randomly and the net magnetic field sums to zero. When a magnetic field is applied there will be a slight net magnetization along the direction of the applied magnetic field. Observing a hydrogen nucleus in the presence of a magnetic field,

it has these two possible energy states, spin up and spin down. Taking an ensemble of nuclei in thermal equilibrium within an applied magnetic field, there will be a distribution of spins in each energy state, given by the Boltzmann factor, with a slight preference for the lower energy, spin up state. This is shown in Figure 6. There will be a preferential net magnetization along the B_0 direction due to the spin excess in the lower energy state. It's this excess that is visible in NMR, all of the other spins will cancel out their magnetization.

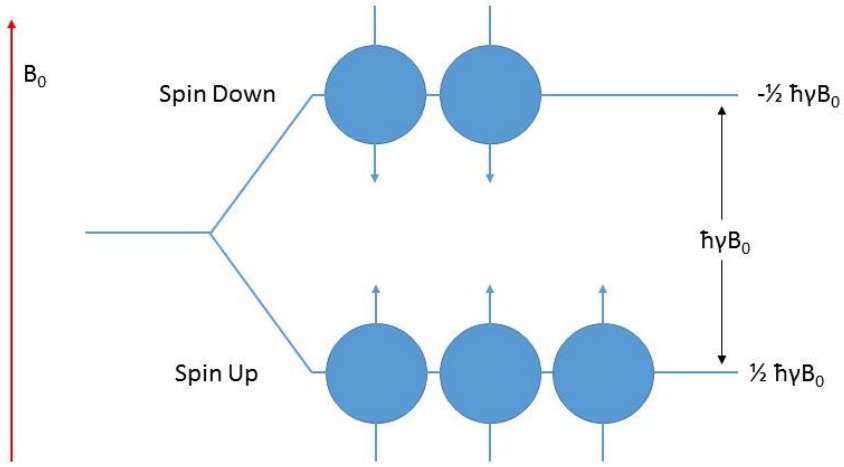


Figure 6: Spin state distribution

Excitation

In order to detect this net magnetization it must be perturbed from equilibrium into the transverse plane at which point the precession will be visible. It is this precession of net magnetization in the laboratory frame of reference that creates a signal to be detected. Before discussing the excitation and detection process, it is important to understand the evolution of nuclear spins under the application of specific magnetic fields and certain frames of reference in which they can be viewed.

Laboratory Frame of Reference

Starting from the laboratory frame of reference, the net magnetization of spins, as described by the magnetization vector M, will be in the direction of the applied static magnetic field, B_0. Even though the precession is not visible when the spins are aligned in the z-direction they are still precessing. This precession frequency is known as the Larmor frequency, ω_0. The Larmor frequency is a function of the gyromagnetic ratio, γ, and the static magnetic field. It is given by

$$\omega_0 = \gamma B_0 \qquad [2]$$

In order to tip the magnetization into the transverse plane a torque must be applied to the magnetization vector. This is achieved by applying a resonant RF magnetic field, B_1, perpendicular to the static B_0 field as well as the precessing magnetization vector. Therefore, B_1 must also be applied at the same resonant frequency as the precessional frequency of the spins, ω_0. The effect of this B_1 field is to cause the magnetization to nutate about the B_1 axis. Once the B_1 field is turned off, the spins now only experience the effect of the B_0 field, this is known as the Zeeman interaction, and are said to be in free precession, that is, they are simultaneously rotating about the B_0 field at their Larmor frequency while spiraling back to equilibrium along the direction of the static B_0 field. This is illustrated in Figure 7.

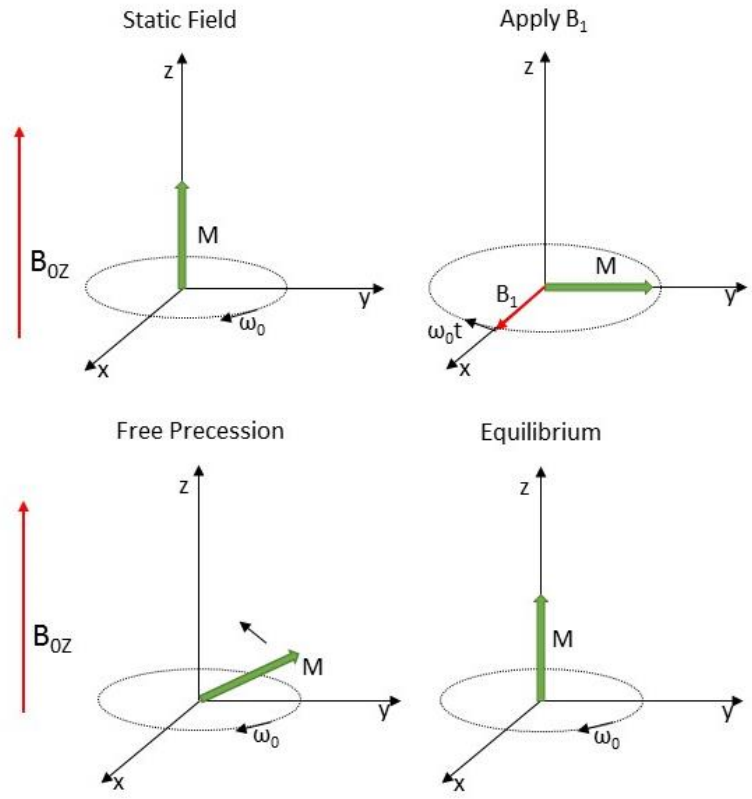


Figure 7: Evolution of magnetization (lab reference frame)

Rotating Frame of Reference

The rotating frame of reference, that is, the frame of reference in which the x and y axes are rotating about the z axis at the Larmor frequency, does two helpful things. It allows the evolution of the magnetization vector to visually be understood better as well as simplifying some mathematical equations. In this frame of reference the axes are rotating about the z axis at the Larmor frequency where effectively the longitudinal B_0 field is zero and the B_1 field appears stationary as long as everything is on resonance, that is, when $\omega = \omega_0$. This can be more clearly seen by looking at the Hamiltonian in the rotating frame of reference defined as

$$H_{rot} = -\gamma(B_0 - \omega/(\gamma)I_z - \gamma B_1 I_x) \quad [3]$$

Keeping in mind that $\omega_0 = \gamma B_0$, being on resonance, $\omega = \omega_0$, would eliminate the B_0 field from the equation and thus leave the effective B_1 field in the transverse x or y direction depending upon the application of the field. This simplifies the Figure 7 visualization to where the magnetization vector, M, appears not to precess, only nutating about the B_1 axis, and B_1 appears to remain stationary. This is illustrated in the following figure

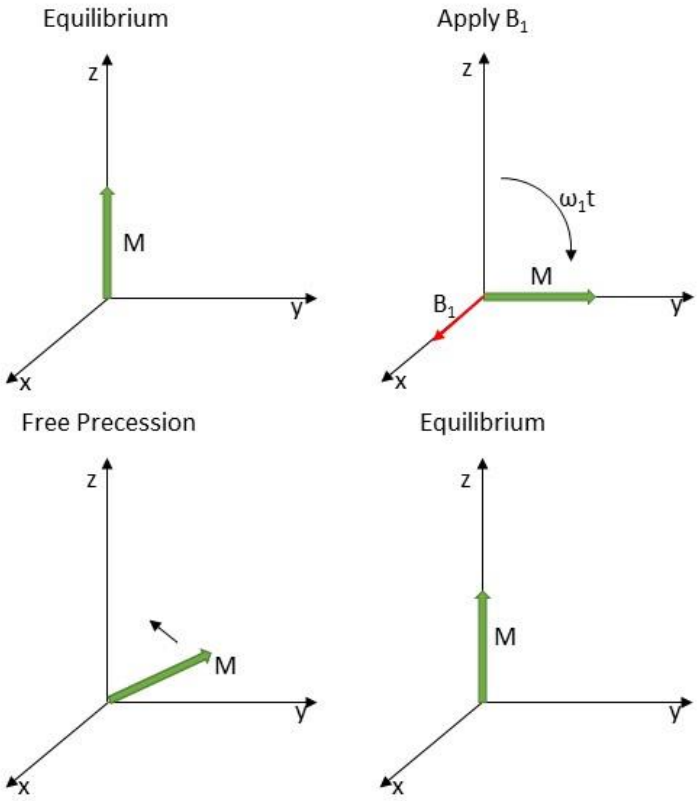


Figure 8: Evolution of magnetization (rotating reference frame)

Detection

Faraday's Law of Induction

To illustrate how signal is detected it is helpful to imagine the case where the magnetization is placed in the transverse plane, i.e. a 90^o pulse. After the magnetization is excited and placed into the transverse plane, the RF pulse in turned off and the magnetization is now in free precession (illustrated in the above figures). This precession of the magnetization vector at the Larmor frequency about the B_0 axis within a radio frequency coil is what produces a measureable signal, via electromagnetic induction. Electromagnetic induction is a phenomena in which a voltage is created in a conductor when it is placed in a varying magnetic field.

Imagine a solenoid, a coil of wire. A magnet is now moved in and out of the coil of wire. As the magnet moves in, an electromotive force, a voltage, is created which in turn induces a current in the wire traveling in one direction. As the magnet direction is changed and removed from the coil of wire, the direction of the induced current in the wire also reverses direction. This concept is illustrated in the following figure. If a current is generated in the coil of wires traveling in one direction it will have its corresponding generated magnetic field lines pointing along one direction within the coil. Now if that current is reversed, so too do the magnetic field lines within the solenoid.



Figure 9: Electromagnetic induction in a solenoid

It is now easy to see that by placing an RF coil near the magnetization vector while it is precessing at the Larmor frequency that an output signal can be generated. Referring to the following figure, as the magnetization vector precesses about the B_0 axis it will change direction within the coil therefore creating an oscillating voltage. Excitation is achieved in a similar manner whereby sending a RF pulse to a coil, it produces a B_1 field in the desired direction nutating the magnetization about its axis. As a side note, the RF coils depicted here are very simplistic and in reality the RF coils are quite complex, using a 'birdcage' configuration [17].

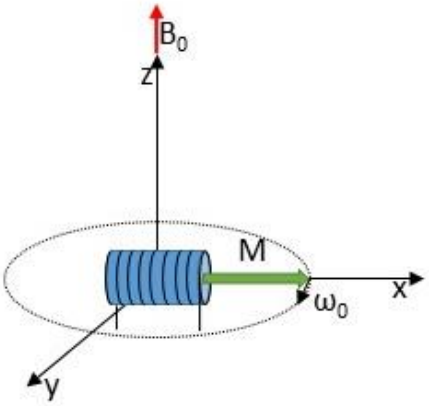


Figure 10: Precession of magnetization in solenoid

Fourier Transforms

Ignoring relaxation for the moment and imagining the magnetization vector stays in the transverse plane, i.e. the return to equilibrium via dephasing of spins doesn't occur, the output can be written in the form of $V(t) = V_0\cos(\omega_0 t)$. In order to obtain results that are meaningful, the output must be Fourier transformed. A Fourier transformation changes a function from one domain, such as time, to another domain, such as frequency,

through the use of integration. It is reversible meaning that it can transform from one domain to the other and vice versa. It is defined by

$$S(\omega)=F\{s(t)\}=\int_{-\infty}^{\infty} s(t)e^{i\omega t}dt \quad [4]$$

$$s(t) = F^{-1}\{S(\omega)\} = \frac{1}{2\pi}\int_{-\infty}^{\infty} S(\omega)e^{-i\omega t}d\omega \quad [5]$$

Fourier transforming the cosine will yield a positive and negative frequency of the same value. The Fourier transform cannot distinguish between the sign of the frequency based on the data given. So in order to distinguish these frequencies both the M_x and M_y transverse magnetization must be obtained and Fourier transformed, that is, the real (cosine) and imaginary (sine) parts must be obtained and transformed. This will allow a distinction of frequencies of the same value but with opposite sign. The following figure illustrates this

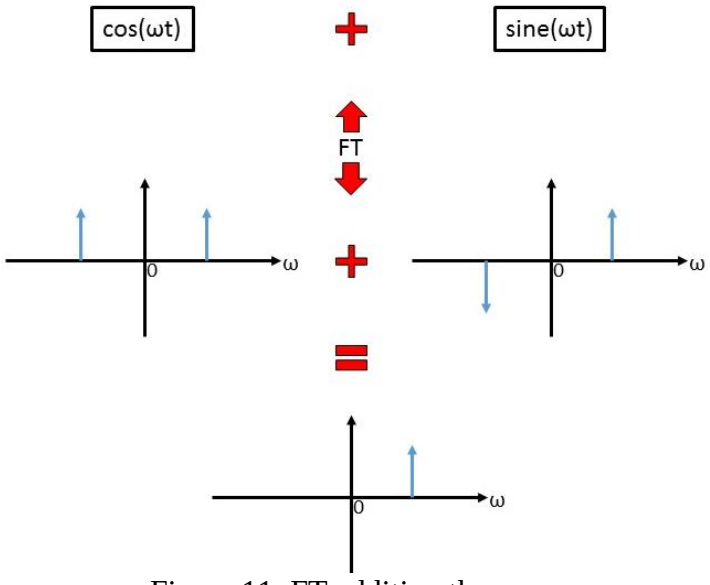


Figure 11: FT addition theorem

Quadrature Detection

The method employed to obtain both M_x (attributed to real) and M_y (attributed to imaginary) is called quadrature detection. Quadrature detection employs mixers and low-pass filters to obtain the complex difference signal. The output signal voltage is mixed with two reference signals. One that is in phase and what that is 90° out of phase, also known as quadrature phase. These signals are then passed through a filter that rejects the sum frequency terms and keeps the difference terms. The output is now the complex difference signal and is exactly proportional to that created by the magnetization. The following figure depicts the quadrature detection scheme.

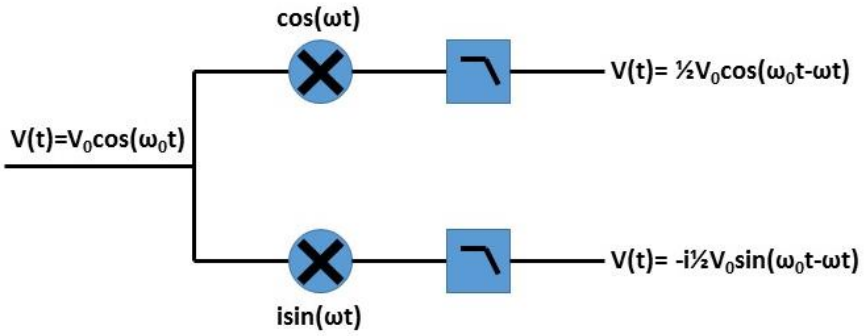


Figure 12: Quadrature detection scheme

The output can also be written in the form of a complex exponential where

$$V(t) = \frac{1}{2}V_0 \exp\left(-i(\omega_0 t - \omega t)\right) = \frac{1}{2}V_0 \cos(\omega_0 t - \omega t) - i\frac{1}{2}V_0 \sin(\omega_0 t - \omega t) \quad [6]$$

This now allows a distinction between frequencies of opposite sign when Fourier transformed. If there are any frequencies that are not at the Larmor frequency, ω_0, they

will show up as an offset frequency from the resonant Larmor frequency, $\Delta\omega = \omega_0 - \omega$. Thus spin magnetization vectors rotating faster than the Larmor frequency will show up as a positive offset while spin magnetization vectors rotating slower than the Larmor frequency will show up as a negative offset. This allows for a distinction of different frequencies from the Larmor frequency which will show up as different frequencies in a spectra once Fourier transformed.

As previously mentioned, relaxation was ignored for the previous development. Now how does the return to equilibrium of spins contribute to the signal? Imagine the magnetization vector returning back to equilibrium along the B_0 axis, so too will the signal decrease until there is no projection of the magnetization vector in the transverse plane. This decay is associated with the dephasing of spins and thus decays according to spin-spin relaxation, or transverse relaxation, described by $\exp(-t/T_2)$, where T_2 is a time constant associated with the process. Adding relaxation to the signal, an oscillating, decaying equation known as the free induction decay (FID) is formed, i.e.,

$$S(t) = S_0 \exp\big(-i(\omega_0 t - \omega t)\big) \exp(-t/T_2) \qquad [7]$$

where S_0 is proportional to the initial magnetization, M_0. A Fourier transformation of the real and imaginary signal with relaxation included where there is no phase shift will yield a real and imaginary spectra, known as the absorption spectra and the dispersion spectra. Shown in Figure 13.

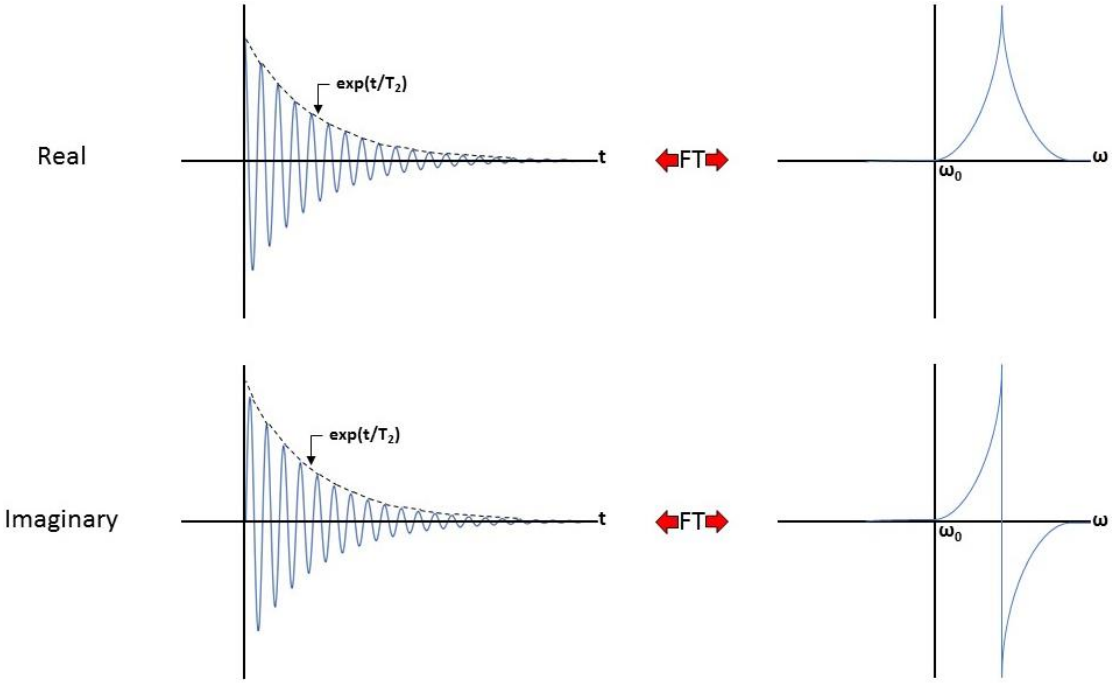


Figure 13: Real and imaginary signal and spectrum

The spectra is a Lorentzian line shape where the full width half maximum (FWHM) is $1/\pi T_2$.In order to obtain a perfect absorption spectra it is important to phase correct the acquired FID so that it has no phase shift. So that when transformed, the absorption spectra is all positive. Phase shifts can arise from things such as, the receiver not being able to immediately detect the signal which results in a small loss of the beginning of the FID or not being able to detect the exact M_x or M_y. Multiplying the signal by $\exp(-i\emptyset)$ will yield a phase corrected spectra, where $\emptyset$ is the phase shift angle. Therefore the equation for the phase corrected FID is now

$$S(t) = S_0 \exp(-i\emptyset) \exp\big(-i(\omega_0 t - \omega t)\big) \exp(-t/T_2) \qquad [8]$$

The computer does this automatically by observing the absorption spectra and adjusting ∅ until the real absorption spectra becomes all positive and has the maximum integral.

Discrete Fourier Transform

In NMR spectroscopy, the analog signal is digitized for storage in the computer. Because the computer doesn't continuously sample the FID but rather it samples in discrete time points, the discrete Fourier transform is used. This is essentially equivalent to multiplying the signal by a finite set of delta functions, N number of points, spaced by a dwell time, dt. It is important to ensure that the sampling frequency, $1/Ndt$, is greater than the FWHM of the spectra or resolution will suffer.

Relaxation

Longitudinal Relaxation

After applying an RF pulse, perturbing the spins from equilibrium along the B_0, the spins will want to return to their equilibrium state because of the dominant Zeeman interaction. They return to equilibrium via two mechanisms: spin-lattice relaxation and spin-spin relaxation. The first, spin-lattice relaxation or longitudinal relaxation, as its name describes, is the return of the magnetization vector to the longitudinal axis along the B_0 field. It is an energy exchange between the spins and their surroundings or lattice. It is characterized by the equation

$$\frac{dM_z}{dt} = -\frac{M_z - M_0}{T_1} \qquad [9]$$

which can be solved to yield

$$M_z(t) = (M_z(0) - M_0)e^{-t/T_1} + M_0 \quad [10]$$

M_0 refers to the equilibrium magnetization along the z-axis in the direction of the B_0 field. In this case, $M_z(0)$ would equal M_0 describing the magnetization along the z-axis. Therefore, M_z describes the longitudinal magnetization. T_1 is a time constant that describes the longitudinal relaxation time. If a 180° RF pulse is applied it will tip the magnetization into the negative z-axis and thus the M_z magnetization may be plotted in the following figure according to the equation above.

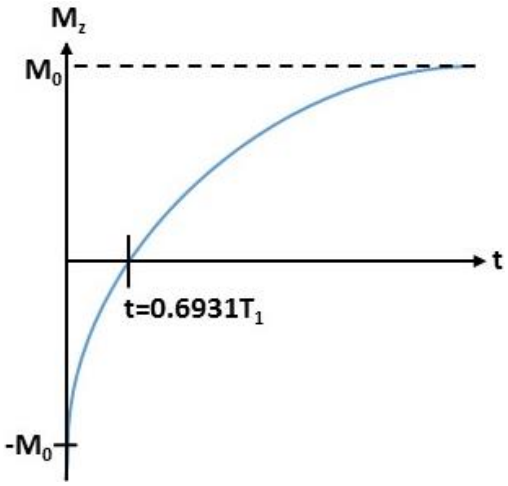


Figure 14: Longitudinal relaxation

Transverse Relaxation

The other process of spin relaxation is known as spin-spin relaxation or transverse relaxation. It is the process by which spins come to thermal equilibrium amongst themselves, hence spin-spin relaxation. It is the decay of the transverse magnetism via the dephasing of spins, or the loss of coherence of the spins. It is described by the equation

$$\frac{dM_{xy}}{dt} = -\frac{M_{xy}}{T_2} \quad [11]$$

which when solved will yield

$$M_{xy}(t) = M_{xy}(0)e^{-t/T_2} \quad [12]$$

M_{xy} describes the transverse magnetizations return to thermal equilibrium with time constant T_2. Where $M_{xy}(0)$ is the starting transverse magnetization. Applying a 90° RF pulse, the magnetization will be placed in the transverse plane and thus the transverse decay is described by equation [12 and can be plotted according to the following figure.

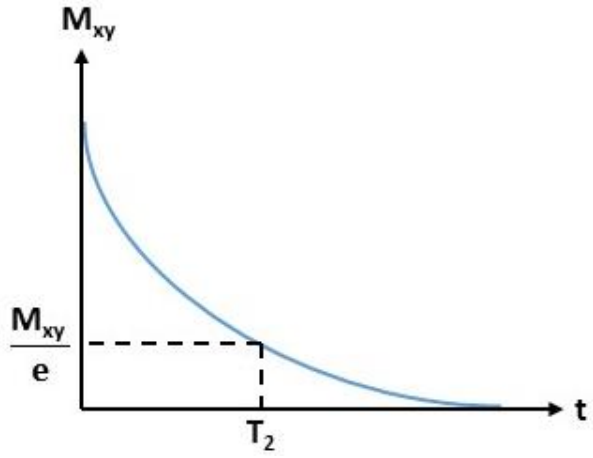


Figure 15: Transverse relaxation

Since transverse relaxation is described by the coherence of spins, it is therefore sensitive to mechanisms that dephase the spins, such as collisions due to diffusion or surface interactions, or molecular interactions between spins. This can lead to extremely short T_2 times in some media. In NMR we distinguish between the decay constant of the FID and the true relaxation time of the substance measured with a CPMG sequence by

using an asterisk. T_2^* is the decay constant of the FID that dephases due to field inhomogeneity.

Because of the additional interactions that contribute to T_2 relaxation, T_2 will always be less than or equal to T_1. In liquids T_1 and T_2 can be relatively similar but in solids T_2 is much shorter than T_1. Simplistically, this can be visualized and thought of by plotting the relaxation time vs. the molecular tumbling rate, see Figure 16. The molecular tumbling rate being related to the size and motion of the molecule. Molecules that are larger have a slower molecular motion corresponding to the divergence of T_1 and T_2, where T_2 can be much less than T_1. As molecular motion speeds up and molecules become smaller, as in free water, T_1 and T_2 are longer and can have similar values.

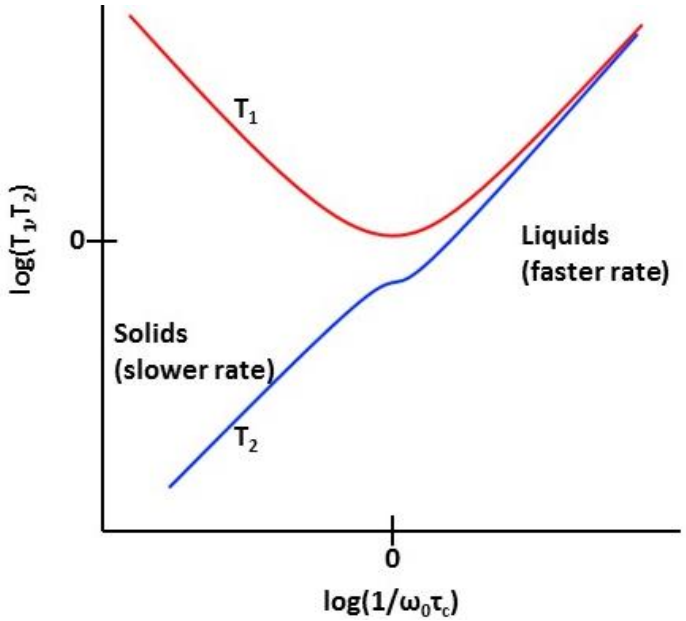


Figure 16: Relaxation vs. molecular tumbling rate

From Bloembergen, Purcell and Pound (BPP) theory, dipolar correlation functions can be developed for T_1 and T_2. These dipolar correlation functions are what describe T_1 and T_2 in Figure 16. For T_1

$$\frac{1}{T_1} = \left(\frac{\mu_0}{4\pi}\right)^2 \gamma^4 \hbar^2 \frac{3}{2} I(I+1)\left[J^{(1)}(\omega_0) + J^{(2)}(2\omega_0)\right] \quad [13]$$

And for T_2

$$\frac{1}{T_2} = \left(\frac{\mu_0}{4\pi}\right)^2 \gamma^4 \hbar^2 \frac{3}{2} I(I+1)\left[\frac{1}{4}J^{(0)}(0) + \frac{5}{2}J^{(1)}(\omega_0) + \frac{1}{4}J^{(2)}(2\omega_0)\right] \quad [14]$$

Where

$$\begin{aligned} J^{(0)}(\omega) &= \frac{24}{15r_{ij}^6}\frac{\tau_c}{1+\omega^2\tau^2} \\ J^{(1)}(\omega) &= \frac{4}{15r_{ij}^6}\frac{\tau_c}{1+\omega^2\tau^2} \\ J^{(2)}(\omega) &= \frac{16}{15r_{ij}^6}\frac{\tau_c}{1+\omega^2\tau^2} \end{aligned} \quad [15]$$

for a simple isotropic rotational diffusion model for a pair of like spins, which represent the dipolar interactions in most liquids. Each $J^{(i)}(\omega)$ term describes different dipolar interactions. A key thing to note is that T_2 has one more term than T_1 does and thus is sensitive to more interactions than T_1 giving more explanation as to why $T_2 \leq T_1$.

Bloch Equations

In order to describe the macroscopic motion of the magnetization three equations are needed: a description of the longitudinal magnetization and the transverse magnetization, and the rate of change of angular momentum.

The rate of change of angular momentum is described by

$$\frac{dM}{dt} = \gamma M \times B \qquad [16]$$

Plugging in equations [9 and [11, a set of coupled differential equations are obtained that can be used to describe the magnetization vector in the rotating frame of reference. They are

$$\begin{aligned} \frac{dM_x}{dt} &= \gamma M_y\left(B_0 - {}^{\omega}/_{\gamma}\right) - \frac{M_x}{T_2} \\ \frac{dM_y}{dt} &= \gamma B_1 - \gamma M_x\left(B_0 - {}^{\omega}/_{\gamma}\right) - \frac{M_y}{T_2} \\ \frac{dM_z}{dt} &= -\gamma M_y B_1 - \frac{M_z - M_0}{T_1} \end{aligned} \qquad [17]$$

Basic Pulse Sequences and Spin Manipulation

Signal Averaging

Due to low signal in NMR it is beneficial to add signal from multiple experiments. This has the effect that signals will continue to add coherently whereas random noise will lead to incoherence that starts canceling. This successfully enhances the signal-to-noise ratio (SNR), distinguishing the signal from the noise. The SNR improves as $N^{1/2}$, where N is the number of experiments. Increasing the number of

experiments from 1 to 2 doubles the experiment time. The time for the spins to recover their z-axis magnetization limits the number of experiments that can be added in a certain amount of time. The repetition time, T_R, is how long the experiment waits before repeating, in which time the magnetization fully recovers. Not allowing a full T_R before repeating the pulse sequence will result in a decrease in signal because the magnetization was never allowed to reach its maximum equilibrium magnetization and thus the starting magnetization is less than 100%. A good rule of thumb is to have a $T_R \geq 5T_1$. This will allow the magnetization to return to equilibrium and full signal strength will be obtained.

Phase Cycling

Phase cycling is a method used to eliminate artifacts due to the electronic hardware and quantum mechanics complications on the desired pulse sequence pathway. It is achieved by varying the phase of the pulses and the phase of the receiver in order to cancel or add certain signals. The phase of the signal is dependent on the phase of the RF pulse. Therefore signal can be distinguished from the background noise by cycling the phase of the pulse and receiver in repeated experiments in such a manner that the desired coherence pathway is additive and all others cancel. Phase cycling can be quite complex but a simple example will be explained to illustrate the effect of phase cycling.

Amplifiers often have a baseline offset, a DC offset, and to correct for this offset, without buying a more expensive amplifier, phase cycling is employed. First, a 90_x pulse is applied and then the FID is recorded. Then a 90_{-x} pulse is applied and the FID is recorded. Note that the receiver does not change phase while the applied RF pulse does. Finally, the 90_{-x} FID is multiplied by -1 and added to the 90_x FID where the signals add

and the DC offset cancels. The following figure illustrates this example. The phase diagram depicts the receiver phase as a dot and the RF phase as an arrow. Note the RF and receiver phase are always off by only 90^o and the phase difference between the two RF pulses is 180^o.

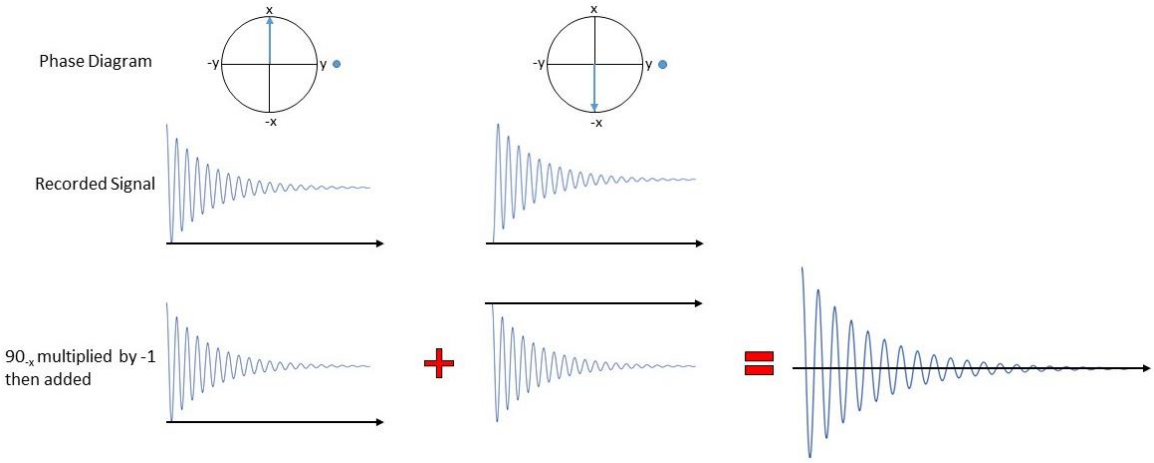


Figure 17: Phase cycling representation

Phase cycling can be used in many other ways to eliminate unwanted signal and retain the desired coherence pathway. A slightly more complex example is that used in quadrature detection called CYCLOPS. There are four steps in the phase cycle where both the receiver and RF pulse are advanced by 90^o maintaining a 90^o offset from one another. It is designed to cancel imperfections in the two phase detectors used for quadrature detection. A basic rule for the number of phase steps needed to eliminate every coherence pathway but the desired one is to raise the number of pulses to the power of 4, however in practice consideration of T_2 & T_1 and the use of crusher gradient pulses can reduce the necessary number of phase steps.

Spin Echo

It is important to understand some basic pulse sequences that are used in NMR. Many are so common that they have become second nature and are the basics of more complex pulse sequences. Understanding these sequences that have endured since the beginning will prove to be valuable and insightful in understanding basic spin manipulation and provide a crux for the more advanced.

A basic 90^o RF pulse and acquisition of the FID have been previously discussed. The next step in this sequence leads to a sequence called the spin-echo. Magnetic field inhomogeneity causes dephasing of the transverse magnetization because there is a spread of Larmor frequencies and thus a loss of phase coherence. The spin-echo causes these spins to rephase, reversing the loss of phase coherence, which form what is called an echo. The following figure illustrates the basic spin-echo sequence.

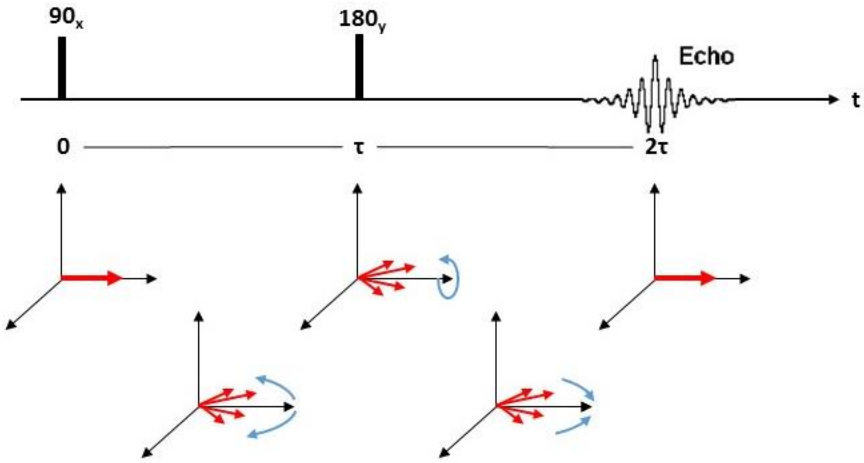


Figure 18: Spin-echo sequence and spin manipulations

A 90^o RF pulse is applied tipping the magnetization into the transverse plane. The spins now begin to dephase in the transverse plane until a time τ, at which point an 180^o

RF pulse is applied rotating the spins 180^o about the y-axis. This effectively inverts the phase of each spin. The spins now begin to refocus and at time 2τ a perfect echo is formed. Capturing the echo will return a signal, that has refocused any dephasing, that can be Fourier transformed to obtain a spectra that has only attenuated due to T_2 relaxation over the time 2τ. The spin-echo sequence essentially removes the effects of any inhomogeneous dephasing.

CPMG

After a time 2τ the spins continue to dephase and the signal is effectively lost. However, it can be successively recovered with the application of multiple 180^o RF pulses called a train. Because the effects of spin-spin relaxation are irreversible, they are the only thing contributing to the attenuation of the echoes. Thus, the envelope created by multiple spin echoes is determined only by T_2 decay. Therefore, the Carr-Purcell-Meiboom-Gill (CPMG) pulse sequence makes it possible to determine the characteristic time constant T_2. The following figure illustrates the CPMG method.

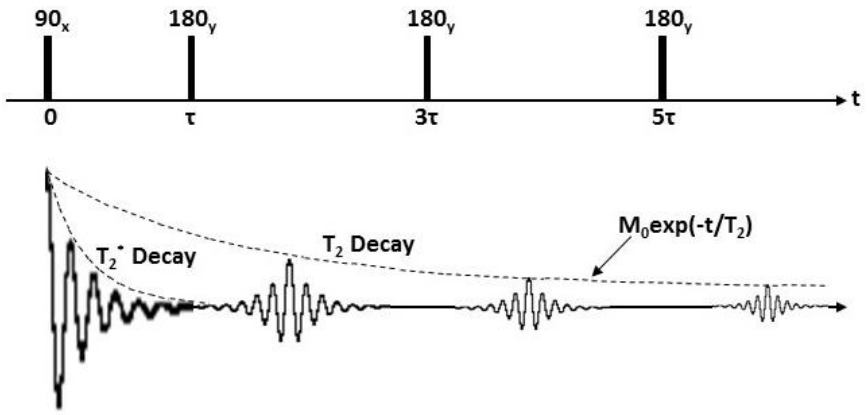


Figure 19: CPMG pulse sequence with echo envelope

The pulse sequence starts the same as the spin-echo sequence but successive 180^o RF pulses are applied at the interval 2nτ-1 and echoes are formed at 2nτ. The echoes are attenuated due to spin-spin relaxation and therefore an equation for T_2 decay can be written as

$$M_y(t) = M_0 e^{(-t/T_2)} \quad [18]$$

This describes the envelope of signal from which the characteristic time constant T_2 can be determined.

Inversion Recovery

The inversion recovery pulse sequence is used to determine the characteristic time constant T_1 as well as to suppress unwanted signals by knowing where the null point occurs (the point at which there is zero magnetization). The following figure depicts this pulse sequence.

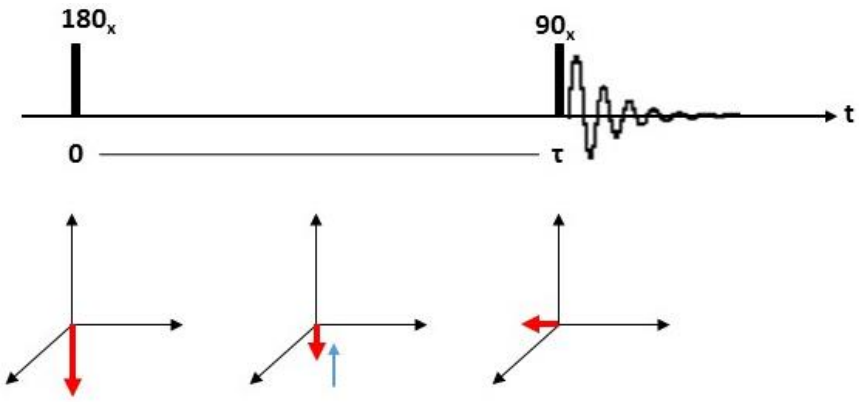


Figure 20: Inversion recovery pulse sequence and spin manipulations

The sequence differs from others in that it starts with an 180^o RF pulse that tips the magnetization into the –z-axis. During some time τ the magnetization relaxes along

the longitudinal axis due to spin-lattice relaxation. At a time τ a 90^o RF pulse is applied and tips the remaining magnetization into the transverse plane during which it begins to dephase resulting in a FID. The magnetization can be described by equation [10. If the τ time was varied the resulting maximum amplitudes of the various FID's would create a curve that is similar to Figure 14. Equation [10 can then be applied to this curve to determine the time constant T_1. Notice at $t = 0.6931T_1$ there is a crossover where the magnetization is equal to zero. This point is known as the null point and is what is exploited to suppress unwanted signals.

Gradients and K-space

Gradients

In spectral imaging, inhomogeneity in the magnetic field was seen as a nuisance, where it hindered resolution. Looking at them from a time-domain perspective however, it's seen that an echo attenuation is formed based on the time between pulses in which molecular motion occurs. This molecular motion being dictated by variations in the magnetic field. The basis of NMR imaging is in this spatially varying magnetic field, called a magnetic field gradient. The most useful gradient in NMR is a linear magnetic field gradient. The fundamental principle that makes imaging possible from these linear magnetic field gradients leads us back to the Larmor equation, $\omega_0 = \gamma B_0$. If B_0 was made a function of position, that is, there was a linear magnetic field gradient applied, then ω_0 would also be a function of position and therefore the position of one spin could be distinguished from another.

Applying a gradient in one dimension, according to Maxwell's equations, would lead to smaller contributions in the other two dimensions. In high field NMR, it is said that these smaller contributions are negligible thus leading to the equation

$$\omega_0(\boldsymbol{r}) = \gamma B_0 + \boldsymbol{r} \cdot \boldsymbol{G} \qquad [19]$$

To illustrate the use of a gradient to achieve spatially dependent frequencies, two tubes of water are depicted in Figure 21 where a gradient is applied on the right and no gradient on the left. When no gradient is applied one spectra is obtained at a Larmor frequency associated with water. When a linear gradient is applied the result is a distribution of frequencies dependent on position with intensity proportional to the number of spins in the plane perpendicular to the applied gradient. Therefore a 1D profile representing the image is obtained after the FT. Taking the next step, gradients could then be applied in the other two directions to obtain a representation of the three dimensional structure.

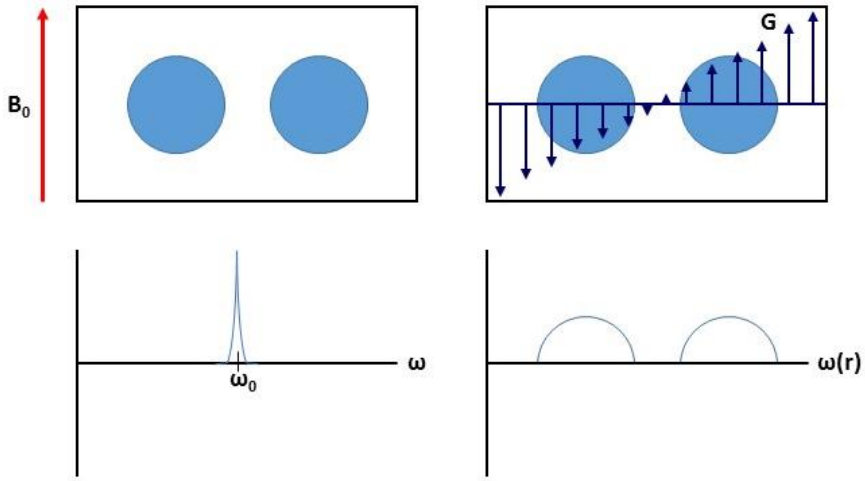


Figure 21: Tube of water with and without gradients applied

K-space

In order to understand how two and three dimensional images are created it is necessary to introduce and understand k-space and how pulse sequences traverse k-space. The spins contribute a transverse magnetization in a rotating frame set on resonance, ignoring relaxation for simplicity, given by

$$M(\boldsymbol{r},t) = M(\boldsymbol{r},0)e^{(-i\gamma \boldsymbol{r}\cdot \boldsymbol{G}t)} \quad [20]$$

Now imagine applying a gradient along the z-axis. The equation then takes the form

$$M(z,t) = M(z,0)e^{(-i\gamma zGt)} \quad [21]$$

The evolution of the phase of spins along the z direction take the form of a helix. The wavelength of the helix will become smaller, it winds up tighter, as either time goes on or a larger gradient is applied. Figure 22 depicts the phase evolution of the spins under the application of a gradient applied in the z direction..

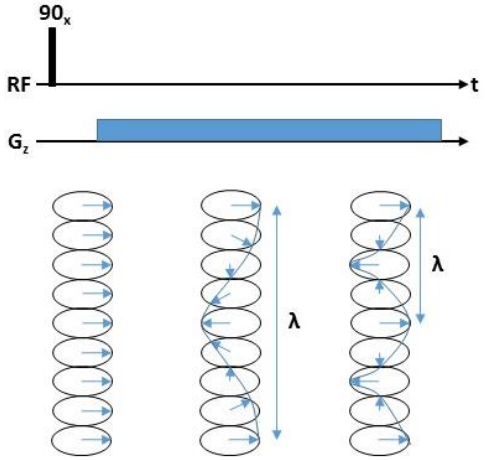


Figure 22: Evolution of spin phase under the application of a gradient

The wavelength is given by

$$\lambda = \frac{2\pi}{\gamma G t} \quad [22]$$

Where the reciprocal space vector, **k**, is thus given by

$$\boldsymbol{k} = \frac{\gamma G t}{2\pi} \quad [23]$$

From this it is clear to see that k-space can be traversed by either varying G, the gradient amplitude, or t, the time the gradient is applied. Varying t is known as frequency encoding and varying G is known as phase encoding, both of which will be discussed in more detail. Substituting equation [23 into equation [20, the phase evolution of the magnetization can thus be described as

$$M(\boldsymbol{r}, t) = M(\boldsymbol{r}, 0) e^{(-i\boldsymbol{k}\cdot\boldsymbol{r})} \quad [24]$$

The sampling of k-space is dependent on the pulse sequence utilized. There is nearly an infinite number of ways k-space could be sampled. To illustrate how certain pulse sequences traverse k-space two examples are discussed. The first using only phase encoding, varying only G, and the second utilizing both phase and frequency (read) encoding, varying G and varying t.

The phase encoding pulse sequence scheme and its k-space trajectory are shown in Figure 23. The first pulse excites the spins into the transverse plane. Then some portion G_x and G_y are applied, positive G_x or G_y going in the positive k_x or k_y direction with an increase in amplitude meaning a farther point in k-space is reached, denoted by the blue arrow going to 1. The application of the 180 pulse effectively reverses the sign

and places the spins in the opposite quadrant, denoted by the black arrow going to 2. An echo will be formed from which the FID is recorded and a signal intensity for that point is obtained. The magnetization is then allowed to decay back to equilibrium putting it back at k = 0. The sequence is then repeated with different values for G_x and G_y until every point in k-space has been traversed. This must be repeated N^2 times, where N is the number of points in a dimension of k-space, in order to capture all of k-space. Because of this, this sequence can be time consuming. A way to decrease the amount of time is to use what is called a read out gradient.

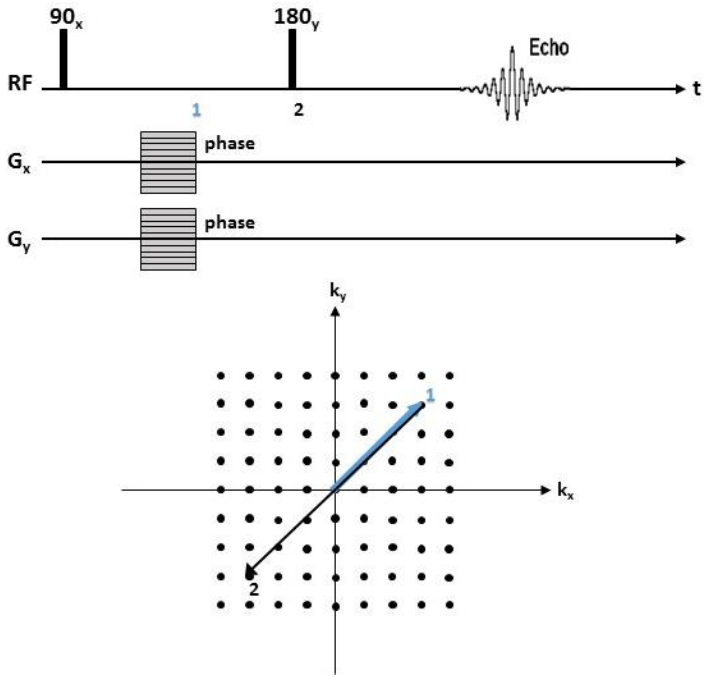


Figure 23: Pure 2D phase encoding sequence with k-space trajectory

Figure 24 depicts a read (frequency) and phase encoding scheme and its k-space trajectory. In this sequence the G_x is considered a readout gradient because a gradient is applied during the echo effectively acquiring a line a k-space points. Utilizing equation

[23, Δk can be determined for the case of phase encoding or read (frequency) encoding. For phase encoding, $\Delta k = \frac{\gamma}{2\pi}\Delta GT$ where T is a constant for the gradient pulse time. For read encoding, $\Delta k = \frac{\gamma}{2\pi}G\Delta t$.

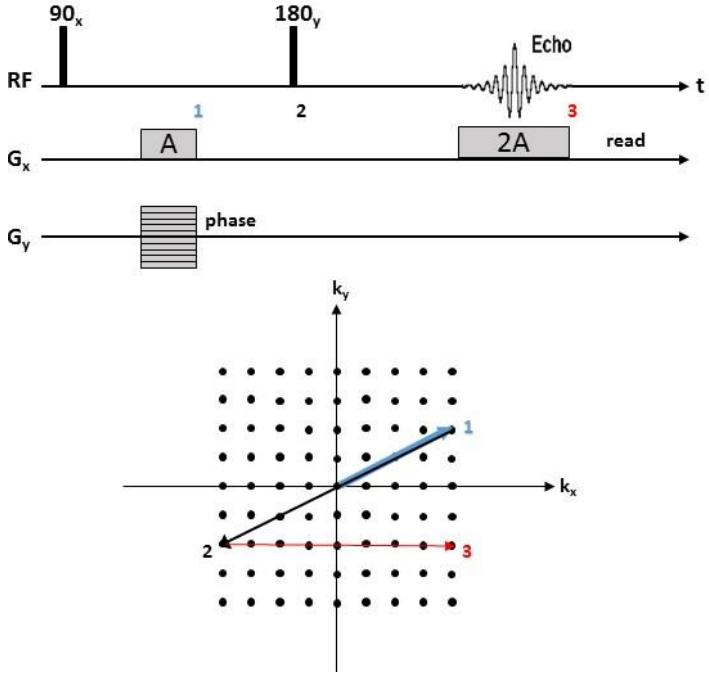


Figure 24: Read and phase encoding 2D sequence with k-space trajectory

Referring again to Figure 24, the first 90 pulse places the magnetization in the transverse plane. Then a gradient G_x and G_y are applied. G_x applies a certain amplitude that will take it to the edge of k-space while G_y can be ramped to any value taking it either up or down in k-space. The application of these gradients are denoted by the blue arrow going to 1. A 180 pulse is then applied again effectively reversing the sign and places it at the point in the opposite quadrant, denoted by the black arrow going to 2. Finally, a readout gradient is applied during the echo acquiring a whole line of k-space denoted by the red arrow. The magnetization is then allowed to return to equilibrium and

the sequence is repeated. To capture all of k-space this sequence must be repeated a total of N times, significantly less than for pure phase encoding. A key thing to note here is that the readout gradient is applied for twice the area of the first gradient, sometimes called a rewind gradient, because this first gradient effectively traverses half of k-space, rewinding it, so that during read out a whole line of k-space is acquired.

Since k-space is sampled as discrete points, a discrete Fourier transform is used to obtain the conjugate space that represents the image, ρ(**r**). The signal, S(**k**), and the spin density, ρ(**r**), are mutually conjugate. Therefore, they can be represented by the following Fourier relationships, or conjugate pairs:

$$S(\mathbf{k}) = \int \rho(\boldsymbol{r}) e^{i\boldsymbol{k}\cdot\boldsymbol{r}} d\boldsymbol{r} \quad [25]$$

$$\rho(\mathbf{r}) = \frac{1}{2\pi} \int S(\boldsymbol{k}) e^{-i\boldsymbol{k}\cdot\boldsymbol{r}} d\boldsymbol{k} \quad [26]$$

The image resolution is determined by π/k_{max} or the sampling range of the particular dimension. This makes sense, as it is known that finer detail is stored in the outer part of k-space. Therefore, sampling farther out will result in finer detail/resolution.

ZTE

A more complex imaging sequence that is used in this research is called the zero time echo (ZTE). It is a 3D radial center out k-space acquisition with k = 0 after the application of the 90^o RF pulse. The gradient, G, is a read gradient applied during signal acquisition that has a contribution of x, y, and z, therefore acquiring k-space in a spherical nature. The gradient is ramped up and on before the application of the RF pulse

and therefore the acquisition starts immediately after the RF pulse. Because of hardware limitations, there is a delay, δ, before the receiver can switch from transmit to receive mode. Thus, there is no signal acquisition during the delay because, even though the gradient is on and data can begin to be read out, the receiver can't pick up the signal. Consequently, there will be some missing center k-space points and the Fourier transform no longer applies. The missing k-space points and image reconstruction are dealt with through the use of an algebraic reconstruction and 3D gridding algorithm. This pulse sequence has particular application in samples with very short transverse relaxation times, small T_2 values. Figure 25 depicts this particular pulse sequence.

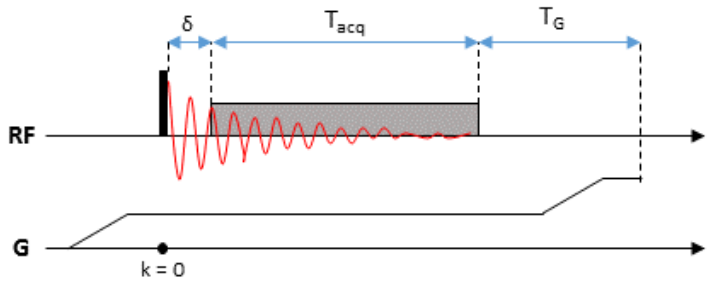


Figure 25: Three dimensional ZTE pulse sequence used in experiments

Selective Excitation

Selective excitation is used to manipulate spins of a certain frequency or to manipulate spins within a specified section of the FOV. The first uses different RF pulse shapes, powers, and times to select the desired frequencies where the latter uses a linear magnetic field gradient in combination with the selective RF pulse. These will be referred to as RF selective excitation and slice selective excitation.

The first, RF selective excitation, has essentially two types of pulses, a broadband and a narrowband pulse termed hard and soft pulses. Because the tip angle is determined by

$$\theta = \gamma B t \qquad [27]$$

a hard pulse will have a larger B with a shorter time, t, and a soft will have a smaller B with a longer time, t. Since the bandwidth is proportional to the inverse of the pulse time, a hard pulse with a short pulse time will excite a large range of frequencies around the Larmor frequency while the soft pulse is just the opposite.

Pulse shapes can also have an effect on excitation frequencies. For instance a soft pulse may use a sinc pulse, in the time domain, which would translate to a hat shaped excitation range in the frequency domain. This is of particular importance when using selective soft pulses because if it were the other way around, a hat pulse yielding a sinc shaped excitation range, a uniform range of frequencies would not be excited.

Slice selective excitation uses a linear magnetic gradient to create a spread of frequencies dependent on location from which a certain frequency, and therefore a certain location, can be excited using a soft RF pulse. The thickness of the slice is determined by $BW/\gamma G_S$, where BW is the bandwidth. The following figure depicts the spread of frequencies due to the application of a linear magnetic field gradient where slice selection can be utilized to excite a specific section by targeting the associated frequency. For instance, if one wanted to excite a slice around ω_2, corresponding to a location +z, one

need only apply a soft pulse targeting that frequency, where the slice thickness is determined by $BW/\gamma G_S$, where BW is the bandwidth.

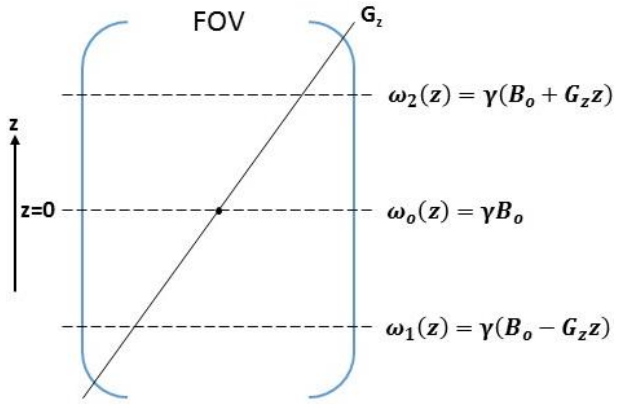


Figure 26: Linear magnetic field gradient with position dependent ω

Translational Motion

The phase helix holds information regarding the molecular motion of the molecules because the spin phase is related to molecular position. The use of a gradient winds a phase ino the spins. By then applying a gradient that is equal and opposite, the phases of the spins will be unwound to their original states, in the case where the molecules don't move, thus forming an echo. This is depicted in the following figure.

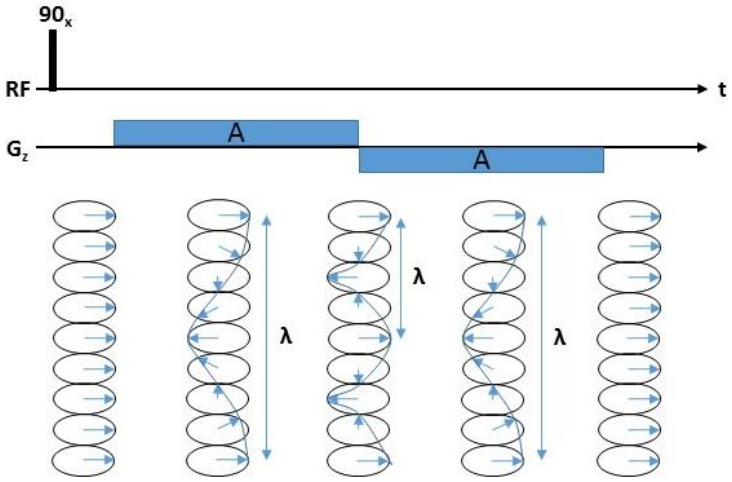


Figure 27: Gradient echo sequence depicting the evolution of spins

All this is assuming that the spins do not move, that there is no molecular motion. It is clear that if there is motion, the final phase distribution will be disturbed and, since the phase is dependent on molecular motion, the signal will depend on that motion. This change in the final phase distribution produces a phase shift. It is this phase shift that allows for the interpretaion of any molecular translation. The signal from the spin isochromats can be represented as

$$M(\boldsymbol{r}_o, t) = M(\boldsymbol{r}_o, 0)e^{(i\emptyset(t))} \quad [28]$$

where

$$\emptyset(t) = \gamma \int_0^t \boldsymbol{g}(t') \cdot \boldsymbol{r}(t')dt' \quad [29]$$

The phase shift is represented by equation [29 where $\boldsymbol{g}(t')$ is the gradient and $\boldsymbol{r}(t')$ is the position of the spin at time t. This equation doesn't take into account the spin phase sign change due to RF pulses so it is helpful to define an effective gradient, $\boldsymbol{g}^*(t')$,

defined with an asterisk. This effective gradient has the effective sign of the gradient at any given time t, considering the sequence of RF pulses that has previously played out. Figure 28 illustrates the effective gradient where after the 180^o RF pulse the sign of the gradient is effectively changed. Figure 27's effective gradient is the same as the gradient because there is no reversal due to an RF pulse.

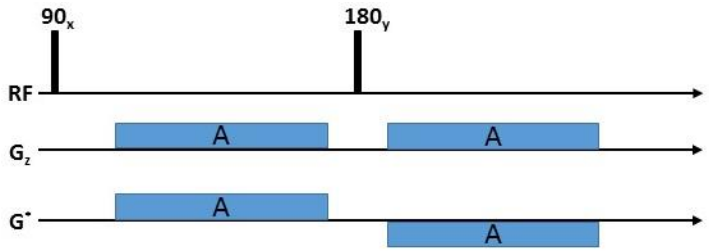


Figure 28: Spin echo sequence with gradient pulses and effective gradient

To prove that the gradients must be equal and opposite for an echo to form, the case where $\boldsymbol{r}(t') = \boldsymbol{r}_o$ is observed, that is, there is no translational movement of the spins. Equation [28 will then yield $M(t) = M(0)$, forming a perfect echo, if $\int_0^t \boldsymbol{g}^*(t')dt' = 0$. Therefore, in order to form a perfect echo the integral of the effective gradient must equal zero.

In order to understand the effects that the effective gradient has on the phase of the spins and its relation to translational motion of the spins, the echo signal is normalized with the condition that $\int_0^t \boldsymbol{g}^*(t')dt' = 0$. Thus,

$$E(t) = \frac{M(t)_{\boldsymbol{g}^*(t')\neq 0}}{M(t)_{\boldsymbol{g}^*(t')=0}} = e^{(i\emptyset(t))} \qquad [30]$$

Consider the motion to have a constant velocity with acceleration, then $\boldsymbol{r}(t') = \boldsymbol{r_o} + \boldsymbol{v}t' + 1/2\,\boldsymbol{a}t'^2$. Substituting this into equation [29 then substituting that into equation [30 and expanding will yield

$$E(t) = \exp(i\gamma \boldsymbol{r}_o \int_0^t \boldsymbol{g}^*(t')dt' + i\gamma \boldsymbol{v} \int_0^t \boldsymbol{g}^*(t')t'dt' + i\gamma \boldsymbol{a} \int_0^t \boldsymbol{g}^*(t')t'^2 dt' + \cdots \quad [31]$$

From this it is clear that if the final phase shift, ergo the signal, is to depend on motion and not the starting positions of the spins then what is called the zeroth moment of the gradient, M_0, $\int_0^t \boldsymbol{g}^*(t')dt'$, must be equal to zero. Otherwise a contribution of the starting position, $\boldsymbol{r}_o$, will be included in the echo signal. The same can be done for velocity, acceleration, and other higher order terms. If velocity needs to be compensated for, the first moment M_1, $\int_0^t \boldsymbol{g}^*(t')t'dt'$, must be equal to zero at the time the echo is formed.

The following figure depicts two different pulse sequences where the effective gradient has been manipulated to change what the echo will be sensitive too. In the first one, it is sensitive to velocity because the first moment does no go back to zero after the application of the gradients when the echo would form. Thus, from the above equation there will be a contribution from the velocity term. While in the second one, it is sensitive to acceleration and compensates for velocity, allowing no net phase shift due to coherent velocity. This is noted in the fact that both M_o and M_1 return to zero after the gradient have been applied. Therefore, only the acceleration term will be present in the echo signal equation above.

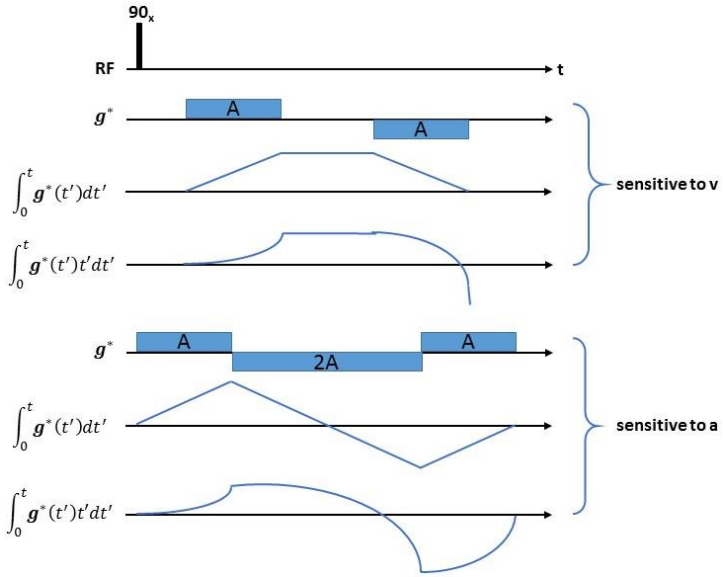


Figure 29: Uncompensated (top) and compensated (bottom) gradients

It is clear to see that the effective gradient can be designed for many purposes. If one needed to compensate for constant fluid flow the sequence could be designed such that it was sensitive to position and the first moment was zero. Also vice versa, one could design a sequence, as above, to allow for sensitivity of velocity but negate the phase shift due to spin starting position.

PGSE

At this point the idea of q-space imaging through the use of the pulsed gradient spin echo (PGSE) sequence can be introduced. Much like its imaging counterpart, k, which is tied to imaging position, q-space obtains data related to displacements which is useful in determining things such as diffusion and velocities within a system. First, a brief discussion of the PGSE sequence is necessary. Figure 28 is essentially a PGSE sequence, except that the gradients in the PGSE sequence are applied quickly such that there is

negligible motion in the time frame in which the phase is ‘wound’. The PGSE sequence is depicted in the following figure.

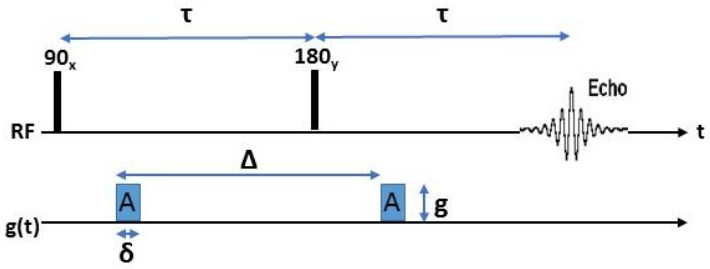


Figure 30: PGSE sequence

This sequence is a form of the previously discussed spin echo sequence. τ is the time between the 90° and 180° RF pulses with an echo formation at 2τ. δ is the gradient pulse time and Δ is called the mixing time, the time between the start of the two gradient pulses. As previously discussed, the stipulation for an echo to form requires that the zeroth moment is zero. In other words, the pair of gradient pulses must be equal and opposite, the first ‘burning’ a phase into the spins and the second ‘unwinding’ this phase. This results in an echo signal that is dependent on the phase related to the molecular motion that took place during time, Δ. Stejskal and Tanner developed an idealized equation for the normalized echo signal described by

$$E(\boldsymbol{g}) = exp\left(i\gamma\delta\boldsymbol{g}\cdot\boldsymbol{v} - \gamma^2 g^2\delta^2 D(\Delta - \delta/3)\right) \quad [32]$$

The first contribution within the exponent describes the phase shift of a coherent motion which displaces all the spins by the same amount, ergo steady flow, with no signal attenuation. The second contribution represents the diffusive contribution. The negative sign in front denotes an attenuation of the echo signal, contrary to steady flow,

which arises due to the incoherent diffusive motion which produces incoherent phase shifts across the nuclear ensemble. Thus, there is a phase shift due to steady flow and a signal attenuation due to diffusion.

Extending some concepts, if one wanted to be rid of the signal due to flow and study only the diffusive contribution, a manipulation of the gradients could be done such that the zeroth and first moments went to zero at the echo. Thus, the sequence would be velocity compensated and only the attenuation due to diffusion would remain. Further, through the use of a Stejskal-Tanner plot one could obtain the self-diffusion coefficient of the fluid within the system of study. Clearly, this PGSE sequence is useful and has a lot of potential for studying flow and diffusion, especially in porous media.

Q-Space and Propagators

To thoroughly understand q-space and extend the usefulness and meaning of the PGSE sequence, the averaged propagator and its relation to the echo signal will be discussed. First, one must take a step back and understand conditional probabilities. The conditional probability measures the probability of an event happening given that another event has occurred. The conditional probability for a particle to be at x_1 at time t_1 given that it was initially at x_o at time t_o is given by the joint probability of both occuring divided by the initial probability density which is given by the following equation:

$$P(x_0, t_0|x_1, t_1) = \frac{P(x_0, t_0; x_1, t_1)}{p(x_0, t_0)} \quad [33]$$

Since Brownian motion is a Markovian process, meaning that the particle position at x_1 at time t_1 is not dependent on where the particle was prior to t_o, the probability of

paths can be calculated in a stepwise manner. To find the conditional probability of any starting and finishing point, one needs to integrate over the intermediate paths. Thus

$$p(x_0, t_0|x_2, t_2) = \int p(x_0, t_0|x_1, t_1)\, p(x_1, t_1|x_2, t_2) dx_1 \qquad [34]$$

This can be done to find the probability of x at time t by integrating over all starting positions. Furthermore, since our interest is in the displacement, we write the probability density as a function of **r**, which is the coordinate in 3D. Thus, the three dimensional probability density of the final position $\boldsymbol{r}'$ at time t is

$$p(\boldsymbol{r}', t) = \int p(\boldsymbol{r}, 0)\, P(\boldsymbol{r}, 0|\boldsymbol{r}', t) d\boldsymbol{r} \qquad [35]$$

Now this can be applied to the echo signal with a little thought. This equation simply represents the probability for a spin to move during a given time. In order to find our desired echo signal for an ensemble of spins, the phase shift of each spin is simply weighted by the probability of that spin to move $\boldsymbol{r}'$ at time Δ given that it was initially at $\boldsymbol{r}$. The probability is exactly that represented in equation [35. Also, $p(\boldsymbol{r}, 0)$ is exactly representative of $\rho(\boldsymbol{r})$, the molecular density function, since the magnetization of the spins at time zero is synonymous of the position of the molecular spins at time zero. Thus, our echo signal can now be written as

$$E(\boldsymbol{g}, \Delta) = \int \rho(\boldsymbol{r}) \int P(\boldsymbol{r}, 0|\boldsymbol{r}', \Delta)\, exp(i\gamma\delta\boldsymbol{g} \cdot [\boldsymbol{r} - \boldsymbol{r}'])\, d\boldsymbol{r}' d\boldsymbol{r} \qquad [36]$$

To make this equation more useful and to have a Fourier relationship pair, as k-space has with the molecular density function, a few definitions and substitutions will be made. First, we define the reciprocal space q as

$$\boldsymbol{q} = \gamma \delta \boldsymbol{g} \quad [37]$$

This is simply a function of the applied gradient weighted by the gyromagnetic ratio and the gradient pulse time. We also define the displacement as being $\boldsymbol{R} = \boldsymbol{r}' - \boldsymbol{r}$. Finally, we introduce what is called the average propagator. This is the ensemble average of the displacement from the origin of all possible starting positions. This essentially yields a distributions of displacements from their initial starting positions for a certain time. This is defined as

$$\bar{P}(\boldsymbol{R}, t) = \int \rho(\boldsymbol{r}) P(\boldsymbol{r}, 0 | \boldsymbol{r} + \boldsymbol{R}, t) d\boldsymbol{r} \quad [38]$$

Now substituting those three definitions into equation [36 yields

$$E(\boldsymbol{q}, \Delta) = \int \bar{P}(\boldsymbol{R}, \Delta) exp(i\boldsymbol{q} \cdot \boldsymbol{R}) d\boldsymbol{R} \quad [39]$$

This equation is now extremely useful and provides insight into q-space and its relationship with the echo signal. It is clearly seen that this now almost identically resembles the Fourier relationship of equations [25 and **Error! Reference source not found.** for that of k-space. So q-space acquisition allows one to obtain the average propagator, $\bar{P}(\boldsymbol{R}, \Delta)$, where it has a Fourier relationship with the echo signal, $E(\boldsymbol{q}, \Delta)$, just as k-space acquisition allows one to obtain the molecular density function. The difference

being that the PGSE sequence aquires information about the dynamic displacements, **R**, whereas a k-space imaging sequence acquires information about the static displacements, **r**. Tying into the Stejskal-Tanner relationship previously discussed, one could write the normalized echo signals for diffusion and flow as

$$E(q,\Delta) = \exp(-q^2 D\Delta) \quad [40]$$

$$E(\boldsymbol{q},\Delta) = \exp(i\boldsymbol{q}\cdot\boldsymbol{v}\Delta) \quad [41]$$

As an example of what an average propagator would look like obtained from the echo signal of the PGSE sequence, consider water diffusing around in a tube, particularly, only in the z direction. This would simplify the **R** in equation [39 to just Z. So running a PGSE sequence with narrow gradient pulses and then Fourier transforming this would yield the average propagator displayed in the following figure.

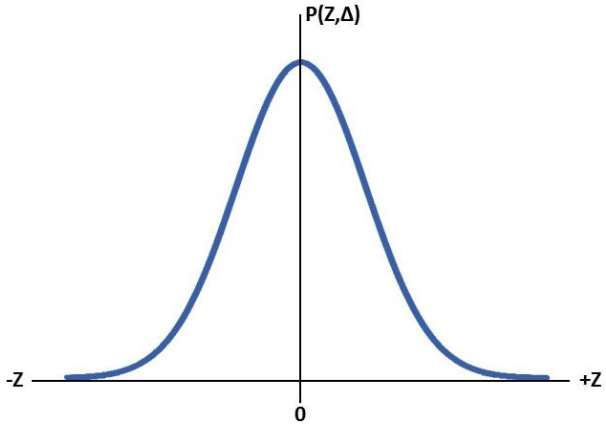


Figure 31: Diffusion Propagator

This is a Gaussian distribution, same as if solved with Fick's Law, representing the distribution of displacements of the spins after time Δ. As seen, some move positive

and some move negative, there is an equal distribution of both, but most don't move at all or move back to the same position as they started.

This brief introduction of NMR, although seemingly long, should be enough for one to understand the concepts presented in the following thesis. Many different pulse sequences used to obtain various data for experiments will also be discussed in more detail within the body of this document where the introduction will prove to be a useful reference.

3. ZTE SEQUENCE OPTIMIZATION

Introduction

Imaging of rock cores and porous media can prove difficult due to the very short relaxation times, mainly T_2^*, due to the increase in molecular interactions within the small pores along with the small amount of water. Because sequences such as the spin echo sequences require the use of a 90^o and 180^o pulse, as opposed to a short tip angle used by specialized sequences, these pulses take longer to apply and by the time the RF coil is switched to receive most of the signal, if not all, would already be gone. This leads to the use of some specialized pulse sequences designed to image systems with ultrashort T_2^*'s, such as single point imaging (SPI), single point ramped imaging with T_1 enhancement (SPRITE), and zero echo time (ZTE). Information on these sequences and more can be found in [18-20].

Therefore it is an important part of this work to explore these sequences designed to image ultrashort T_2^* systems and determine what sequence would be best to use. It is important that the sequence be able to adequately image short T_2^* samples and to capture the image quickly, as some experiments will be dynamic experiments in need of a "snapshot". This section discusses the chosen ZTE sequence, the optimization of it, and its advantages and disadvantages.

Parameter Manipulation

The ZTE sequence was chosen because it was the quickest sequence and it provided adequate resolution. The ZTE imaging sequence [18-20] is depicted in Figure 32. Its value comes from capturing fast relaxing decays, short T_2 and T_2^* values. This is achieved by switching on a readout gradient before RF excitation and ramping through gradient values acquiring k-space in a 3D radial center-out manner. By having the gradient already switched on before excitation, there is no added down time between acquisition and RF excitation. The only down time being the physical limit on how fast the hardware can switch between transmit and receive, denoted by δ. Therefore, more of the FID can be obtained at the cost of losing some initial k-space points due to the delay, δ. Due to these missing k-space points the typical Fourier transformation for image reconstruction does not hold. The missing k-space points and image reconstruction are dealt with through the use of an algebraic reconstruction and 3D gridding algorithm [18]. The sequence also utilizes short tip angles, further helping to shorten TR as well as capture the fast decay. That is, pulses that are less than 90°.

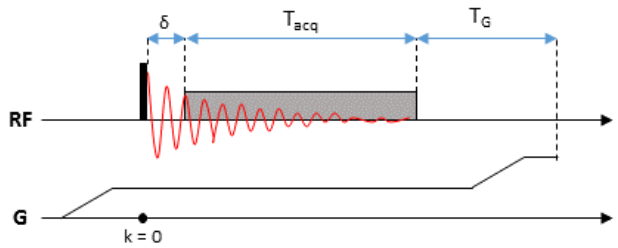


Figure 32: Three dimensional ZTE pulse sequence with hard RF pulse

In order to optimize the ZTE sequence and determine the adequate parameters, a rubber sample was first used that had a similar short T_2 relaxation time as a saturated

Berea rock core, i.e. on the order of 5ms. The rubber actually had a longer T_2 but it made it easier to initially image and manipulate sequence parameters by providing slightly more signal that was uniform as opposed to dealing with saturating a rock core that had less signal and was more heterogeneous. Parameters were therefore manipulated first using the rubber sample then, once a better understanding of the sequence was obtained, a saturated Berea rock core was used. Many parameters that were investigated and will be discussed include: the bandwidth, the pulse length, the pulse power, the tip angle, the polar under sampling, the field of view (FOV) and matrix size, the repetition time (TR), and the reconstruction options.

In order to resolve an image, the excitation bandwidth per pixel must be greater than the linewidth of the sample otherwise blurring will occur. Therefore, increasing the excitation bandwidth would increase your resolution until the image was fully resolved. However, increasing the bandwidth will lead to more missing k-space points because faster sampling will place more points within the down time, δ, where they are not being acquired. Therefore, there is a trade-off between bandwidth and missing k-space points where a bandwidth greater than the optimum leads to poor image quality. It was found that any more than 2 missing k-space points leads to poor image quality and thus a maximum bandwidth of 200 kHz was used.

Since the ZTE sequences utilizes short tip angles, the pulse time is significantly shorter than a 90^o pulse. Since the image can't be fully resolved, it's important to maintain the maximum bandwidth to achieve the best resolution possible. Bandwidth is inversely related to the pulse length, a shorter pulse means a larger bandwidth. Therefore,

by maximizing our bandwidth we shorten our pulse time. Thus, if we want to change the tip angle we must change the pulse power. So with the bandwidth maximized and the pulse time shortened, we increase the pulse power to increase the tip angle and obtain a FID with more signal. However, there are hardware limitations and only so much pulse power can be achieved. Therefore, a bandwidth of 200,000 kHz resulted in a pulse time of 6.4μs, a maximum pulse power of -3dB, a tip angle of 6.4^{o}, and 1.8 missing points.

In order to capture the entire rock core without any artifacts, the FOV needed to be adjusted. The FOV needed to be just big enough to capture all the rock core and any background signal so as to not create any wrap-around artifacts but not so big that the resolution and sequence time began to suffer. The optimum FOV in the SWB 60mm probe was found to be around 60x90x60mm with a matrix size of 64x64x64. As latter discussed the actual resolution was determined to be somewhere around 3mm/pixel, so a matrix size of 64^3 was more than adequate. Increasing the matrix size only exponentially increased the image reconstruction time and gradient duty cycle without providing any additional resolution gain.

The polar under sampling was also looked at. The polar under sampling essentially acquired less radial lines, under sampling the data and saving experiment time. Increasing the under sampling did not show much difference. Considering its small change in the already short sequence time, and the fact that the resolution was not fully resolved, the polar under sampling was left at 1, sampling the entire radially space. The repetition time (TR) was determined from the Ernst angle equation and increasing the TR showed no improvement in the signal only lengthening the experiment time. Therefore, a

TR of 3.84ms was chosen as it was larger than the Ernst angle calculation but to the point where an increase showed no further signal increase.

Image Reconstruction and Analysis

During the image reconstruction and analysis it was found that a user intensity range needed to be specified so that the reconstructed images all had the same image intensity intervals and were comparable. That user range was chosen to be 0 – 200,000 for the saturated Berea rock core. This allowed an accurate comparison between images where an increase or decrease in the water saturation could be easily detected and measured in the image intensity.

Since the saturated rock core had a small signal the background signal, from things like the AFLAS sleeve, PEEK tube, and core holder, was significant. Two things were done to enhance the saturated core signal and separate it from the background signal. The first was to add Magnevist to the water to enhance the signal from the rock core, increasing the signal intensity making it more distinguishable from the background signal. The second was to obtain a background image with a dry rock core and use it to subtract out the background. The background subtraction was done in Prospa where the saturated rock matrix was subtracted from the background matrix. Figure 33 shows an example of this subtraction. An axial slice of a fully saturated core with background signal is subtracted from the same slice with a completely dry core where only the background signal exists yielding only the signal from the water within the rock core.

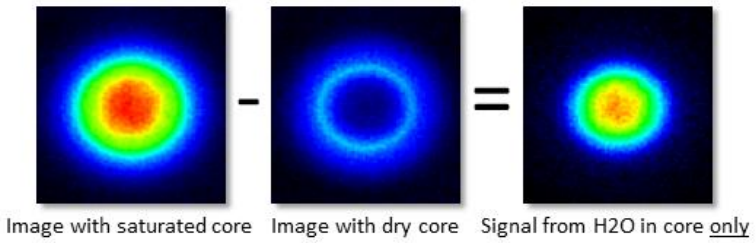


Figure 33: Background subtraction for ZTE images

Phantom Resolution Experiments

Introduction

As discussed above the bandwidth is not large enough to fully resolve the image pixels and therefore the signal will bleed into the surrounding pixels blurring the image. In order to determine the actual resolution of the optimized sequence a phantom was created that had multiple slices of different thickness of a red rubber that had a comparable T_2^* to the saturated Berea rock core. The slices would start small and grow in size. If the slice was fully resolved the full width half maximum (FWHM) of the 1D signal intensity would be about the same as the thickness of the rubber slice. However, if the FWHM was greater than the slice thickness, pixel bleed through has occurred and the slice could not be full resolved. So by starting with a thick slice and gradually going to smaller slices, one could determine the resolution when a slice thickness no longer matched the FWHM.

Experimental Setup and Procedure

All experiments were performed using a Bruker AVANCE 300MHz spectrometer with a 60mm diameter Super-Wide Bore (SWB) probe, the same probe to be used in the future experiments with the TEMCO core holder. Three circular chunks were cut out of a

flat sheet of rubber. One cut out of the thin sheet of rubber and two cut out of the thicker sheet of rubber. Three thicknesses could be created: the thin one which was 1.68mm thick, one chunk of the thick one which was 3.15mm thick, or two stacked chunks of the thick one which was 6.3mm thick. At first it was thought to put all the different sizes together in one image separated by 6mm of a material that yielded no signal, but as will be shown, it proved difficult to accurately distinguish the different thickness. Therefore, it was decided to do each thickness on its own.

A plastic tube with a Teflon platform inserted in it was used to set the rubber sample on and placed inside the 60mm probe. First, the tube was inserted into the probe to obtain a background image and then the rubber slice was placed on the Teflon platform and imaged using the ZTE sequence with the optimum parameters discussed earlier. Each rubber slice thickness was imaged and then analyzed in Prospa. Each image was background subtracted and a sagittal section was taken from the middle of the 3D ZTE image matrix allowing a 2D side profile to be seen of the thicknesses of the rubber samples.

Results and Discussion

As mentioned above, it was first thought to put all the different thicknesses together each separated by 6mm of material that yielded no signal so as to image them all in one go. Due to bleed through as well as the very slight signal obtained from the separating material however, this approach made it hard to accurately distinguish the FWHM of each rubber thickness. This is depicted in Figure 34 where the left bump represents the 6.3mm sample, the middle bump represents the 3.15mm sample, and the

right bump represents 1.68mm sample. The orange line represents one row of the 2D sagittal image and the red line represents an average off all rows in the sagittal 2D image. As seen, it is hard to distinguish a FWHM of each bump as the bumps are not sufficiently separated.

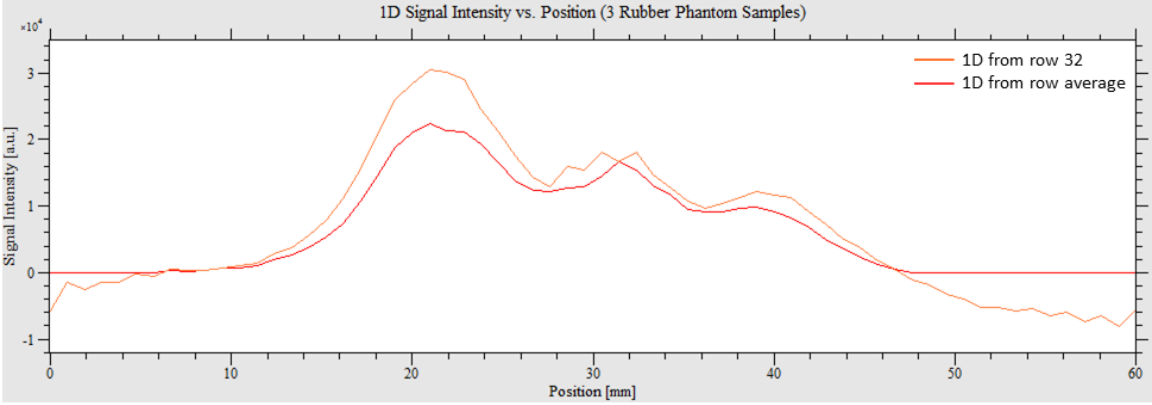


Figure 34: Signal intensity vs. position for 3 rubber phantom samples

So it was decided to image each rubber thickness on its own. Figure 35 depicts the 1D average intensity versus position for the 6.3mm rubber phantom. At FWHM the thickness is about 6.4mm. This is only 1.59% from the actual value, 6.3mm.

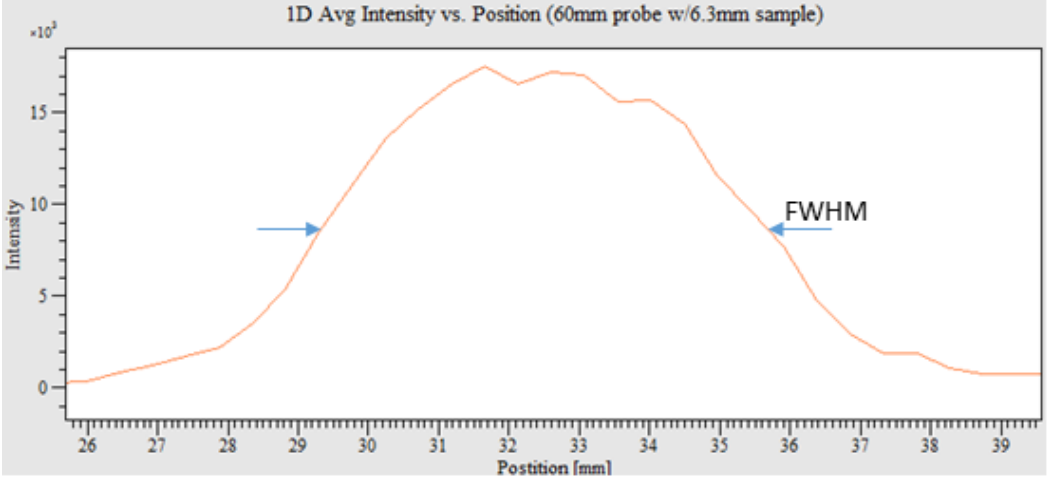


Figure 35: Signal intensity vs. position for 6.3mm phantom sample

Figure 36 depicts the 1D average intensity versus position for the 3.15mm rubber phantom. The thickness at FWHM is found to be about 3.5mm. This is a small 11.11% from the actual value of 3.15mm.

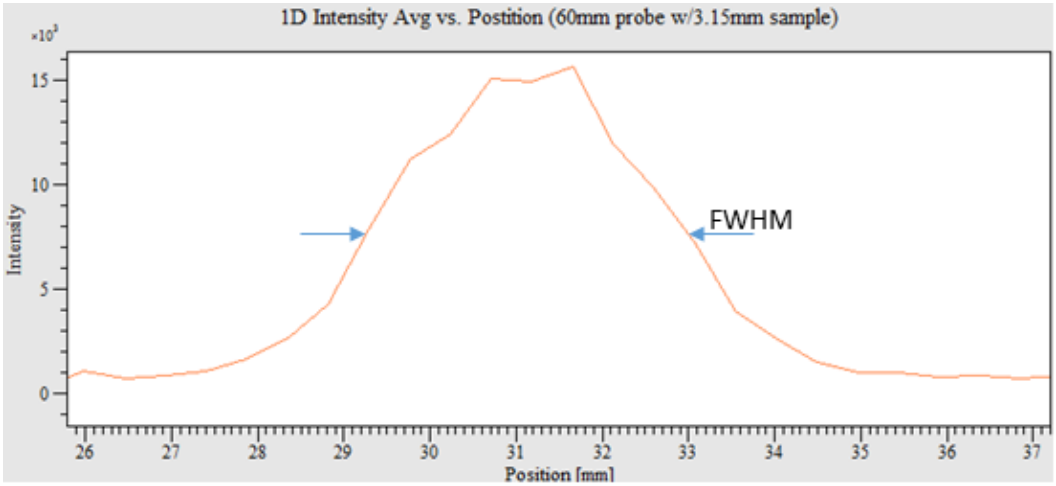


Figure 36: Signal intensity vs. position for 3.15mm phantom sample

Finally, Figure 37 depicts the 1D average intensity versus position for the 1.68mm rubber phantom. The thickness at FWHM is found to be about 2.9mm. This is significantly different than the actual value of 1.68mm by 72.62%.

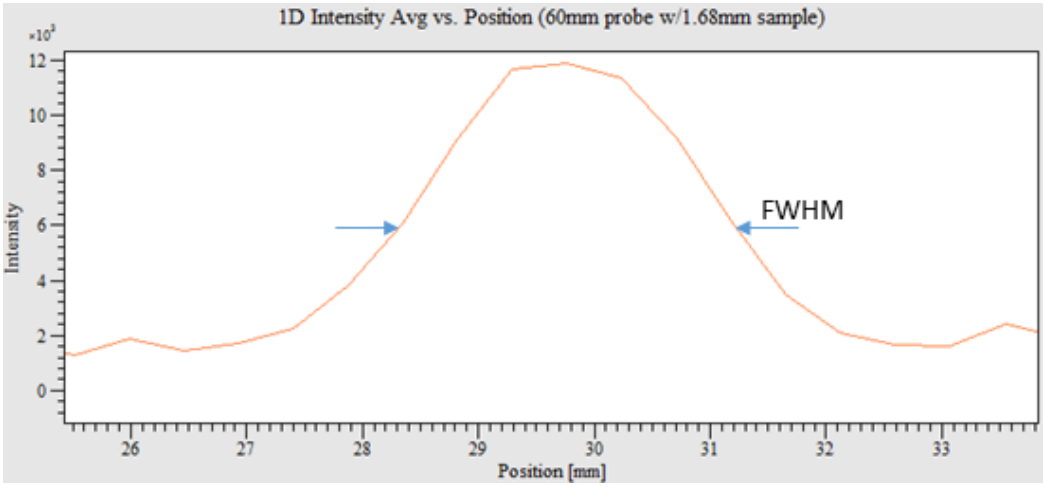


Figure 37: Signal intensity vs. position for 1.68mm phantom sample

Conclusions

Table 1 summarizes and compares the data for each phantom thickness. Clearly, the 6.3mm phantom is able to be fully resolved as the percent error is only 1.59%. The error for the 3.15mm sample yields about 11.11% which is not negligible but still small enough to conclude that this thickness can be mostly resolved. The broadening of the 1.68mm sample to 2.90mm suggests that anything smaller than 2.90mm would not be resolved. This in combination with the small percent difference of the 3.15mm sample suggests that this sequence with given parameters and setup has an actual resolution of around 3mm.

Table 1: Phantom FWHM comparison to actual thickness

60mm Probe	**6.3mm Sample**	**3.15mm Sample**	**1.68mm Sample**
FWHM	6.4mm	3.5mm	2.90mm
Error	1.59%	11.11%	72.62%

4. T1 AND T2 PRESSURE DEPENDENCE STUDY

Introduction

T_1 and T_2 measurements in NMR provide fundamental knowledge of the system at hand by describing the longitudinal and transverse relaxation of the nuclear spin ensembles, more information can be found on longitudinal and transverse relaxation under the relaxation section in the Nuclear Magnetic Resonance Theory chapter. The relaxation times are an indication of whether molecular motion is more solid or liquid-like, provide a distinction between different liquids or solids, whether something is contained in a large or small pore, whether there are surface interactions, magnetic field susceptibilities or inhomogeneities, and many other things [16, 21]. It is therefore important to be sure that these relaxation measurements are correct and accurate. Otherwise, the data could be misleading or interpreted wrong. Since most of the future experiments were going to be conducted at various high temperatures and pressures, it was the purpose of this experiment to determine any dependence of T_1 and T_2 relaxation times on pressure. It is already known that there is a dependence on temperature due to a change in the thermal energy causing increased or decreased molecular interactions [22, 23]. Therefore, there is only a need to focus on pressure dependence in this experiment.

Experimental Setup and Procedure

Setup

All experiments were performed using a Bruker AVANCE 300MHz spectrometer with a 60mm diameter Super-Wide Bore (SWB) probe. The flow loop is depicted in

Figure 38. A custom TEMCO FCH core holder designed for high-field NMR retained the high pressure fluid. There are two regions within the core holder separated by an FEP heat shrink sleeve. The outer region contains the confining fluid, Fluorinert, and the inner region contains the DI H_2O in a 20mm diameter PEEK tube. The confining fluid is maintained at a higher pressure which tightly squeezes the FEP sleeve around the PEEK tube restricting fluid from flowing around the outside. A partial cross section is shown in Figure 38.

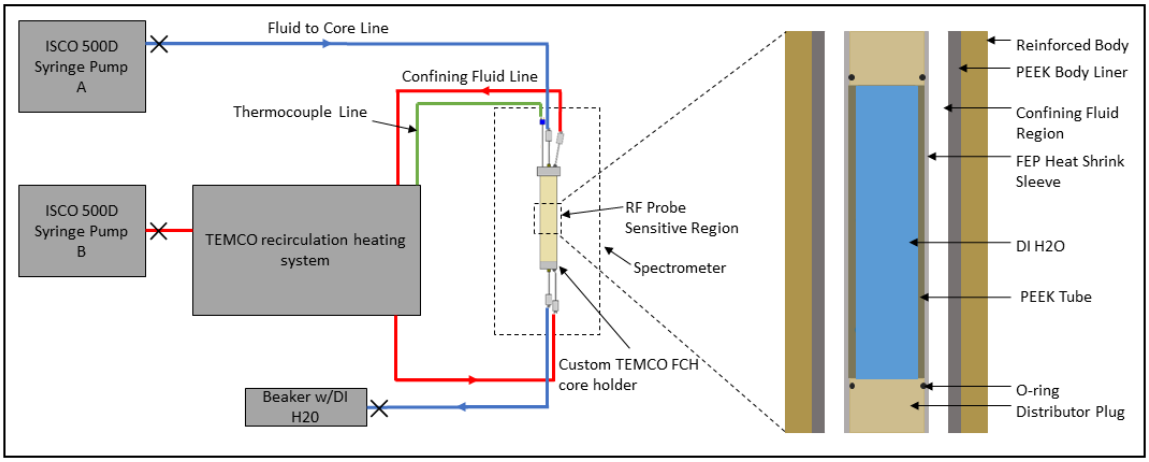


Figure 38: Experimental setup for pressure dependence study

Two ISCO 500D syringe pumps were used to provide the desired pressures and flow rates. One pump was designated to maintain pressure and flow of fluids through the bead pack while the other pump was designated to provide the confining pressure. A TEMCO recirculation heating system provided the necessary power to heat the confining fluid which, in turn heated the fluid going through the bead pack, which was monitored via a thermocouple. On the outlet end of the core holder, a line ran to a beaker that caught DI H_2O as it was pumped through the system. The system could then be pressurized after

it was saturated with H_2O, ensuring there was no air in the system, and the valve to the beaker was closed.

Procedure

The procedure for this experiment is fairly straight forward. The system is first setup as depicted in Figure 38. The confining fluid was pressurized to 6.89bar (100psi) and the temperature was set to 35^oC representative of the supercritical temperature to be used in future experiments. DI H_2O doped with Magnevist, used because future experiments were going to be using Magnevist and the same conditions wanted to be studied, was then pumped through the system at 0.689bar (10psi) until a steady flow began to pour into the beaker. This was done to ensure that the air was completely out of the system so as not to cause magnetic susceptibilities and compression issues. The valve was then shut and pressure equilibrated.

Once the system temperature and pressure was equilibrated, T_1 and T_2 measurements were made. The pressure was then increased to 13.79bar (200psi), maintaining the confining pressure 6.89bar (100psi) above the system pressure at all times, and another T_1 and T_2 measurement were made. This continued in 13.79bar (200 psi) increments up to 124.13bar (1800psi), being careful to maintain constant temperature. The obtained data is presented in the following section in Figure 39 andFigure 40.

Pulse Sequences

The two pulse sequences used for this experiment are the inversion recovery and CPMG pulse sequences. They are described in the Basic Pulse Sequences and Spin

Manipulation section of the Nuclear Magnetic Resonance Theory chapter. The inversion recovery sequence is used to determine the time constant T_1. For a pulse power of -2dB, a 90^o pulse was achieved with a pulse time of 103.5μs and 180^o pulse was achieved with a pulse time of 207.0μs. A TD=2048 and DW=50μs were used to acquire the signal with two averages, NS=2. The list values for the inversion time points were as follows: 0.001, 0.071, 0.142, 0.214, 0.285, 0.357, 0.428, and 0.500s.

The CPMG pulse sequence is used to determine the time constant T_2. The same pulse times and power were used to achieve the 90^o and 180^o pulses. To acquire the FID the following parameters were used: TD=56032, D3=400μs (Tau), DW=10μs, D4=D6=DW, and L22=700 (number of echoes). In order to acquire a steady state signal and increase the signal to noise, 3 dummy scans, DS=3, and 8 averages, NS=8, were used.

Results and Discussion

The T_2 values acquired from the CPMG scans are depicted in Figure 39 and the T_1 values acquired from the inversion recovery sequence are depicted in Figure 40. Both are plotted against pressure in order to determine any trends as the pressure is increased. The first point at 0.689bar (10psi) in Figure 39 is not comparable to the rest of the data. An error was made in the first scan and the scan was not redone until all the other data was collected. Upon depressurizing and redoing the 0.689bar (10psi) scan it was noticed that the temperature had decreased by about half a degree Fahrenheit. Therefore, the difference is attributed to the temperature and not pressure. Had the scan been conducted at the same temperature it would be expected to fall somewhere at or slightly above the

T_2 value at 13.79bar (200psi). However, the overall trend shows a general decrease in the transverse relaxation, about 12ms over a large pressure range of 110.34bar (1600psi). The change in T_2 is only about 4.8% of the maximum T_2 value. This decrease makes sense as an increase in pressure compresses the substance, even though the substance is considered incompressible it does compress albeit very minutely, causing molecular interactions to increase, restricting the molecules rotational diffusivity and leading to a faster relaxation [24].

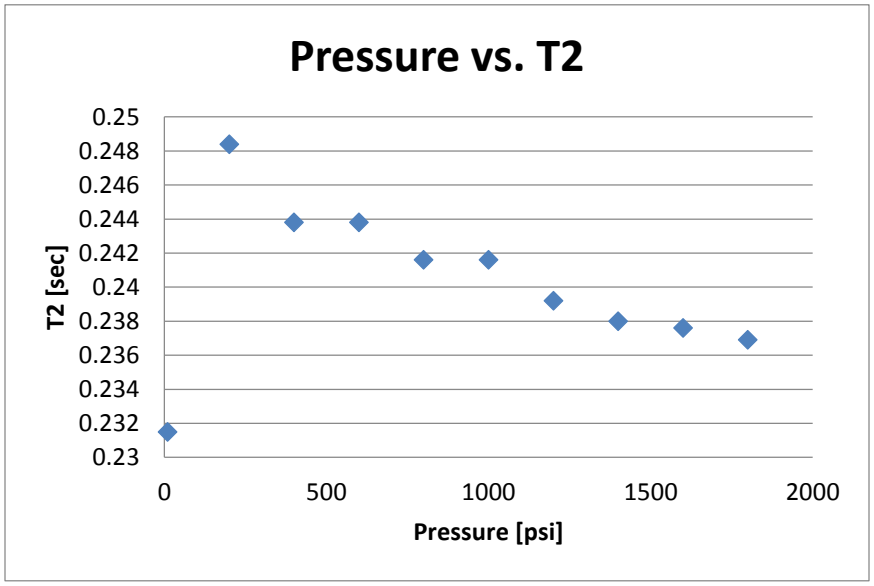


Figure 39: Pressure versus T_2 relaxation for doped DI H2O

Again, the first point in Figure 40 is not comparable to the rest of the data for the same reason as mentioned above, the scan was redone after all others were conducted and it was noticed that the temperature had decreased by about half a degree Fahrenheit. The overall average trend in the data is a decrease in T_1 with increasing pressure. The T_1 decreases about 3ms over a pressure range of 110.34bar (1600psi). The change in T_1 is only about 1.0% of the maximum T_1 value. However, when considering the error bars the

data is nearly statistically the same. This is consistent with the data in [25], as over a range of pressures that extend to 9000 bar (130533.96psi) , about 65 times that in this experiment, a change in the T_1 of about 27% is noticed at 30°C, where in the range considered in this experiment there is no distinguishable change.

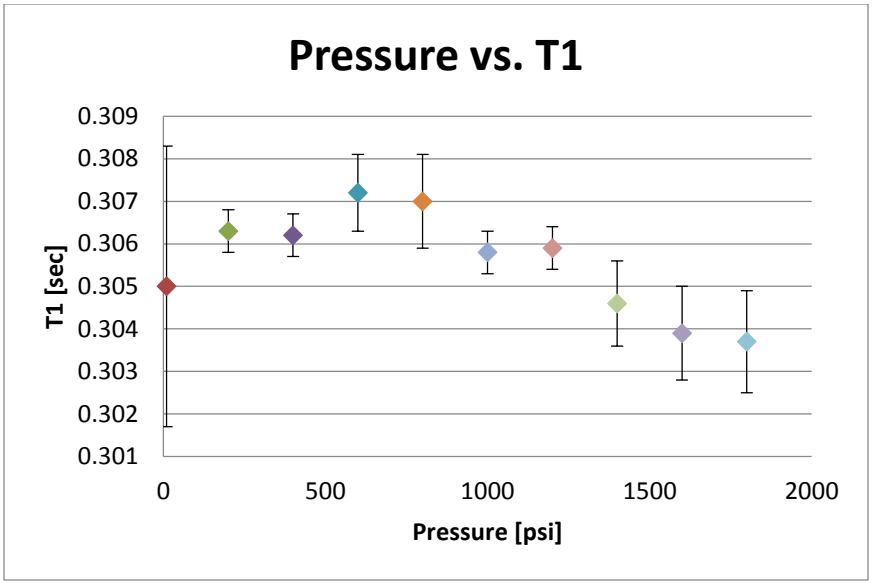


Figure 40: Pressure versus T_1 relaxation for doped DI H2O

Conclusions

The purpose of this experiment was to determine the pressure dependence on relaxation times in order to ensure experimental accuracy and correctness. Considering the change in the characteristic relaxation times when compared to their maximum value, the change is nearly insignificant. T_2 changes by about 4.8% and T_1 changes by about 1.0%. Therefore, it is concluded that the relaxation times' dependence on pressure is negligible. As a side note, experiments will be carried out at a constant temperature and pressure therefore any data will be comparable.

5. VISCOUS FINGERING EXPERIMENTS

Introduction

Nuclear magnetic resonance (NMR) techniques have been utilized to study the dissolution of scCO_2 in water in a porous media under conditions representative of that in a deep underground saline aquifer. CO_2 is essentially immiscible in water at room temperature conditions. By increasing to supercritical conditions, representative of a deep underground saline aquifer, the CO_2 becomes miscible in water. According to [26], the solubility of CO_2 in H_2O at conditions conducted in this experiment, T = 35^{o}C and P = 100bar (1450psi), is approximately 1.287 mol/kg or about 2.3%. This percent, although small, should cause the NMR signal to decrease as CO_2 dissolves into the H_2O, restricting the mobility of the ^{1}H hydrogen atom and impacting the relaxation mechanisms. Thus, as dissolution occurs the NMR signal will decrease and the dissolution of CO_2 into water can be monitored. It is the goal of this work that the interface between the CO_2 and water can be monitored moving over time from which a flux could be obtained, much like that of the work in [12] in which numerical simulations of the convective dissolution of MEG into water were conducted. It is therefore the focus of this experiment to extrapolate a dissolution rate for CO_2 into water and to measure the viscous fingering phenomena in which convective dissolution occurs, further enhancing the dissolution rate, as discussed in the introduction of this thesis. Determining the dissolution rate and studying the viscous fingering phenomena could provide valuable information on the CO_2 sequestration process, leading to enhanced storage security and process optimization.

Experimental Setup and Procedure

Setup

All experiments were performed using a Bruker AVANCE 300MHz spectrometer with a 60mm diameter Super-Wide Bore (SWB) probe. The flow loop is depicted in Figure 41. A custom TEMCO FCH core holder designed for high-field NMR retained the high pressure fluids and housed the porous media. There are two regions within the core holder separated by an FEP heat shrink sleeve. The outer region contains the confining fluid, Fluorinert, and the inner region contains the 180-212 μm borosilicate glass microspheres in a PEEK tube with Berea rock core caps. The confining fluid is maintained at a higher pressure which tightly squeezes the FEP sleeve around the PEEK tube restricting fluid from flowing around the outside. A partial cross section is shown in Figure 41.

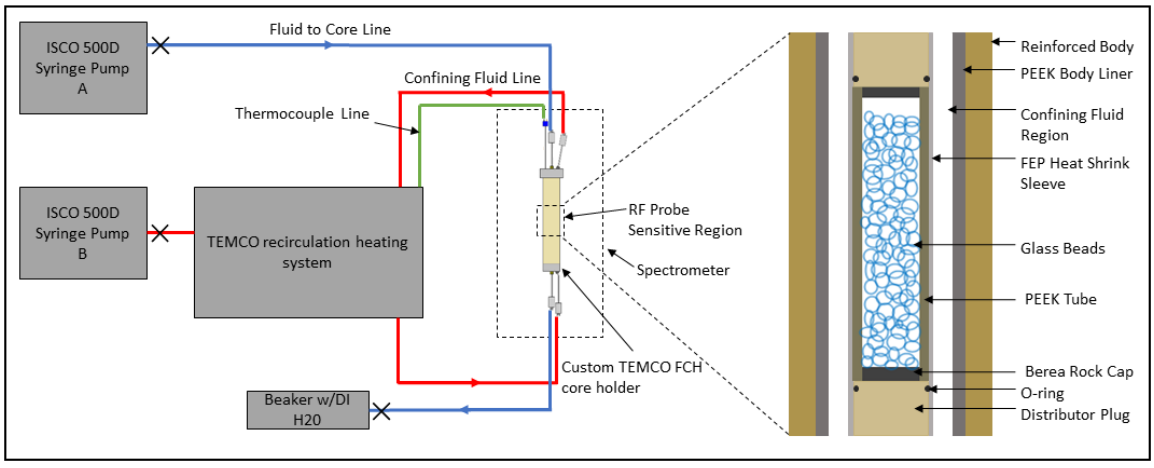


Figure 41: Experimental setup for viscous fingering experiment

Two ISCO 500D syringe pumps were used to provide the desired pressures and flow rates. One pump was designated to maintain pressure and flow of fluids through the

bead pack while the other pump was designated to provide the confining pressure. A TEMCO recirculation heating system provided the necessary power to heat the confining fluid which, in turn heated the fluid going through the bead pack, of which was monitored via a thermocouple. This allowed for supercritical temperatures to be reached. On the outlet end of the core holder, a line ran to a beaker with DI H_2O in it from which water could be drawn into the bead pack to a certain level by reversing the pumps. The system could then be pressurized after closing the valve to beaker.

Procedure

One five day experiment was conducted in which a head of $scCO_2$ was placed on top of DI H_2O, doped with Magnevist, in a bead pack at conditions representative of a deep saline sandstone aquifer. This experimental setup effectively replicates the CO_2 sequestration scenario in which a buoyant plume of $scCO_2$ has been trapped by a cap rock and is on top of a denser brine layer, all within a porous sandstone, at which point convective dissolution begins to take place, as discussed in the introduction of this thesis.

The beads were carefully placed in a 20 mm diameter by 100 mm long PEEK tube with the bottom Berea rock cap in place and filled slightly less than full so as to leave a small gap at the top to more clearly see the interface between the bead pack and the head of CO_2. The top Berea rock cap was then inserted. The rock caps were used not only to hold the beads in place but, also to provide a permeable barrier that would protect the bead pack from any sudden velocity surges that may disrupt the bead pack and interface. After this the apparatus was setup according to Figure 41.

Once setup, CO_2 at ambient conditions was pumped through the core at 10 ml/min bubbling it in the beaker filled with DI H_2O doped with 0.19%-vol Magnevist. The bubbling ensured that the system was completely purged of anything but CO_2 and that when stopped no air would diffuse back into the system. After bubbling, the pumps were reversed drawing DI H_2O back into the system at 0.5 ml/min until it reaches the bead pack and then slowed to 0.25 ml/min.

The H_2O entering the bead pack was monitored by single pulse FID and 1D spatial profiles. The 1D spatial profiles scan was used to fill the bead pack to a point where the CO_2/H_2O interface was in the top 3/4s of the sensitive region in the RF coil. This was done so that the interface could still be monitored as well as any dissolution down into the saturated bead pack. A ZTE image was then taken assuring the location of this interface was distinctly defined and in the appropriate position. Once the appropriate position was obtained the pump was shut off and the valve to the beaker was closed.

The recirculation heating system was then turned on to reach the supercritical temperature of 35^{o}C. The pressure was slowly increased to a supercritical condition, 100bar (1450psi) while maintaining an overburden pressure 6.89bar (100psi) greater. Once the system was equilibrated, imaging began. The system was allowed to sit for 5 days capturing ZTE and MSME images every 2 hours. The MSME images were used to find the relaxation time T_2 as well as the 2D intensity images. The MSME intensity images were also compared against the ZTE images since this was the first big experiment using the ZTE sequence and the MSME was an already trusted sequence.

Pulse Sequences

Four main pulse sequences were used to capture the necessary data: a single pulse FID acquisition, a 1D spatial profile position-z, ZTE (zero echo time), and MSME (multi-slice multi-echo). The single pulse sequence is the most basic pulse sequence used to simply detect signal. A 90^o RF pulse is applied to the sample and a FID is obtained. The FID is Fourier transformed to yield a spectra in the frequency domain. Since the signal is tuned to detect ^1H nuclei, the signal is from the water protons. The more water the greater the signal and the larger the intensity of the spectra. A 90μs RF pulse with a power level of -3.0dB was used to achieve a 90^o RF pulse.

The second sequence used is the position-z sequence. The sequence is like the one discussed in Figure 21 of the gradients section in the Nuclear Magnetic Resonance Theory chapter. The application of a linear magnetic field gradient in the z direction after the application of a 90^o RF pulse will result in a spectra with frequencies that are dependent on spin position along the z axis and signal intensity that is proportional to the number of spins associated with a certain position. Thus a cylinder full of water placed lengthwise along the z axis would yield a spectra of a 1D profile of a rectangle when a position-z scan is utilized. The same 90^o RF pulse was used in this sequence. A bandwidth of 50000Hz was sufficient to spectrally view the length of the sample. A FOV along the z axis of 100 mm with 128 pixels was more than enough to capture the signal in the entire tube. A repetition time of 5000ms was used to ensure the signal returned to equilibrium before another pulse was applied.

The third pulse sequence used was the multi-slice multi-echo (MSME) pulse sequence depicted in Figure 42. This sequence is used to acquire 2D slice selected images

with different T_2 weighting. This sequence is similar to the spin-echo sequence described in Figure 18 and Figure 24 except that a slice selective gradient is used to select a specified slice of desired thickness in the third dimension and that an echo train of a specified number of echoes is used to obtain multiple T_2 weighted images, the number of images dependent on the number of echoes.

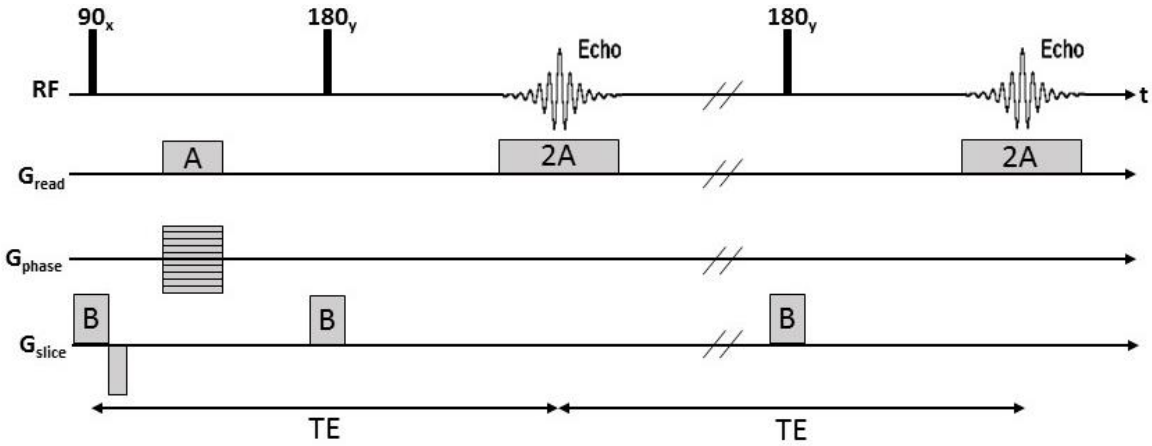


Figure 42: Multi-slice multi-echo (MSME) pulse sequence

A particular use of this sequence is that, along with acquiring a 2D image, the spin-spin relaxation time can be determined because the signal acquired at each successive echo is attenuated by transverse relaxation. From the successive attenuated 2D images a relaxation map like that depicted in Figure 47 can be created and the T_2 value can be found for a particular location within the image. A selective sinc3 pulse was used with a 0.97ms pulse length at 3dB in order to achieve a 90^o pulse exciting a bandwidth of 6402 Hz. 16 echoes with an echo time (TE) of 10.21 ms was used from which a relaxation map was created from the attenuated 2D images. 1 axial slice of 0.5 mm was

selected with a FOV of 32x32 mm and a matrix size of 64x64 yielding a resolution of 0.5 mm/pixel.

The final pulse sequence used in this experiment was the zero echo time (ZTE). The ZTE sequence is depicted and discussed in both Figure 25 and Figure 32. In order to resolve the spectral information a band width of 65789 Hz was used with a 19.5 μs pulse at 4.7 dB and a tip angle of 8^o. A FOV of 32x90x32 with a matrix size of 128^3 was sufficient to capture the desired image without creating any artefacts. A repetition time (TR) of 3.84 ms was used in order to ensure the magnetization returned to equilibrium before the next RF pulse was applied.

Results and Discussion

Imaging of CO_2 Pulse through Saturated Rock Core

Before the experiment was carried out another experiment was conducted to evaluate if it was even possible to adequately image a saturated core, image a CO_2 pulse passing through the core, and distinguish between water and CO_2 within the pores. The idea was to image a completely dry rock core for an initial reference and background subtraction and then saturate the rock core with H_2O and bring it up to supercritical pressure and temperatures, 75.86bar (1100psi) and 35^oC. Then pump CO_2 into the rock core displacing the water in the pores. ZTE images would be taken continually to monitor any changes in the rock core and saturation. Figure 43 depicts what the anticipated 1D profile would look like when a pulse of CO_2 passes through a saturated rock core. Green represents a fully saturated core with the blue representing the transit of the CO_2 pulse through the rock core and red representing a drained rock core.

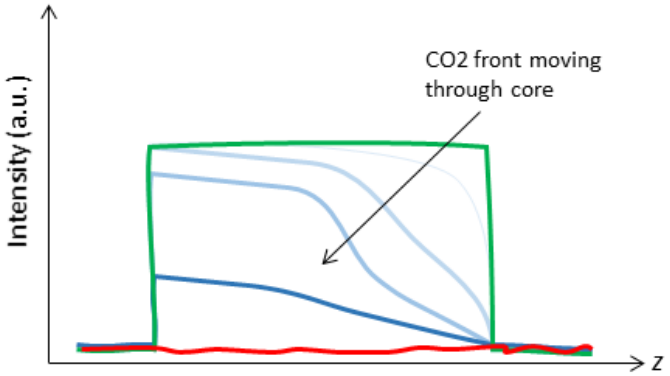


Figure 43: Expectation of 1D ZTE data for CO_2 pulse

The results of this experiment are depicted in Figure 44 and Figure 45. Figure 44 displays the 1D intensity profile during the course of draining the rock core, similar to the anticipated depiction in Figure 43. The core does drain and decrease in signal, meaning water is being displaced out of the core. However, it does not completely remove all of the water from the core, as noted by the remaining signal after the pulse has moved through the rock core.

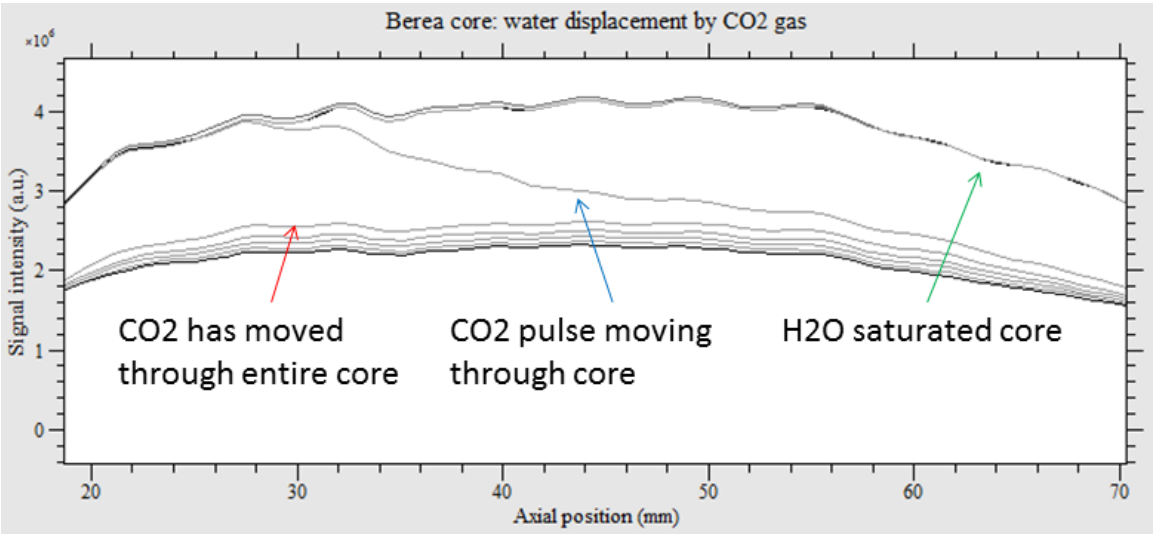


Figure 44: 1D ZTE data for CO_2 front moving through rock core

Figure 45 shows the same water being displaced as the CO_2 pulse passes through the core but as a 2D image, both axial and sagittal. These images are achieved after a background subtraction yielding only the signal from the water in the rock core. As the pulse passes through the rock core the signal from the water clearly attenuates. Thus these figures show that a rock core can be adequately imaged during saturation and drainage and that the CO_2 and water can be distinguished.

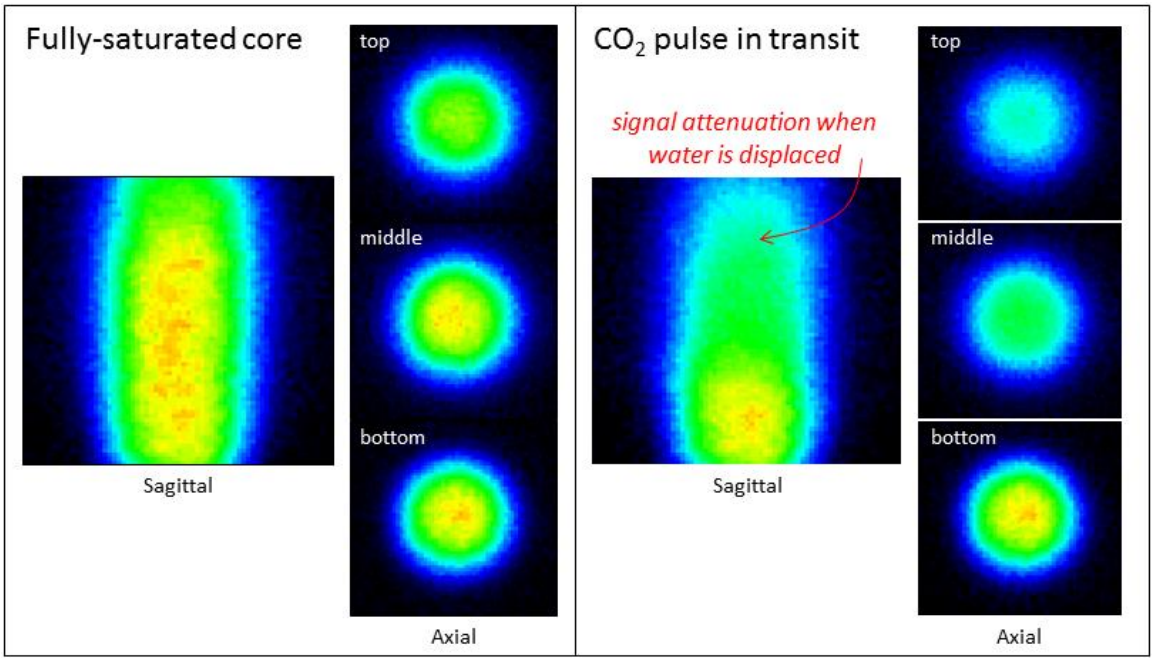


Figure 45: 2D ZTE data for CO_2 front moving through rock core

Viscous Fingering Experiment

After verifying the plausibility of imaging a CO_2 pulse passing through rock core, the five day experiment was conducted in order to try and capture the CO_2 dissolution in the porous media as well as the viscous fingering phenomena which leads to convective dissolution further enhancing mass transfer. The setup and procedure were previously explained.

The intention of this experiment was to have a clear interface between the water and $scCO_2$, as depicted in the left ZTE image of Figure 46, in which the dissolution into the bead pack could be clearly monitored along with the movement of the interface and any fingering that might take place and be visible. However, as depicted in the right ZTE image in Figure 46, there was a pressure inversion incident upon pressurizing the system. It can be seen that the interface has moved into the bead pack but still remains fairly distinct. Therefore, the experiment was allowed to continue with the new interface.

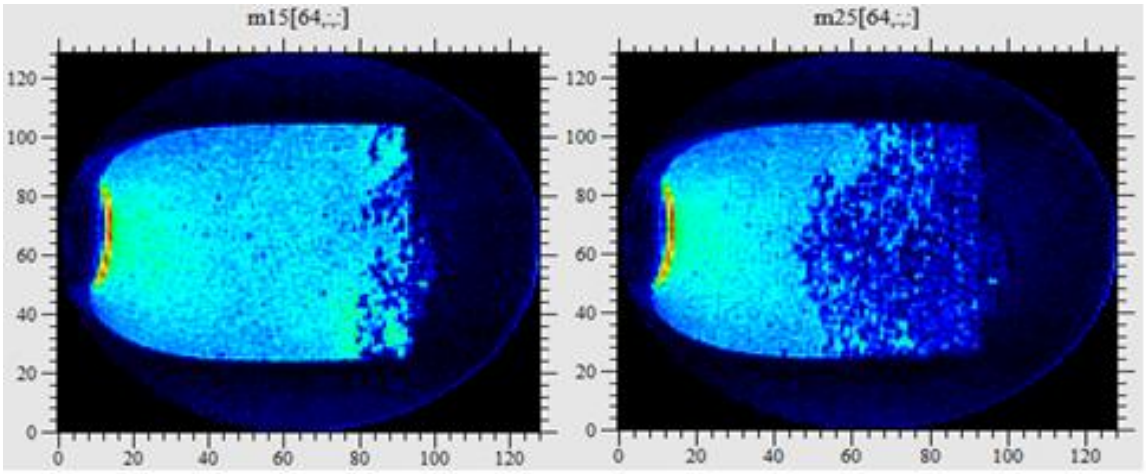


Figure 46: Before and after images from pressure inversion incident

As mentioned above relaxation maps were made from the MSME sequence, in which one can spatially distinguish the spin-spin relaxation times within the bead pack. Figure 47 depicts what these maps look like with red and yellow being the longest relaxation times moving down to blue and black being the fastest relaxation times. Therefore, it makes sense that in the region where CO_2 has penetrated into the bead pack and mixed with water that the relaxation times are shortened due to CO_2's molecular interactions with the hydrogen ions in water [27]. The red and blue lines indicate the

position in the bead pack that Figure 49 and Figure 50 are associated with where the red line is below the interface in the water saturated region and the blue line is above the interface in the CO_2 saturated region.

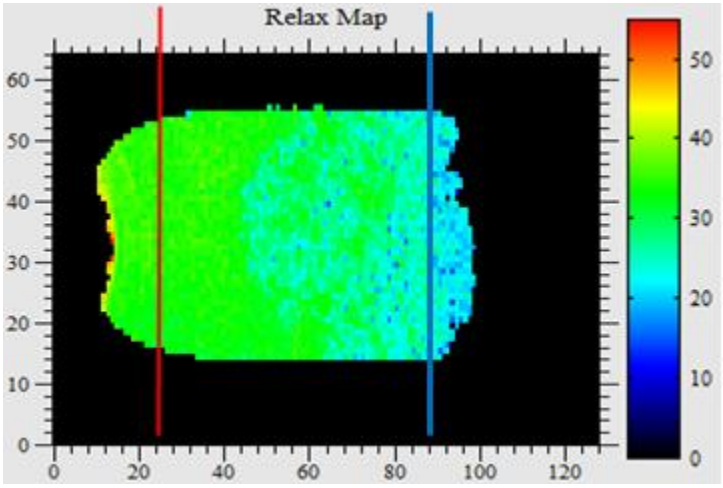


Figure 47: Relaxation map with red and blue lines indicating where T_2 progressions were taken from

Figure 48 is 34 average 1D profiles, averaging the signal across the diameter of the tube, each created from its associated relaxation map that was made from the chronologically taken MSME images. Therefore, this gives us an idea of how the relaxation times associated with a longitudinal position in the bead pack changed over the several day period. Again, the red and blue lines indicate the position in the bead pack that Figure 49 and Figure 50 are associated with. It's hard to distinguish any change over the experiment duration of the relaxation times and associate that with a position in Figure 48 because the lines are all so close together. Therefore, in order to distinguish the difference in time Figure 49 and Figure 50 where made.

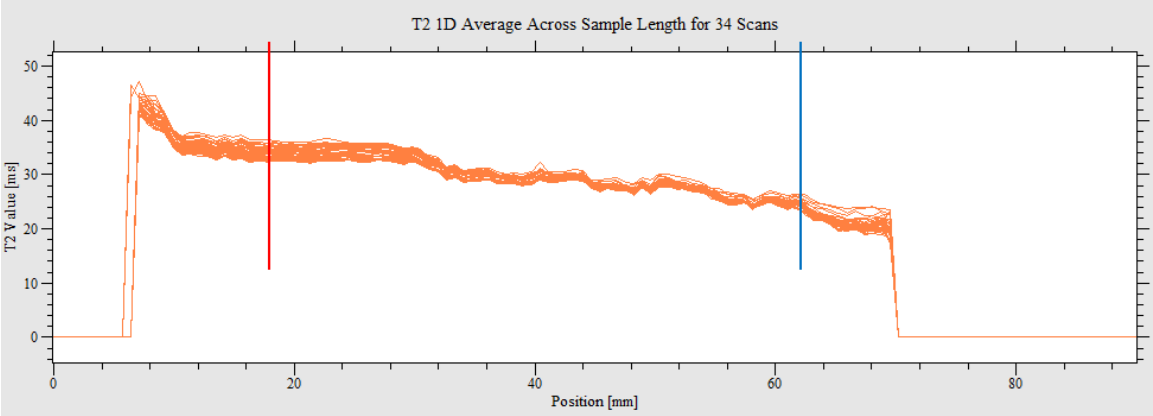


Figure 48: T_2 1D average across length of sample for all 34 scans

Figure 49 represents the change in time of the T_2 relaxation time associated with the position as indicated by the red line in Figure 48. It can now be clearly seen that the relaxation time is consistently decreasing at this position. It changes from ~36.8 ms to ~33.5 ms which is a decrease of about 8%. This makes sense as the dissolution of the CO_2 into the water would decrease the relaxation time [27].

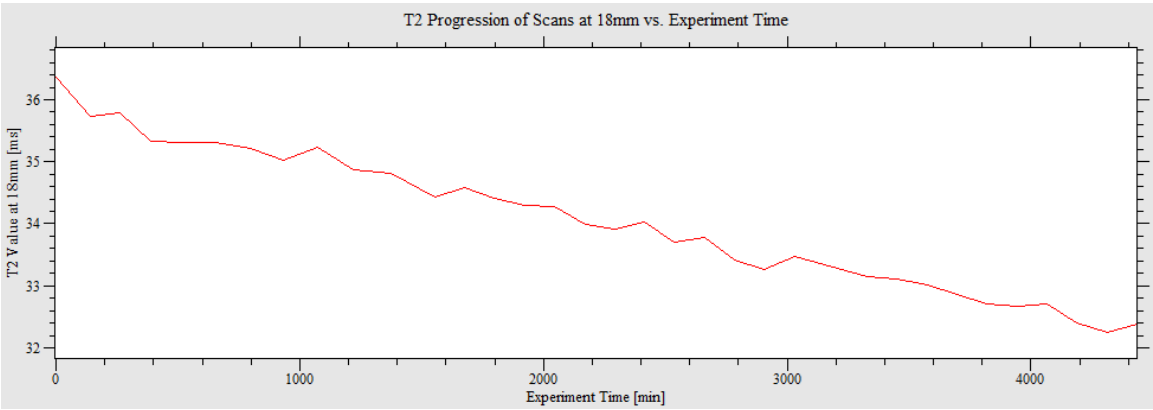


Figure 49: T_2 progression of scans at position 18mm versus time

Figure 50 represents the change in time of the T_2 relaxation time associated with the position as indicated by the blue line in Figure 48. Initially, it appears there is a small decrease in the relaxation time but as time goes on the relaxation times begin to increase.

It changes from ~24 ms to ~26.5 ms which is an increase of about 9%. This is unexpected but may possibly be explained by an increase of pure water (that which has no dissolved CO_2 in it) in the pores at this position. As the CO_2 above dissolves into the water and creates a denser layer of CO_2 and water that then fingers down into the water saturated bead pack, because of mass conservation, it would displace water into the upper portion of the bead pack. This is a viable hypothesis but still remains unclear, in part because only 2.3% of the CO_2 is dissolvable in water at these conditions and the spectrometer is unable to clearly resolve this difference.

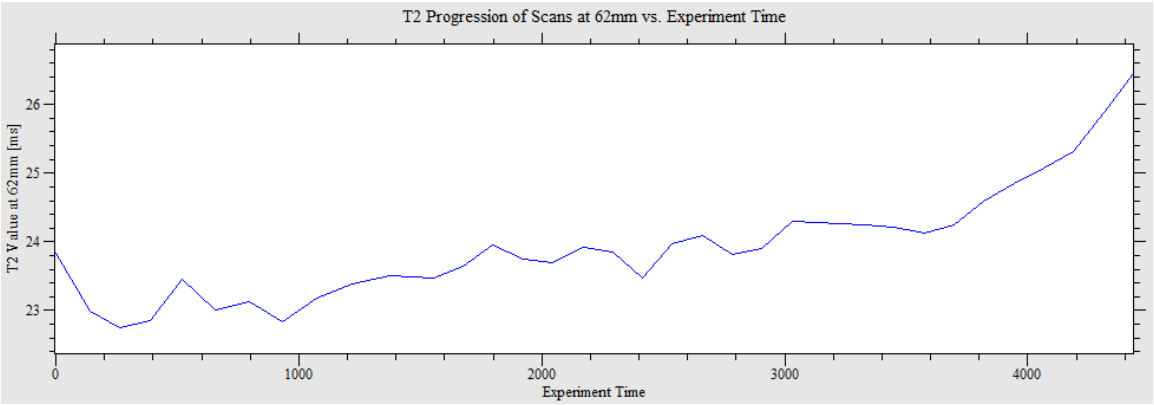


Figure 50: T_2 progression of scans at position 62mm versus time

The following two figures depict the 1D average signal intensity along the z-direction, lengthwise along the tube as in the previous figures, for the MSME data and the ZTE data over four days. Notice the data starts on day two as the pressure inversion incident took place on day one, skewing the data. Therefore, it was removed to reflect the new interface position as shown in Figure 46. In Figure 51, although slight, it appears that in the bottom half of the tube the signal intensity decreases and in the top part of the tube the signal intensity increases, especially in the last day. This helps to corroborate the

previous T_2 relaxation time hypothesis in that more water is displaced into the upper pores as the CO_2 mixes with the water and plunges down.

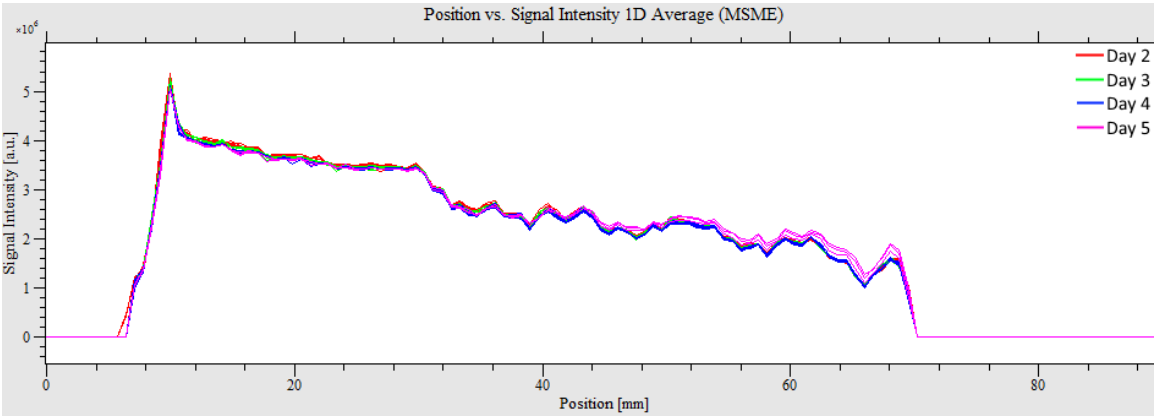


Figure 51: 1D average signal intensity vs. position (MSME scans)

Figure 52 shows similar data as in Figure 51 except a different pulse sequence was used to obtain the data, the ZTE sequence which is weighted for T_1 relaxation rather than T_2. This data, however, does not show any significant trend over time. The lines remain more or less on top of each other. This difference can be attributed to the pulse sequences themselves. The MSME sequence has a higher signal to noise because more averages are done and has a finer resolution whereas the ZTE sequence is done quickly with minimal averages leading to a smaller signal to noise ratio. Considering the minute changes that take place this hypothesis makes sense where the changes are barely noticeable in the higher signal to noise ratio pulse sequence.

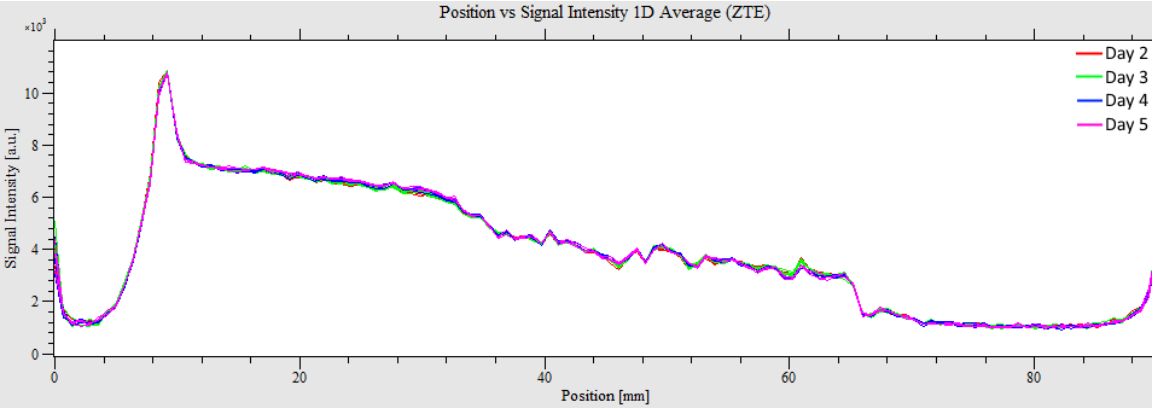


Figure 52: 1D average signal intensity vs. position (ZTE scans)

Conclusions and Future Work

Imaging the viscous fingering phenomena and quantifying the dissolution rate has proved to be a difficult task. Things that lend itself to the difficulty include: the very small amount of CO_2 that can dissolve into the water (just 2.3% at these conditions) leading to a small contrast in signal between the dissolved CO_2/water and the water, the inability for the imaging sequences to distinguish between the dissolved CO_2/water and just water itself because of this small percentage, the small amount of signal that can be detected, the inhomogeneities caused by the porous media, and the unknown timeframe and effect of viscous fingering on dissolution. This data has shown these difficulties but also suggests dissolution was occurring over these four days and that water was possibly being displaced by the dissolved CO_2, suggested by the T_2 relaxation data and the MSME data. Therefore, it is plausible that this phenomenon can be detected and studied but requires further testing and refinement.

In future work it would prove beneficial to take a step back and look at a more simplified system, such as removing the porous media and just having a head of CO_2 on

water. This would allow a higher signal to noise, a cleaner interface, and better resolution in hopes of being able to better visualize and quantify the viscous fingering to obtain a better understanding of the dissolution of CO_2 into water. Also, one might look into maximizing the dissolution percentage by finding the optimum conditions, therefore, increasing the contrast between the water and the dissolved CO_2/water.

Furthermore, it may prove beneficial to revisit the experiment that was conducted with maximized conditions being careful not to disrupt the CO_2/water interface, i.e., avoid a pressure inversion. The inversion could have affected the system in unforeseen ways, such as perturbing the whole system and causing a large amount of CO_2 to dissolve quickly, causing the system to behave differently and in a manner that doesn't represent the sought after phenomena.

6. CAPILLARY TRAPPING EXPERIMENTS

Introduction

Nuclear magnetic resonance (NMR) techniques have been utilized to noninvasively monitor the drainage/imbibition of air, CO_2, and $scCO_2$ with DI H_2O in a Berea sandstone rock core under conditions representative of a deep underground saline aquifer. This experiment is designed to mimic the capillary trapping mechanism discussed in the introduction of this thesis, in which, after CO_2 injection brine imbibes back into the pores trapping CO_2 ganglia via snap-off. Because of the thermophysical properties of $scCO_2$, analogue fluids used for simplification may not be representative of the actual processes under geologic conditions. Thus, this study will compare the capillary trapping of air with that of supercritical CO_2. Also, subcritical CO_2 will be compared to supercritical CO_2 in order to identify and analyze any distinctions in the supercritical state from its subcritical state. Furthermore, the distribution of W fluid in the pores will be monitored via NMR relaxometry in order to provide some insight into which pores may trap the NW phase and to track the drainage/imbibition through the pore structure. These experiments stemmed from the work done in [7].

Experimental Setup and Procedure

Setup

All experiments were performed using a Bruker AVANCE 300MHz spectrometer with a 60mm diameter Super-Wide Bore (SWB) probe. The flow loop is depicted in Figure 53. A custom TEMCO FCH core holder designed for high-field NMR housed the

rock core and retained the high pressure fluids. There are two regions within the core holder separated by an FEP heat shrink sleeve. The outer region contains the confining fluid, Fluorinert, and the inner region contains the rock core. The confining fluid is maintained at a higher pressure which tightly squeezes the FEP sleeve around the Teflon wrapped rock core restricting fluid from flowing around the outside of the core. A partial cross section is shown in Figure 53.

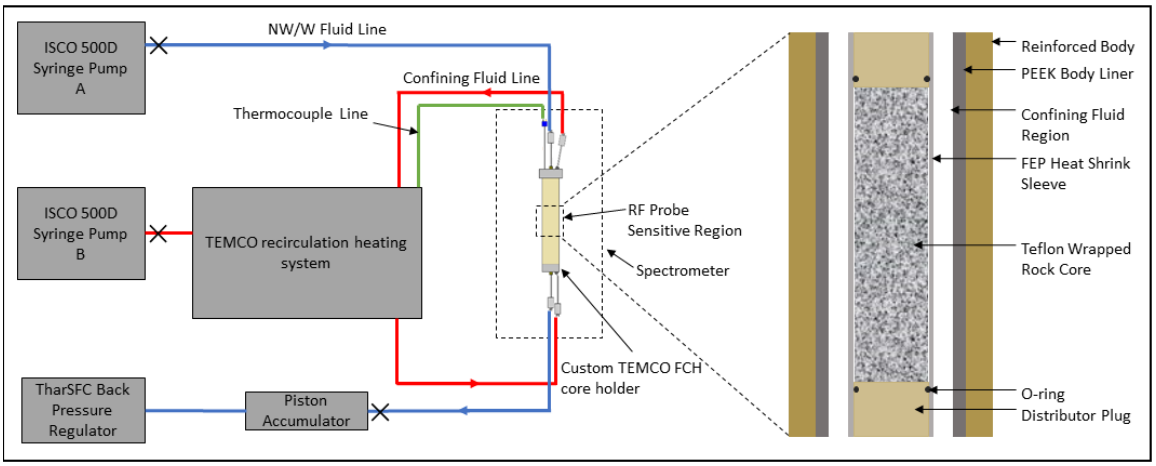


Figure 53: Experimental setup and cross section of core holder

Two ISCO 500D syringe pumps were used to provide the desired pressures and flow rates. One pump was designated to maintain pressure and flow of fluids through the rock core while the other pump was designated to provide the confining pressure. A TEMCO recirculation heating system provided the necessary power to heat the confining fluid which, in turn heated the fluid going through the rock core, of which was monitored via a thermocouple. This allowed for supercritical temperatures to be reached. Lastly, a piston accumulator attached to a TharSFC back pressure regulator allowed fluid to accumulate while maintaining the system at a constant pressure.

The rock cores used were a Berea Sandstone with dimensions of roughly 26mm in diameter and 97mm long. They were both cored from a larger block of sandstone and thus are expected to have similar properties listed in Table 2. Before heat shrinking the FEP sleeves around the rock core, a couple layers of Teflon tape was wrapped around the rock core to help seal the rough rock exterior against the FEP helping to prevent flow around the core.

Table 2: Berea Sandstone Properties

Sandstone	Dunham Classification	Porosity	Permeability
Berea	quartz arenite	~15%	~150mD

Procedure

Three separate drainage and imbibition experiments were performed on two different rock cores. Each experiment used either air, CO_2, or $scCO_2$ as the non-wetting (NW) fluid and DI H_2O, doped with 0.4%-vol Magnevist to enhance the signal, as the wetting (W) fluid. The drainage and imbibition experiment was then repeated for each rock core, for each NW fluid yielding a total of 6 experiments for each rock core. This duplication is done to help verify the results for each rock core as well as show any variations/similarities between rock cores. The results for each rock core are expected to be similar because these cores were taken from the same block of sandstone and because Berea Sandstone is fairly homogenous.

The experimental process is exactly the same for every experiment except for the difference in the chosen NW fluid. Every experiment was conducted at 75.86bar

(1100psi) and 70^{o}F for air/CO_2 or 95 ^{o}F in order for CO_2 to reach a supercritical state, scCO_2. The experimental steps were as follows:

1. The core is wrapped with Teflon tape, heat shrunk in the FEP sleeve, and placed into the core holder which is then placed into the probe in the spectrometer and fluid lines attached. A ZTE image is taken with the core completely dry to obtain a background image that is later used for background signal subtraction.
2. DI H2O doped with Magnevist is then pumped in saturating the core. It is then slowly pressurized to the desired 75.86bar (1100psi) at the same time maintaining the confining pressure 17.24bar (250psi) above the core pressure. The saturation is monitored via the FID produced by a modified single pulse sequence allowing for detection of very short T_2's. Once the FID area, representative of the amount of H2O in the sample, has stabilized, this is assumed to be maximum saturation and a ZTE image and 1D T_2 are taken for full saturation.
3. Once pressure has equilibrated at 75.86bar (1100psi), pump A is isolated and the fluid is switched to the desired NW fluid (air, CO_2, or scCO_2 if the heating recirculation system is turned on) and pumped into the core, simulating drainage, at 0.5ml/min corresponding to very low Ca numbers (≈ 2.72E-08, 2.39E-07, or 8.09E-08). It is pumped in for about 15 minutes until it appears the FID area has reached a fairly stable regime. Several ZTE images and 1D T_2's are taken during the drainage process with the final one taken at maximum drainage when the FID stabilizes.

4. Pump A is now isolated and the fluid is switched to DI H2O doped with Magnevist for the imbibition phase. The water is pumped in at 0.5ml/min corresponding to low Ca numbers (≈ 1.38E-06, 3.21E-06, or 3.50E-06). It is pumped in for about 10 minutes until the FID area has stabilized and reached an equilibrium like state. A ZTE image and 1D T_2 are taken after stabilization and represent the final imbibition saturation, the residual saturation.
5. The core is then removed, oven-dried, and placed in a vacuum in order to ensure all water and NW phase have been removed so the beginning conditions of the rock core remain the same for every experiment.

Pulse Sequences

Two main pulse sequences were used in order to capture the necessary data: zero echo time (ZTE) and CPMG. The CPMG pulse sequence is a basic spin echo pulse sequence that consists of a 90^o RF pulse followed by sequential 180^o pulses that induce spin echoes. These spin echoes create an exponential decay envelope. Since the envelope of decays is determined only by T_2 relaxation, the time constant T_2 can be determined. For samples where multiple T_2's may be present, such as in porous media with different pore sizes, a multi-exponential decay envelope is obtained. An inverse Laplace transform (ILT) algorithm is then used to create a 1D distribution of T_2 values representative of the distributions within the sample. In order to pick up the extremely short T_2's in the rock core, values of the pulse sequence were pushed to the hardware limits. A 90μs RF pulse was obtained at max power with 500 echoes covering the short T_2 decay with an echo time of 140μs.

The ZTE imaging sequence [18-20] is depicted and discussed in Figure 32. Its value comes from capturing fast relaxing decays, short T_2 values. Since there is a trade-off between bandwidth and missing k-space points, where a bandwidth greater than the optimum leads to poor image quality, it was found that any more than 2 missing k-space points leads to poor image quality and thus a maximum bandwidth of 200kHz was used. A tip angle of 6.4^o at maximum power yields a pulse time of 6.4μs. A TR of 3.84ms was used and is greater than the needed TR, calculated from the Ernst angle equation, thus giving adequate time for the longitudinal magnetization to recover. A FOV of 60mm x 90mm x 60mm with 64^3 pixels is adequate to image the rock core without creating any wrap-around artifacts. The suggested resolution of 0.938mm/pixel x 1.41mm/pixel x 0.938mm/pixel is inaccurate because the maximum bandwidth used is much less than the required bandwidth to achieve this resolution. Through the use of multiple phantoms of varying size it was estimated that the minimum resolution that can be resolved is about 3mm/pixel. The total scan time was approximately 58 seconds providing quick snapshots of the real time process.

Results and Discussion

AFLAS and FEP Sleeves

In preliminary experimental runs, two different confining sleeves were used and tested. The sleeve needed to seal against the rock core forcing flow to go through the rock core and not around, it needed to be inert against the supercritical CO_2, and it needed to have minimal or no signal contribution. During testing several significant differences

between the AFLAS and FEP sleeves were noticed. The first significant difference is displayed in Figure 54.

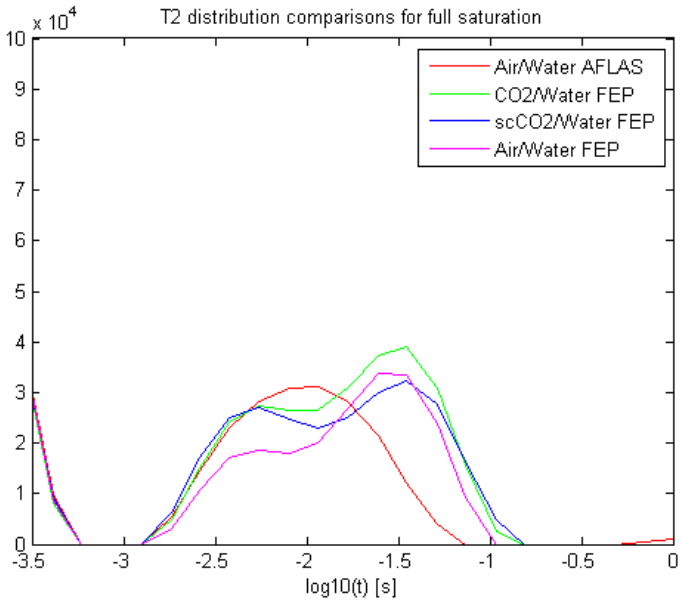


Figure 54: T2 distribution comparisons between AFLAS and FEP

Figure 54 displays the T_2 distributions for four different runs during full saturation, three of which are a Teflon wrapped core in a FEP heat shrink sleeve and one of which an AFLAS sleeve is used. Although the distributions cover about the same range of values, it is noticed that the AFLAS run has distinctly one smooth population whereas the FEP runs have what appears to be two populations. Because the FEP sleeves have no signal and the AFLAS sleeves do, verified through imaging of just the sleeves, it make sense that the signal from the AFLAS sleeve would contribute to the overall T_2 distribution therefore altering it from the FEP data, which is believed to be the signal from just the water in the core due to the fact that there is no signal from the FEP. In conjunction with the hypothesis that the AFLAS sleeve also may have significant surface

relaxation effects on the water, it makes sense that the use of the AFLAS sleeve alters the actual T_2 distribution and is therefore not representative of the sample itself.

Another downfall of the AFLAS sleeve is its reaction to the carbonic acid created as a results of introducing CO_2 to water during the drainage phase. This can be seen in Figure 55 where the AFLAS sleeve signal contribution becomes more intense as time goes on. This increase in the NMR signal indicates an increase in the molecular mobility of the sleeve which may be due to a solubilization of the material from its reaction to the created carbonic acid.

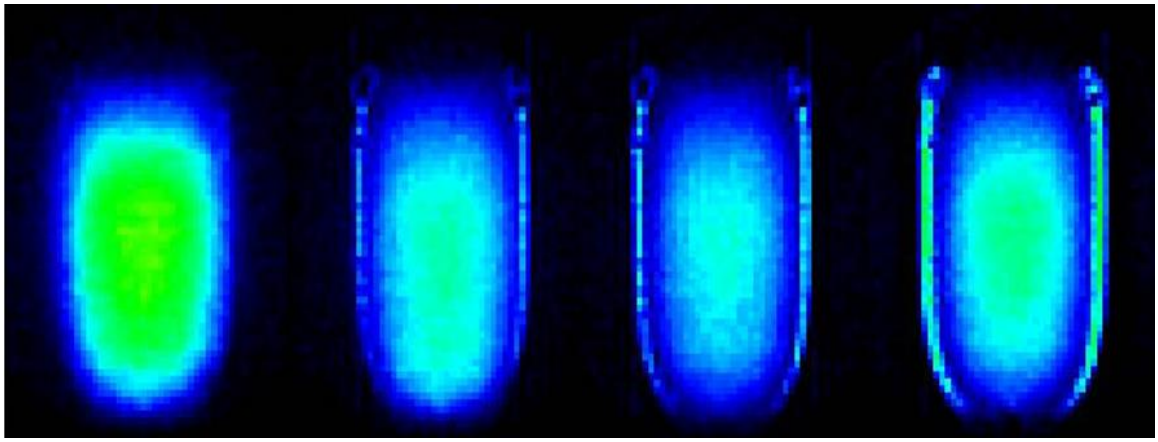


Figure 55: ZTE images of AFLAS time evolution reaction to CO_2

Figure 56 shows two pictures of the aftermath of the sleeve reaction. The choice to go with a Teflon wrapped core and an FEP sleeve was made because of the significant signal contribution from the AFLAS and its severe reaction to the introduction of CO_2. The FEP sleeve is ideal because it doesn't react with the CO_2, it has no signal contribution, and when the core is wrapped with Teflon the flow will be restricted from going around the core.



Figure 56: AFLAS sleeve failure

ZTE Data

Drainage and imbibition experiments were performed under conditions representing a CO2 sequestration scenario with a specific interest into the residually trapped amount of NW fluid due to capillary forces. The capillary trapping efficiency was investigated for three different NW fluids (air, CO2, and scCO2) using two different Berea Sandstone rock cores. The wetting fluid being DI H20. Three dimensional images were taken via the ZTE pulse sequence and the data was analyzed in Prospa. At the beginning of each experiment a ZTE image was taken of the dry rock core to provide a background image of the signal that could then be subtracted from the saturated images, via matrix operations within Prospa, providing only signal from the water within the pores.

A ZTE image was taken at full saturation, several during the drainage process, and one more at the end of the imbibition process. The three most important images, for calculating the fraction of residually trapped NW fluid and capillary trapping efficiency,

are the full saturation image, the last drainage image, and the final imbibition image. The 3D ZTE images were broke down into a 1D average profile across the length of the core, the z-direction. This was done by selecting the center, sagittal 2D plane of the rock core and averaging each line in the transverse plane making a 1D sagittal profile. These profiles are depicted in Figure 57Figure 58Figure 59 for air, CO2, and scCO2 as the NW phase. These figures represent the most recent experiments on rock core #3 (as a note, the experiments refer to rock core #2 and #3 and not #1 because #1 was used to work out the bugs). The other 9 profiles for the other experiments were left out due to their similarities to these three and are thus represented in the data tables and attached in the appendices.

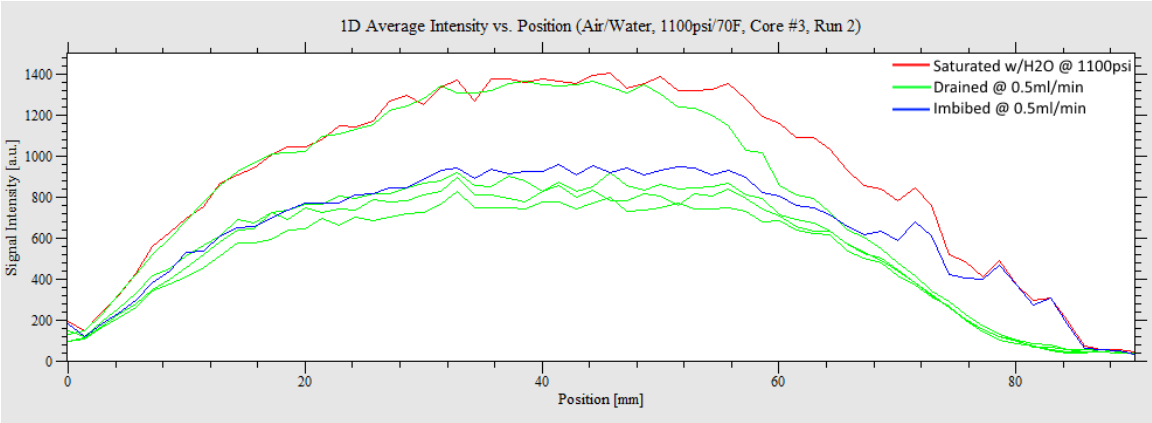


Figure 57: 1D profiles indicating W phase along rock core length (air/H_2O)

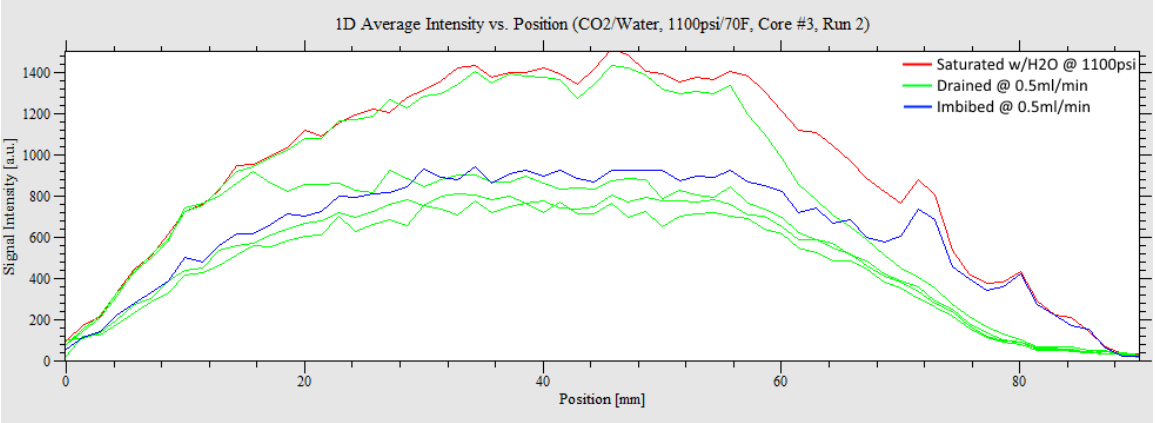


Figure 58: 1D profiles indicating W phase along rock core length (CO_2/ H_2O)

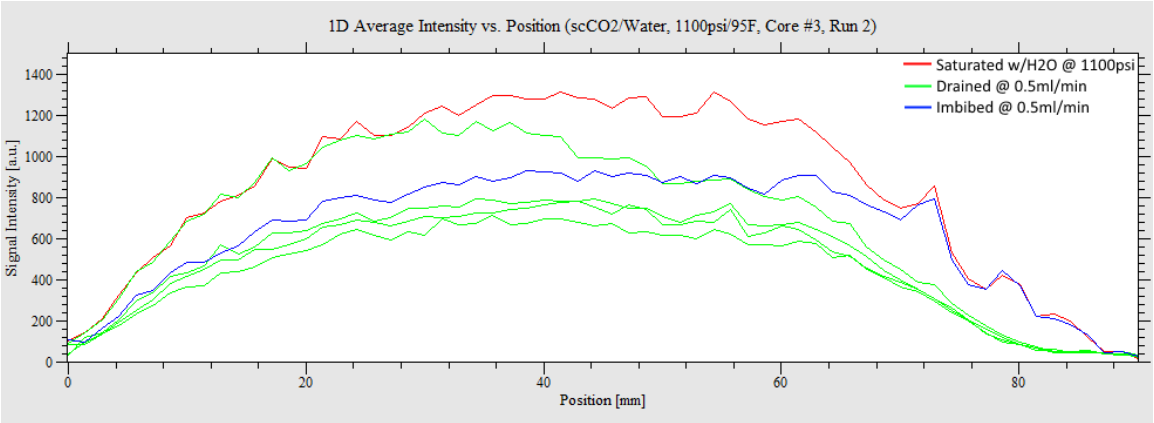


Figure 59: 1D profiles indicating W phase along rock core length ($scCO_2$/ H_2O)

The red line indicates maximum saturation, the green lines indicate the saturation during drainage in chronological steps as signal decreases, and the blue line indicates the maximum saturation reached after imbibition. All lines represent the signal associated with the wetting phase saturation, so in order to obtain the NW phase saturation fraction the data is normalized and the difference from maximum saturation, being 1, is thus the fraction of NW phase within the pores. This is, assuming that all the pores are initially full of the wetting phase.

Examining each of the 1D profiles for air, CO2, and scCO2 is it clear to see that they have very similar profiles and intensities. In-flow artifacts appear in the 3D ZTE images and are pronounced in the 1D profiles as signal spikes in the intensity, the several signal spikes are on the right side around 72-80 mm. RF roll-off occurs at both the left and right ends of the FOV and thus the signal intensity decreases. Due to these artifacts, the NW phase fractions are calculated based on the average signal intensity in the most linear region of the profiles, that being from 28-54mm.

The NW phase fraction data for each 1D profile of every experiment is depicted in Table 3and Table 4. The data represents the fraction of NW phase within the pores. The key NW phase fractions are those highlighted in yellow. There are several noticeable trends. The first is that both CO2 and scCO2 tend to drain the core more than air in the same period of time, indicated in the drainage-4 line in Table 3 and Table 4. For core #2, CO2 drains the core, on average, about 9.5% more than air, and scCO2 drains the core about 7.5% more than air. For core #3, CO2 drains the core, on average, about 5.5% more than air, and scCO2 drains the core about 6.5% more than air. After imbibition, CO2 is noticed to have the largest amount of trapped NW phase when compared to air and scCO2, indicated in the imbibition final line in Table 3 and Table 4. On average, about 6.5% more CO2 is trapped than air and about 8.0% more CO2 is trapped than scCO2 for core #2. For core #3, on average, about 3.0% more CO2 is trapped than air and about 5.0% more CO2 is trapped than scCO2.

Table 3: Non-wetting phase fraction in Berea rock core #2

Scan (Non-Wetting Phase)	**Normalized Average 1D Intensity from 28-54mm**					
Run (Sleeve Material)	Air (AFLAS)	Air (FEP)	CO2 (FEP)	CO2 (FEP)	scCO2 (FEP)	scCO2 (FEP)
Fully Saturated	0	0	0	0	0	0
Drainage-1	0.00	0.01	0.02	0.02	0.40	0.30
Drainage-2	0.30	0.22	0.36	0.43	0.44	0.40
Drainage-3	0.35	-----	0.47	0.48	0.49	0.43
Drainage-4 ($S_{Initial}$)	0.41	0.42	0.51	0.51	0.51	0.47
Imbibition Final ($S_{Residual}$)	0.28	0.32	0.36	0.37	0.27	0.30
Trapping Efficiency ($S_{Residual}/S_{Initial}$)	0.68	0.76	0.71	0.73	0.53	0.64

Table 4: Non-wetting phase fraction in Berea rock core #3

Scan (Non-Wetting Phase)	**Normalized Average 1D Intensity from 28-54mm**					
Run (Sleeve Material)	Air (FEP)	Air (FEP)	CO2 (FEP)	CO2 (FEP)	scCO2 (FEP)	scCO2 (FEP)
Fully Saturated	0	0	0	0	0	0
Drainage-1	0.10	0.03	0.01	0.04	0.19	0.18
Drainage-2	0.35	0.36	0.34	0.39	0.42	0.40
Drainage-3	0.38	0.40	0.41	0.44	0.44	0.42
Drainage-4 ($S_{Initial}$)	0.40	0.44	0.47	0.48	0.49	0.48
Imbibition Final ($S_{Residual}$)	0.30	0.32	0.33	0.35	0.29	0.29
Trapping Efficiency ($S_{Residual}/S_{Initial}$)	0.75	0.73	0.70	0.73	0.59	0.60

The last noticeable trend appears in the trapping efficiency. The trapping efficiency is just the ratio of the residually trapped amount of NW phase to the maximum amount of NW phase that was in the core after drainage. For core #2, the average

trapping efficiency for air and CO2 are the same whereas scCO2 differs from air by about 13.5% and from CO2 by about 13.5%. For core #3, the average trapping efficiency for air and CO2 only differ by about 2.5% where as scCO2 differs from air by about 14.5% and from CO2 by about 12.0%. This is a significant amount of variation of the trapping efficiency of scCO2 from both air and CO2. The scCO2 trapping efficiency is found to be about 10% less than values reported on in [6] for similar sandstones of Bentheimer and Doddington. However the trapping efficiency for air and CO2 are on par with their reported results. This is more suggestive of results obtained in [8, 9] where scCO2 has a lower residual saturation than for an analogue strongly water-wet system, air and water. Furthermore, as the contact angle increases, snap-off is less favored and gives way to a more piston-like advance. With the suppression of snap-off there is decrease in residual saturation [8, 9, 28]. Therefore, this suggests that scCO2/water is not strongly water-wet leading to larger contact angles, a decrease in snap-off, and therefore a lower residual saturation.

It appears that CO2 and air have very similar trapping efficiencies but differ in both the amount of NW phase drained and the residual amount of NW phase trapped. ScCO2 has similarities to air in the amount of residual NW phase trapped and similarities to CO2 in the maximum amount of NW phase drained but it has significant differences in the trapping efficiency when compared to both air and CO2. From this three trends are observed. The first is that CO_2 and $scCO_2$ drain the core to a higher maximum value than does air. The second is that CO_2 traps the largest residual amount of NW phase when compared to air and $scCO_2$. Finally, air and CO_2 have similar trapping efficiencies

whereas $scCO_2$ is on the order of 12% less than both air and CO_2. It is key to point out that these three trends hold true and are similar for both rock cores. This can be more clearly seen and summarized when averaging all four runs for each NW phase (air, CO2, and scCO2). The data is depicted in Table 5.

Table 5: Average NW phase fractions of all four runs of air, CO_2, and $scCO_2$

Scan (Non-Wetting Phase)	**Average values for all 4 runs of air, CO2, and scCO2 with standard deviation**		
Run	Air	CO2	scCO2
Drainage-4 ($S_{Initial}$)	0.42±0.02	0.49±0.02	0.49±0.02
Imbibition Final ($S_{Residual}$)	0.31±0.02	0.35±0.02	0.29±0.01
$S_{Residual}/S_{Initial}$	0.73±0.04	0.72±0.02	0.59±0.05

By plotting the NW phase initial vs. the NW phase residual we can better visualize the efficiency differences and other trends. Figure 60 displays the NW phase residual saturation vs. the NW phase initial saturation for the values from Table 3Table 4. A point closer to the diagonal would mean a higher trapping efficiency. Therefore, a point on the diagonal would represent a 100% efficiency and all of the NW phase pumped in would have remained trapped in the rock core. We can see from the graph that both air and CO_2 seem to follow a linear trend where an increase in the initial NW phase leads to a higher residual NW phase, seen also in the work of [29]. The difference in saturation values between the air and CO_2, where CO_2 has a higher initial and residual NW phase saturation, can be explained by the difference in surface tension. CO_2 has a surface tension with water that is slightly more than half as much as that between air and

water. A lower surface tension will lead to lower overall capillary entrance pressures within the pores of the rock. With a lower capillary entrance pressure than that for the air/water system but with the same flow rate, the viscous forces will therefore be stronger in comparison to the capillary forces. Thus, CO_2 will invade more pores leading to a higher initial NW phase saturation.

$ScCO_2$ does not fall on this same linear line that air and CO_2 seem to fall on. It is farther away from the diagonal than air and CO_2, thus having a lower trapping efficiency. It does fall on the same initial NW phase interval as CO_2, due to the similar surface tension values, but with a lower residual NW phase. This lower residual NW phase saturation can be explained by the hypothesized increase in the contact angle leading to less favorable snap-off conditions and thus a lower residual NW phase saturation, as previously mentioned. Furthermore, by fitting a line through the air and CO_2 data and forcing it to go through zero, in order for the trend in saturation to have basis in reality, one would obtain a slope of the linear fit that is near exactly the average trapping efficiency value in Table 5. The same holds true if a linear trend is fit through the $scCO_2$ data. This further validates the linear trend in the trapping efficiency and more clearly distinguishes the difference of $scCO_2$ from that of air and CO_2.

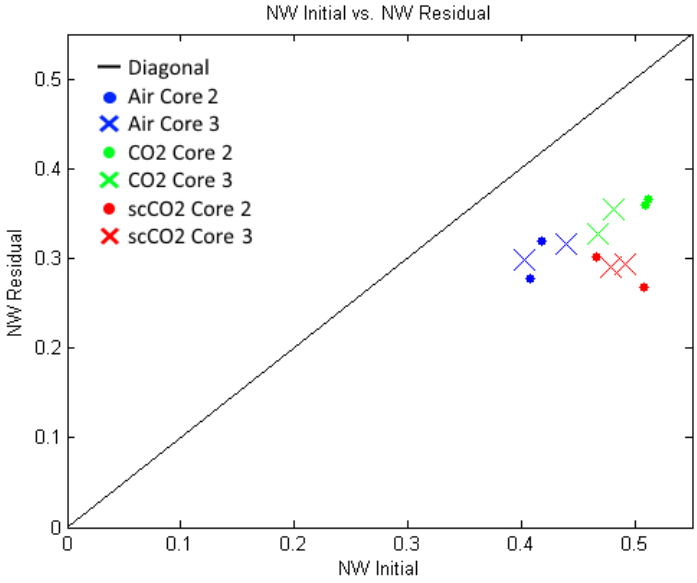


Figure 60: NW phase initial vs. NW phase residual

T2 Distribution Data

The transverse relaxation times where obtained using the CPMG pulse sequence. This yielded a multi-exponential decay curve which was inverse Laplace transformed using MATLAB in order to obtain a distribution of T_2 values. The T_2 distributions were obtained at the same significant stages as the ZTE images. The T_2 values are associated with different pore sizes within the rock core [30]. The increased interactions of nuclei in small pores as well as surface relaxation effects contribute to the decrease of T_2 as pore sizes become smaller. Therefore, larger T_2 values (slower relaxation) are attributed to larger pores and smaller T_2 values (faster relaxation) are attributed to smaller pores. This is illustrated in Figure 61 where there are essentially two distributions that can be split into smaller and larger pores.

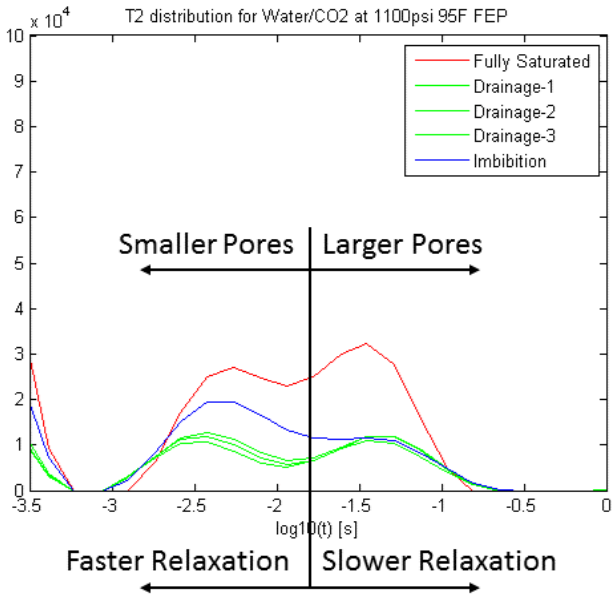


Figure 61: Illustration for defining larger and smaller pores associated with transverse relaxation times

In all T_2 distributions there appear to be two main distributions which we associate to larger and smaller pore sizes [10, 31, 32]. The third distribution on the far left continues off to infinity. It cannot be resolved because the pulse time and echo time could not be shortened any further due to hardware limitations, therefore missing most of the extremely fast relaxing signal. These extremely fast relaxing spins are associated with micro-porosity clay-bound water [10, 31]. Because this water is immobile and of minimal contribution to the overall signal, it is ignored when discussing the drainage and imbibition within the pore structure.

Figure 62, Figure 63, and Figure 64 depict the T_2 distributions during full saturation, drainage, and imbibition of air, CO2, and scCO2 as the NW phase with the wetting phase being DI H2O doped with Magnevist. These figures are the results from the three most recent experiments of air, CO2, and scCO2 on rock core #3. They are

representative of the rest of the T_2 distributions and have a similar trend which is why the others have been left out. They can be found in the attached appendices for reference.

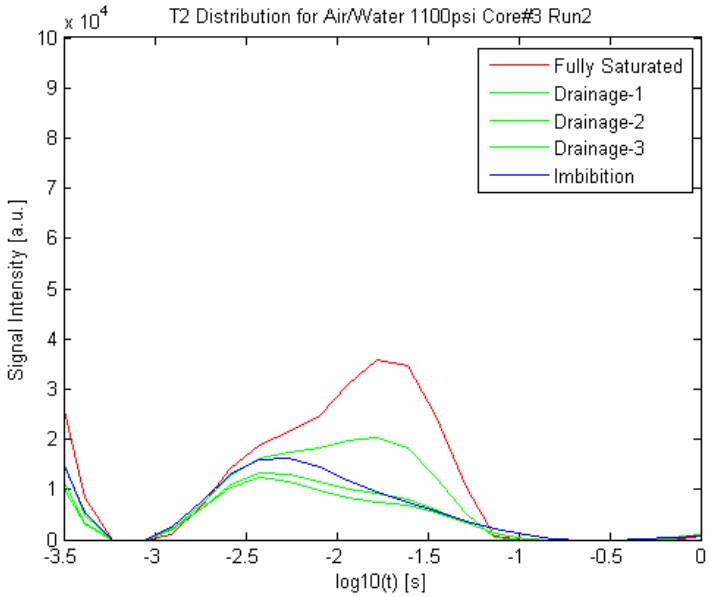


Figure 62: T_2 distribution evolution for drainage/imbibition of air/water at 75.86bar and ambient temperature

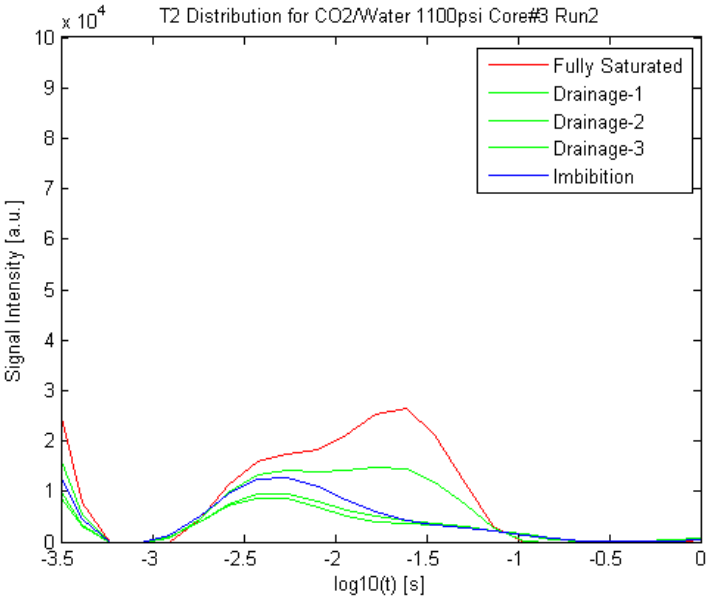


Figure 63: T_2 distribution evolution for drainage/imbibition of CO_2/water at 75.86bar and ambient temperature

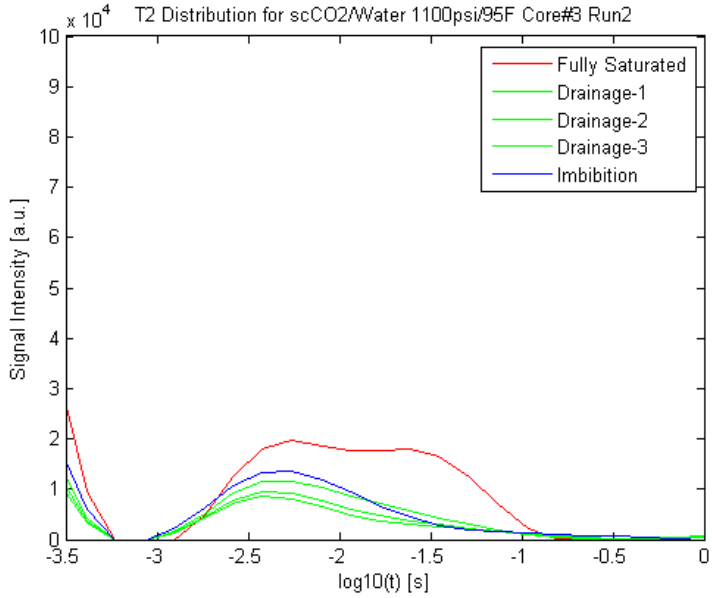


Figure 64: T_2 distribution evolution for drainage/imbibition of $scCO_2$/water at 75.86bar and 35ºC

All distributions exhibit the same trends. They have values between about 10^{-3} and 10^{-1}s with intensities that are relatively similar. There appear to be two populations that are centered on about $10^{-2.3}$ and $10^{-1.6}$s. The left population is associated with the micro-porosity and the right population is associated with the macro-porosity. The key thing to take from these distributions is that during imbibition it appears only the micro-porosity is filling with water where the macro-porosity remains the same. This is seen in the fact that there is no change from the final drainage line (green) to the imbibition line (blue) within the macro-porosity whereas there is an increase in saturation in the micro-porosity. It can therefore be deduced that the NW phase is preferentially trapped in the larger pores due to the lack of signal in the macro-porosity during imbibition. This could be due to the fact that the pore-throat aspect ratio, the ratio of the pore body radius to the

throat radius, is greater in the macro-porosity giving rise to more favorable snap-off conditions [7, 8, 33, 34].

5mm Core T2 Distribution Data

In order to fully resolve the extremely fast relaxing spins and add more validity to the macro and micro-porosity regions of the T_2 distributions, a saturated 5mm core was placed in a 5mm probe where shorter pulse times could be achieved and the signal from the short T_2's could be captured. To capture this, a 10μs RF pulse was used with 6000 echoes and an echo time of 16μs.

Figure 65 shows the fully resolved T_2 distribution in red compared to the T_2 distributions captured in the SWB probe where the very fast relaxing spins cannot be captured. As expected, the distribution was fully resolved and three populations are present. In [31] they discuss three different regions in the porous sandstone structure that can be associated with different relaxation times. The first is micro-porosity clay-bound water. It is associated with the far left population because the immobility and very small pore sizes result in the smallest T_2 values. The second is called the meso-porosity capillary-bound water. It is discussed as the micro-porosity in the above content because the clay-bound water is not expected to move and therefor the distribution is assumed not to change. This is associated with the middle population because the pore size is slightly greater and surface relaxation effects aren't as strong. The third is called the macro-porosity free water. It is associated with the right most population because the pore size is yet larger and surface relaxation effects are yet less strong.

As expected the left population that goes off to infinity in the SWB T_2 distribution is resolved into a single population. Because this population is associated with the clay-bound water it is expected to be immobile and the population is not expected to change during drainage and imbibition. Therefore, it further justifies the assumption in the previous material where the far left population that can't be resolved, can thus be ignored as it does not contribute to the desired data and the right two populations are indeed associated with the smaller pore, capillary-bound water and the larger pore, freer water. As a drainage/imbibition experiment cannot be performed on the 5mm core this assumption and justification is the best that can be accomplished.

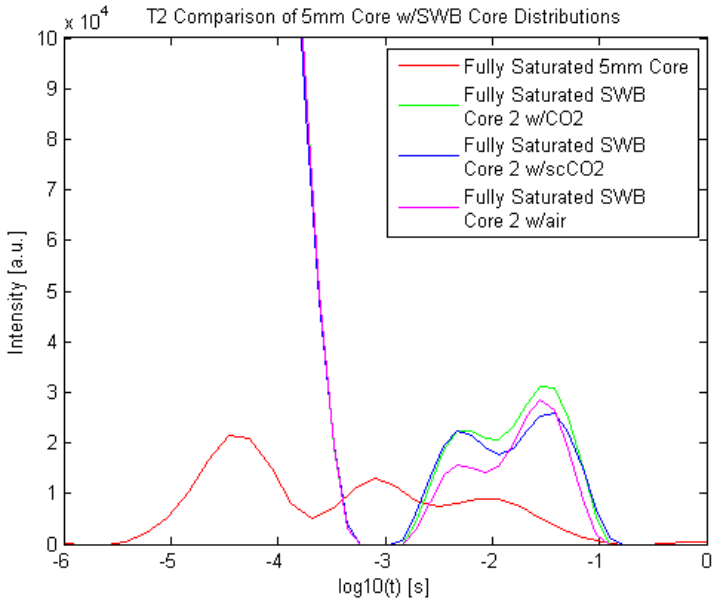


Figure 65: T2 distribution comparison of 5mm and 27mm cores

The fact that the 5mm core populations do not line up with the SWB populations can be attributed to the ILT. Because a smaller core was used in a smaller probe where different pulse times used and a more complete data set was acquired the ILT data will be

different. It is expected that if the SWB data could be fully captured and resolved that it would shift left and resemble the fully resolved 5mm core distribution data.

Conclusions and Future Work

This work demonstrates the usefulness of NMR in determining the residually trapped NW phase as well as providing insight into the pores in which the NW phase is preferentially trapped. The results provide for a comparison between the different NW phases used as well as characterizing the capillary trapping of each NW phase. Several trends are apparent when comparing each NW phase:

1. scCO2 and CO2 drain the core to a higher NW phase fraction than air
2. CO2 traps the largest residual amount of NW phase
3. scCO2 traps the lowest residual amount of NW phase and has a trapping efficiency about 13% less than CO2 and air, further justified by Figure 60
4. air and CO_2 seem to follow a linear trend where an increase in the initial NW phase leads to an increase in the residual NW phase where they hover around a trapping efficiency of about 72%

Because scCO2 has a lower residual NW phase saturation than air and CO2, it can be concluded that scCO2/water is not as strongly water-wet. This means scCO2/water have larger contact angles which lead to a suppression of snap-off and therefore a lower residual NW phase saturation [8, 9, 28]. This data suggests that air is not a good proxy for scCO2 and that CO2, when in its supercritical state, behaves differently and leads to a reduction in capillary trapping.

Lastly, the T_2 distribution data shows that the NW phase, regardless of whether its air, CO2, or scCO2, is preferentially trapped in the larger pores. This result is supported by the findings of [33, 34]. This is most likely due to the fact that snap-off conditions are more favorable in the macro-porosity. Meaning, the aspect ratio is greater and a piston-like flow does not occur.

Future Work

This work has proved the usefulness of NMR in characterizing the trapping of fluids in porous media. There is a multitude of things that can be pursued to advance this work. There are some planned future experiments in which low field NMR spectroscopy is utilized. In a low field spectrometer the image resolution may be lower, however susceptibility impacts on T_2 relaxation will be minimized and therefore all water in the sample will be able to be analyzed with the T_2 method, and all experiments will be able to be carried out on a wider variety of geological materials. This work presents a preliminary example of how NMR might inform us about the location of the imbibed or trapped fluid.

Another thing that may prove useful to pursue is to use different flow rates, Ca numbers, and study how the trapping efficiency varies as well as the location of the trapped fluid. This would provide insight into the optimum situations for maximizing the amount of trapped fluid. It would be expected that, to a point, the trapping efficiency would increase with lower Ca numbers and subsequently, decrease with higher Ca numbers. Hypothesized from the role between viscous and capillary forces where an

increase in the flow rate would increase the viscous forces and subsequently, overcome the capillary forces that trap the NW fluid.

Another insightful study would be to test fluids with lower and higher surface tension values to see if, as hypothesized between air and CO_2, they would fall on higher and lower NW phase initial saturations where the efficiency value could give one an idea of the contact angle by comparison. As discussed, a lower surface tension will lead to lower overall capillary entrance pressures within the pores of the rock. Thus, the viscous forces will therefore be stronger in comparison to the capillary forces for a given flow rate, and the NW fluid will invade more pores leading to a higher initial NW phase saturation. Again, this knowledge would prove beneficial in optimizing the amount of NW fluid to be trapped.

Furthermore, this research could be applied to different porous media to study the best geologic scenarios for sequestering CO_2. It would also provide further insight into how and where the NW fluid is trapped and to any limits and idealities of trapping. This work could further be extended to enhanced oil recovery (EOR) to study and optimize the process.

7. TWO PHASE FLOW EXPERIMENT

Introduction

Two-phase flow in porous media is an important part of many industries and science, such as enhanced oil recovery, fluidized beds, and water-cooled nuclear reactors to name a few. However, because two phase flow can be unpredictable, there is a lot that isn't understood. Therefore, understanding the fluid behavior and mechanics of immiscible two phase flow could prove valuable to providing more efficient designs and to ensure the system behaves and reacts as expected. Thus, being able to determine the flow structure and understanding the fluid mechanisms from a relationship between the capillary number and the pressure gradient could prove valuable.

Previous numerical simulations and calculations by Sinha, [35], have studied the nonlinearity of the pressure gradient versus capillary number in an immiscible two-phase flow through a porous media. They demonstrate that in the region where the capillary forces are comparable to the viscous forces, the fluids behave similar to a Bingham fluid. That being, there is effectively a yield threshold to overcome before the fluids begin to displace. This is essentially the threshold pressure that must be overcome. Furthermore, they developed a generalized Darcy equation that described this relationship where the equation was given by $(\Delta P - \Delta P_c) \sim Ca^{\beta}$, where ΔP is the pressure difference across the porous media, ΔP_c is the threshold pressure previously mentioned, Ca is the capillary number, and β is the scaling factor. They found that $\beta = ½$ for low capillary numbers and $\beta = 1$ for high capillary numbers.

Previous research in this NMR lab by Rassi et al [36], has confirmed these values, when the threshold pressure is factored in, and have illustrated the nonlinear and linear regimes. However, further experimental investigation has indicated there is an instability in the flow structure occurring around the transition region, the region where β changes from 0.5 to 1. This instability is not understood and is thought to be attributed to one of the flow regimes indicated in the following figure.

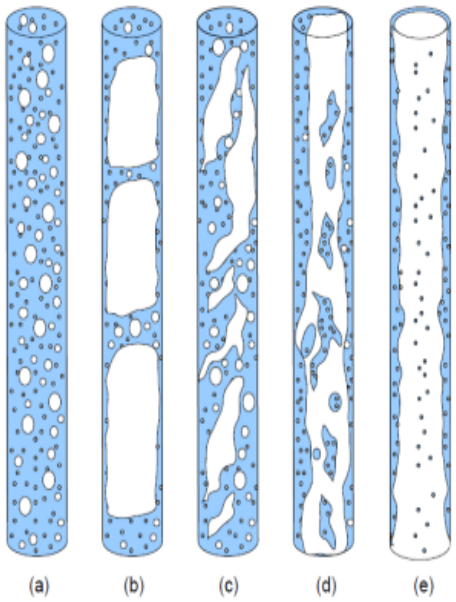


Figure 66: Immiscible two phase flow regimes: (a) Bubbly (b) Slug (c) Froth (d) Annular (e) Dispersed [4]

The use of NMR techniques would help provide insight into this instability. NMR would be used to monitor the signal from the water in a mixed, immiscible two-phase flow that was being pumped through a borosilicate microsphere bead pack at different capillary numbers. The occurrence of this instability has led to the idea that different flow

[4] http://modelica.github.io/Modelica/om/Modelica.Fluid.Dissipation.PressureLoss.StraightPipe.dp_twoPhaseOverall_DP.html

regimes could correspond to different capillary number/pressure drop relationships and have an effect on the exponent value β. The NMR data would provide a visualization and quantitative data to help qualify different flow patterns and would be used to help characterize these flow patterns and their relationship to capillary number, pressure drop, and β value. The following work presented was a collaboration of efforts from several students within the MRM lab at Montana State University; Matt Dancyk, Andrew Bender, Kevin Izard, and Linn Thrane.

Experimental Setup and Procedure

Setup

The previous experiments that were conducted, where the NMR spectrometer wasn't used, were nearly the same as the experiments conducted in this thesis where the only difference was the length of line between the two pressure transducer ends. This was because more tubing was needed to hook the bead pack up inside the magnet. This would yield an overall higher pressure difference but the same trends should follow.

The setup is depicted in Figure 67 where the wetting and non-wetting fluids are mixed and pumped through the bead pack in the NMR spectrometer and out into a beaker at atmospheric conditions. The check valves are in place to ensure that one fluid does not enter the other fluid's line. The filter helped mix the two fluids and also keep any small particles from entering the bead pack and blocking flow. The flow rate of each fluid was controlled by an ISCO 500D syringe pump. The pressure difference was measured by a single differential Omega pressure transducer with a 0-1.03 bar (0-15 psi) range hooked to a DAQ where data was controlled by a LabVIEW program. All NMR experiments

were performed using a Bruker AVANCE 300MHz spectrometer with a 20 mm diameter Wide Bore (WB) probe.

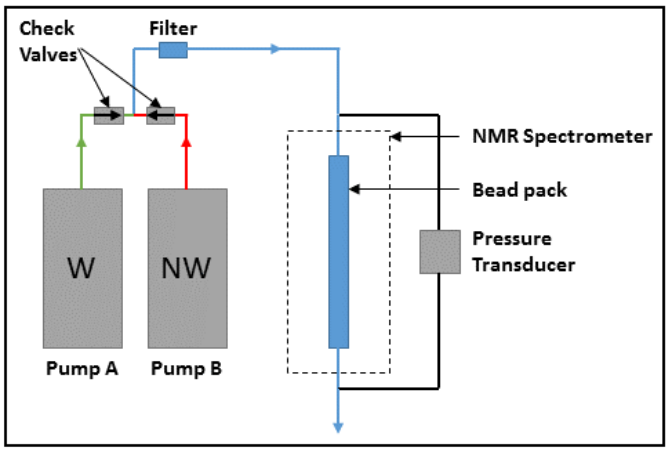


Figure 67: Two phase flow setup diagram

Procedure

The procedure is quite simple. One pump was filled with the wetting fluid (water) and the other pump was filled with the nonwetting fluid (air). A flow rate was set on each pump and allowed to run until both pumps were empty. While the pumps were running the pressure transducer would acquire the differential pressure drop and the NMR spectrometer would utilize pulse sequences to obtain data. The flow rate could be changed in order to obtain different Ca numbers that would correspond to the nonlinear or linear regions, $\beta = 0.5$ or 1 (the focus of this thesis is around the transition region, where β changes from 0.5 to 1, and in the nonlinear region).

Pulse Sequences

The NMR spectrometer utilized the single pulse and 1D imaging sequences discussed in the pulse sequences section of the viscous fingering experiments chapter but

with some modifications. The single pulse free induction decay (FID) is the most basic pulse sequence used to simply detect signal. A single NMR radio frequency, RF, pulse excites the protons in the liquid H_2O in the sample and the free induction decay (FID) that is acquired immediately afterwards can be directly correlated to the total water content within the sample. A 0.1 ms RF pulse with a power level of 15.2 dB was used to achieve a 90^o RF pulse with a bandwidth of 12800 Hz. 1024 points of the FID were obtained. It was set up so that 35 sequential scans would be obtained with a 10 second delay between each, yielding a total acquisition time of about 5.8 minutes. This resulted in a matrix of data that was 1024 x 35 where there was 35 sequential FIDs.

The MSME sequence is depicted in Figure 42. For this sequence however, the phase gradients were eliminated and no echo train was used therefore becoming a 1D imaging sequence thus yielding a single 1D profile selected along the z-axis, the longitudinal length of the bead pack. A BP32 pulse with a 0.1 ms pulse length at 15.2 dB was used to achieve a 90^o excitation pulse with a bandwidth of 12800 Hz. The 180^o refocusing pulse thus excited a bandwidth of 8000 Hz at 9.2 dB. The 1D profile was obtained from a 30 mm length along the z-axis averaged over a 50 mm wide slice with 128 matrix points along the length of the acquired profile. A repetition time of 3 seconds was used in order to allow the magnetization to return to equilibrium. It was set up such that 100 sequential scans would be obtained with a 10 second delay between each, yielding a total acquisition time of about 16.7 minutes. This resulted in a matrix of data that was 128 x 100 where there was 100 sequential 1D profiles.

Results and Discussion

Figure 68 displays the obtained pressure drop curve for a given flow rate. The steady state (SS) region depicted is the section is where the pressure drop was averaged and a single value was obtained. The threshold pressure was determined to be the value the pressure curve returned to in the long time regime. The pressure drop was subtracted from the threshold pressure, as in the equation discussed in the introduction, and plotted on a log scale for a given flow rate. This data is displayed in Figure 69.

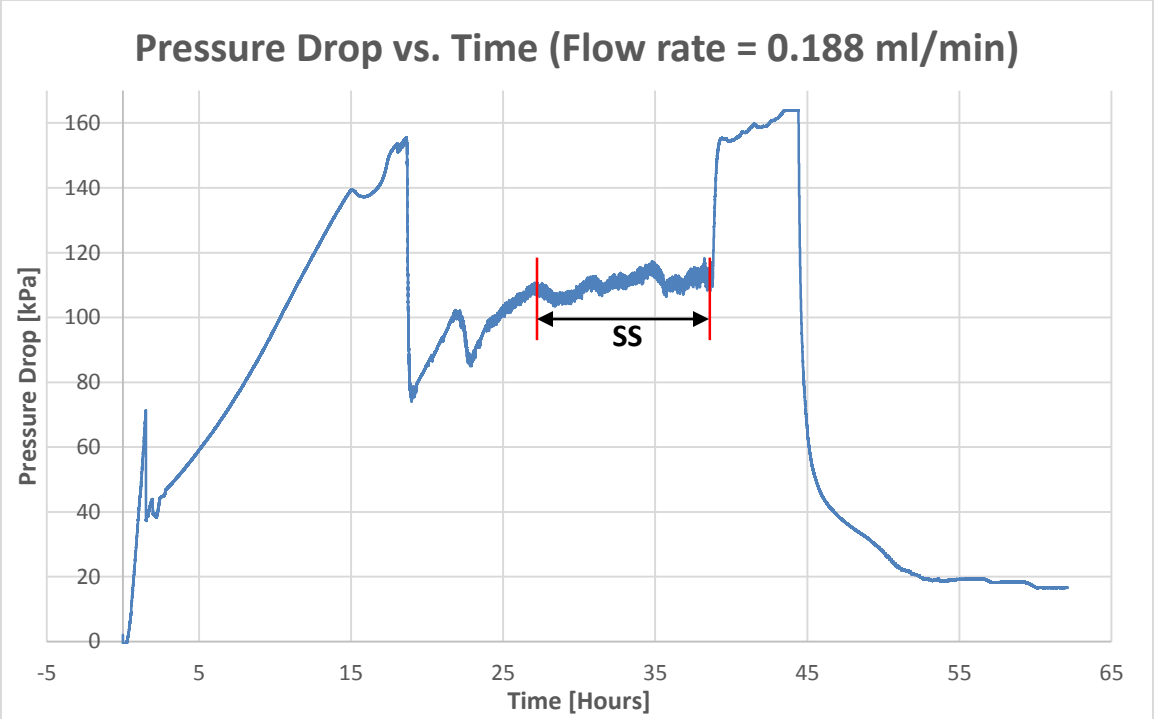


Figure 68: Example of pressure drop acquisition and steady state (SS) region[5]

Figure 69 displays the earliest data acquired with the threshold pressure for a range of Ca numbers over the two different regimes. Each dot represents an immiscible

[5] Courtesy of Andrew Bender

two phase flow experiment from which a pressure gradient was obtained for a given flow rate. Each regime was then fitted with a curve where β is represented by the slope of the curve, since it's on a log plot. It is clear there are two distinct regions and a transition zone. The upper blue region represents the linear region where β = 1.0192, almost 1, and the lower red region represents the nonlinear region where β = 0.5829, close to 0.5. The discrepancy of the nonlinear region to having a β value of 0.5 could be attributed to the volatile transition region. Multiple experiments were done in the lowest Ca numbers and at the transition region. As displayed, the lowest Ca number experiments nearly have overlaid values as opposed to the transition region in which there is significant variance in the pressure value. This data is supportive of that in [35].

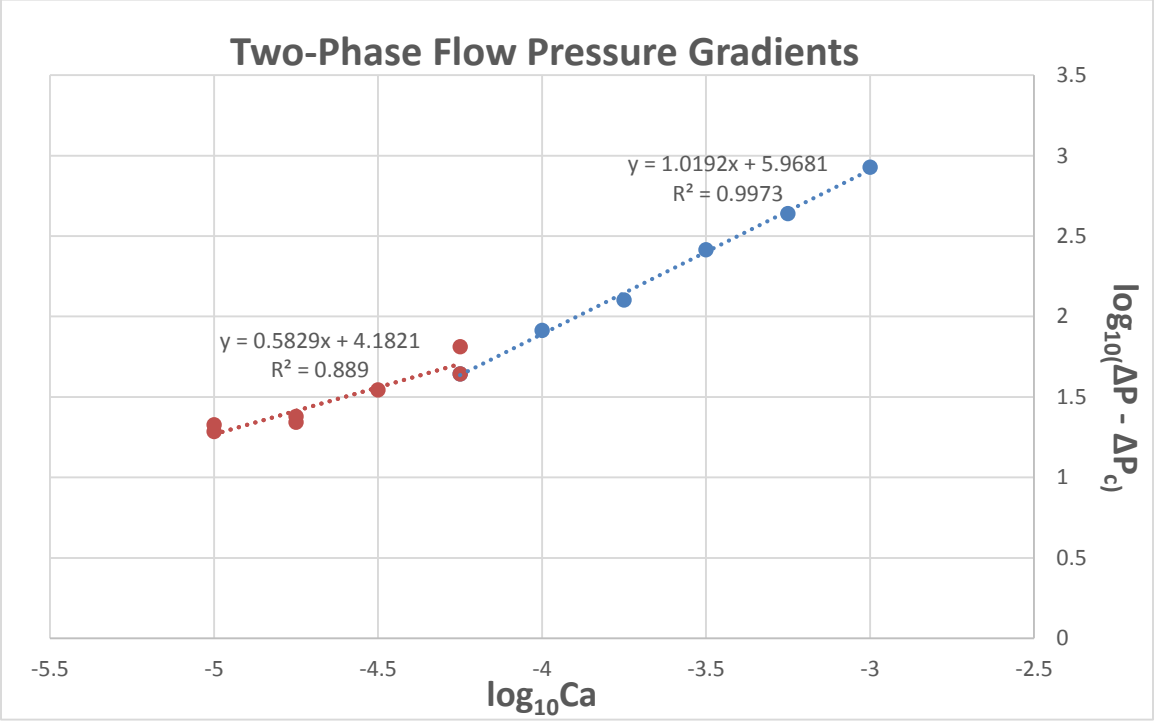


Figure 69: Capillary number vs. pressure gradient (preliminary)[6]

[6] Courtesy of Andrew Bender

Further experiments were conducted to further establish the nonlinear β value and to further understand the effects of the transition region. Figure 70 displays several data sets over the course of several months. The purple data is the same data as the red in the previous graph but with the transition region removed. As seen the β value changes significantly, from β = 0.5829 in the previous one to β = 0.4364, thus showing the dynamics of the flow in the transition region can have a large effect on the data and that this region needs to be further studied.

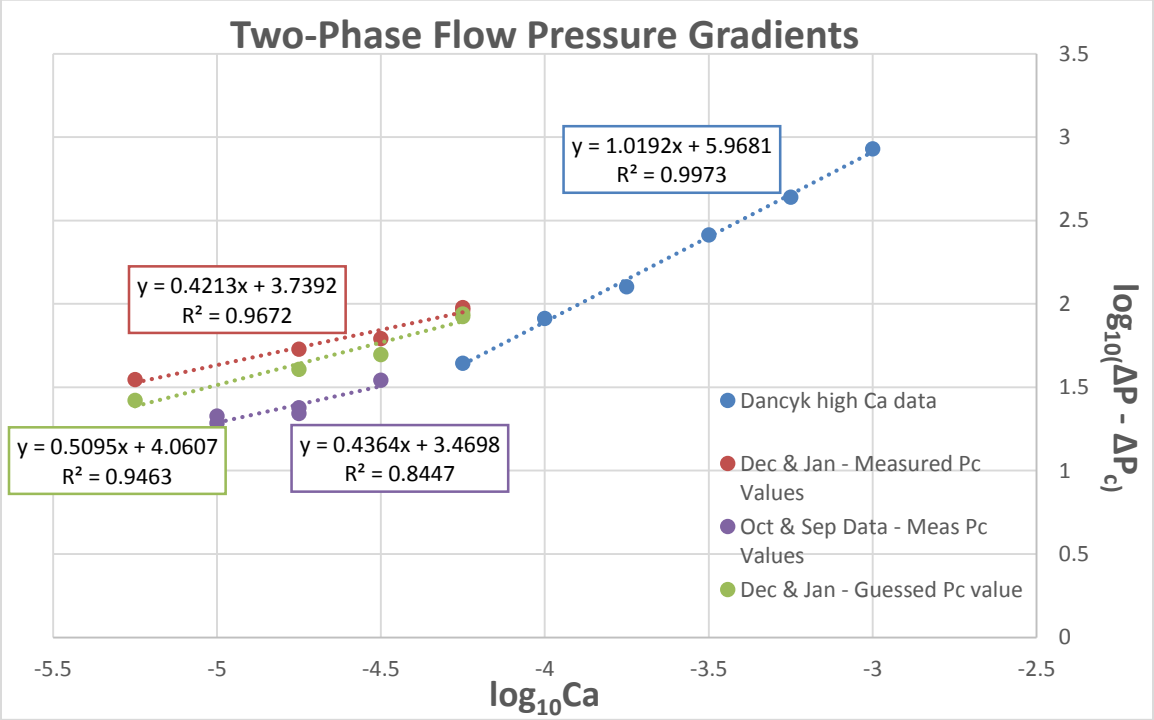


Figure 70: Capillary number vs. pressure gradient (recent)[7]

The red and the green lines display the most recent data obtained. The red line displays data for which the threshold pressure, P_c, was measured from the experiment and

[7] Courtesy of Andrew Bender

the green line displays the same data but for which the threshold pressure was adjusted in order to obtain a β value close to 0.5. This in conjunction with the NMR data later discussed suggests that the threshold pressure that is being obtained is not representative of the steady state two phase flow region. Also, this data has shifted upwards resulting in higher overall pressure gradients. This is possibly attributed to the changing structure of the bead pack over the course of months as it is moved around in conjunction with, possibly, small clogs due to particles or crushed beads. These hypotheses and phenomena need further exploring.

NMR Data

The following four figures show the pressure curve overlaid with the obtained NMR data, either the FID data or the 1D imaging data, for a given flow rate. The FID data is representative of the overall amount of H_2O in the system, so a higher signal intensity corresponds to a larger amount of H_2O in the system. This is not true for the 1D imaging data as the signal is affected by the velocity where a faster velocity actually diminishes the signal because some of the spins don't see their refocusing pulse because they have moved out of the voxel in which it was excited and signal is therefore diminished. The 1D imaging data gives access to any local changes across the bead pack, i.e., as to such things as whether or not the saturation is uniform or if there is local minimums and maximums.

Figure 71 and Figure 72 represent the FID and 1D imaging data obtained for the flow rate of 0.595 ml/min ($\log_{10}Ca = -4.5$), which is near the transition region. The FID data in Figure 71 is displayed in blue where each of the 25 chunks represent the average

signal for 35 sequential FIDs taken over approximately 5.8 minutes. The gaps in between are the time frame in which the 1D imaging data was obtained.

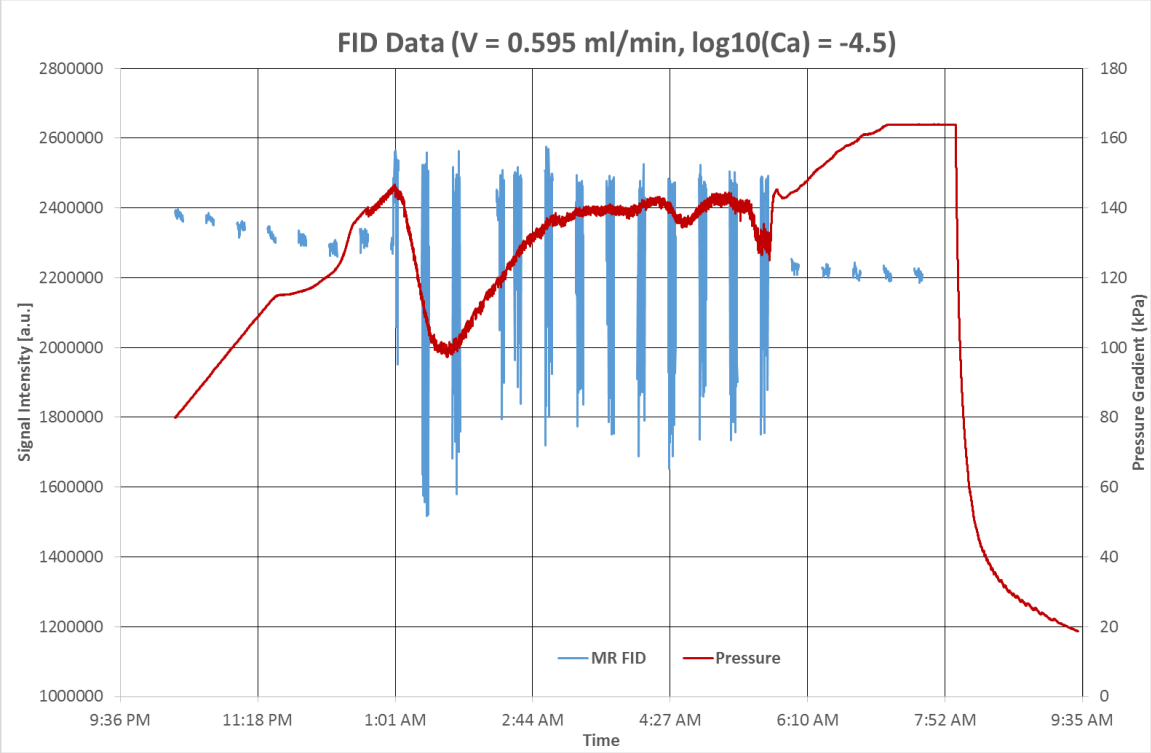


Figure 71: FID data (pressure overlaid) for V = 0.595 ml/min[8]

The 1D imaging data for this flow rate is represented in Figure 72. The data is displayed in blue where each of the 25 chunks represent the average signal from 100 sequential 1D profiles each 10 seconds apart taken over approximately 16.7 minutes. The gaps in between are the time frame in which the FID data was obtained.

[8] Courtesy of Linn Thrane and Andrew Bender

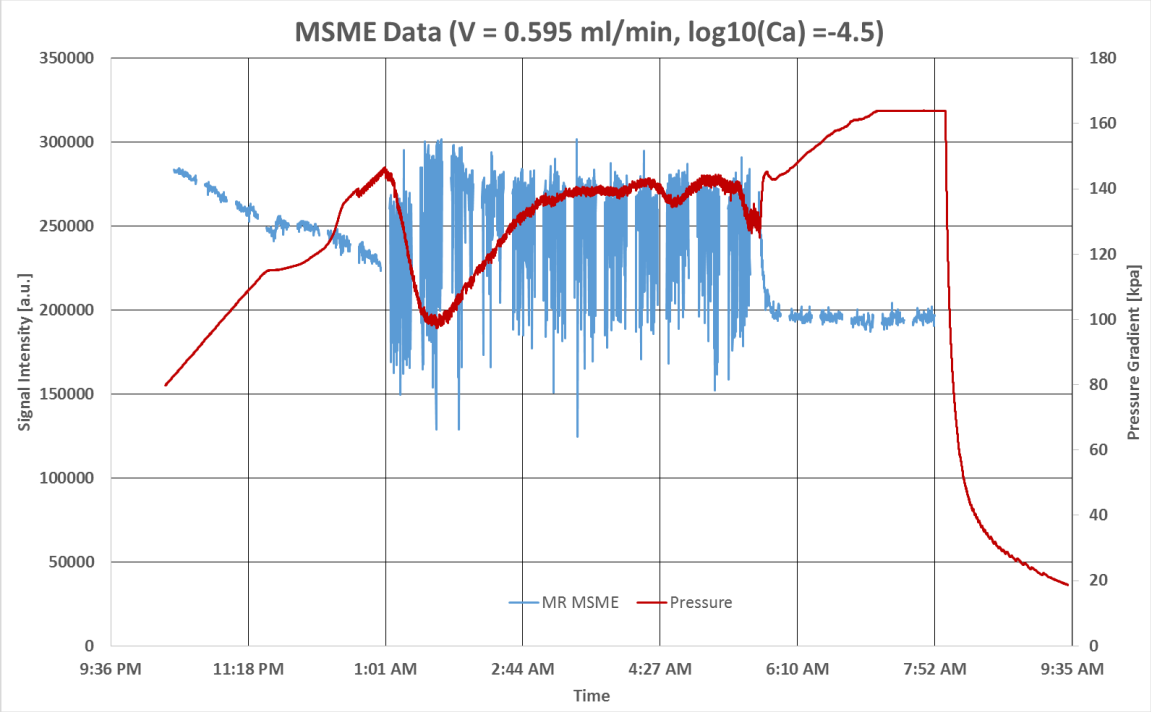


Figure 72: MSME data (pressure overlaid) for V = 0.595 ml/min[9]

Observing Figure 71, during the first section in which the pressure continues to rise the water saturation remains fairly constant, denoted by the very small fluctuations of the MR data keeping a nearly constant signal intensity. This indicates that no air has entered the bead pack. This makes sense as the air is compressible and requires significant time in order for the pressure to build up, under a constant flow rate, to overcome the system pressure head and begin to flow and compete with the incompressible water which easily overcomes the system pressure head.

The point at which the pressure begins to drop is the point at which air is introduced into the bead pack, denoted by the large fluctuations of the MR signal. It may not appear so on the graph but if one zoomed in on one chunk of the NMR signal it is

[9] Courtesy of Linn Thrane and Andrew Bender

actually fluctuating between low and high signal intensity values. When air goes through the bead pack, the overall NMR signal goes down because the signal is only sensitive to the hydrogen ion in water and the amount of water in the bead pack has decreased due to the introduction of air.

The pressure then increases and begins to stabilize in the steady state region. The NMR signal also begins to stabilize and seems to fluctuate consistently. This signifies that air and water are alternately flowing through the bead pack in a constant manner. The minimum and maximum fluctuations appear to be on the same order meaning that the same amount of air and water are alternately flowing through the bead pack. These oscillations could mean possibly a slug or froth type flow through the bead pack. Further experiments would need to be conducted to verify this hypothesis.

Lastly, the pressure begins to increase again and the signal intensity has very small fluctuations around a near constant value. This again indicates that there is no air flowing through the bead pack. This is probably due to the fact that during pressurization in the beginning the higher pressure water (higher pressure because the incompressible nature of the water allows the pressure to increase more quickly at a constant flow rate as opposed to compressible air) entered the lower pressure air pump reservoir and this is the point at which all the air has been pumped through the system leaving only the remaining water.

The pumps are then shut off and as shown the pressure drops to a constant threshold pressure. This last segment of data provides insight into previous experiments and to possibly why the β value is slightly off from the anticipated value of 0.5. In [35],

their results show that the threshold pressure depends on the NW saturation in the bead pack. Therefore, the threshold pressure obtained may not be representative of the steady state regime because the introduction of pure water and the pressure increase at the last segment would likely change the NW saturation.

Experiments are currently being conducted in which the pumps are stopped during the steady state regime to avoid the surge of pure water and allow the system to come to equilibrium at a threshold pressure that would be consistent with the two phase flow steady state regime. This would verify whether or not there is a significant change is the threshold pressure that would alter the data.

Lastly, the 1D imaging data in Figure 72 shows similar trends to those discussed about the FID data. The difference being that the signal intensity of the 1D imaging data is not indicative of the total water saturation within the bead pack for the reason previously discussed. It can be seen that as the pressure drop increases (meaning that there also must be an increase in velocity) the signal intensity decreases. As previously mentioned the 1D imaging data allowed access to a 1D profile where the intensity corresponds to the amount of water at a location along the length of the bead pack. This is used to determine whether or not there are any local variations in the saturation. When analyzing the profiles, the saturation was seen to be fairly uniform across the bead pack. That is why an average intensity of the 1D profile was used to create the NMR data in Figure 72 and Figure 74.

Figure 73 and Figure 74 display the same NMR and pressure data as in Figure 71 and Figure 72 expect for with a flow rate of 0.188 ml/min ($\log_{10}Ca = -5$). Figure 73

displays the FID data in 38 chunks where each chunk consists of the 35 average signals of FID scans each 10 seconds apart for a total scan time of about 5.8 minutes. The data in Figure 74 displays the 1D imaging data where each of the 39 chunks represent the average signal from 100 sequential 1D profiles each 10 seconds apart taken over approximately 16.7 minutes. It should be noted that the experiment was cut short which is why the data stops in the steady state region and there is no recorded data for the return to the threshold pressure. However, from previous experiments it is expected to follow the same trend as is Figure 71 and Figure 72.

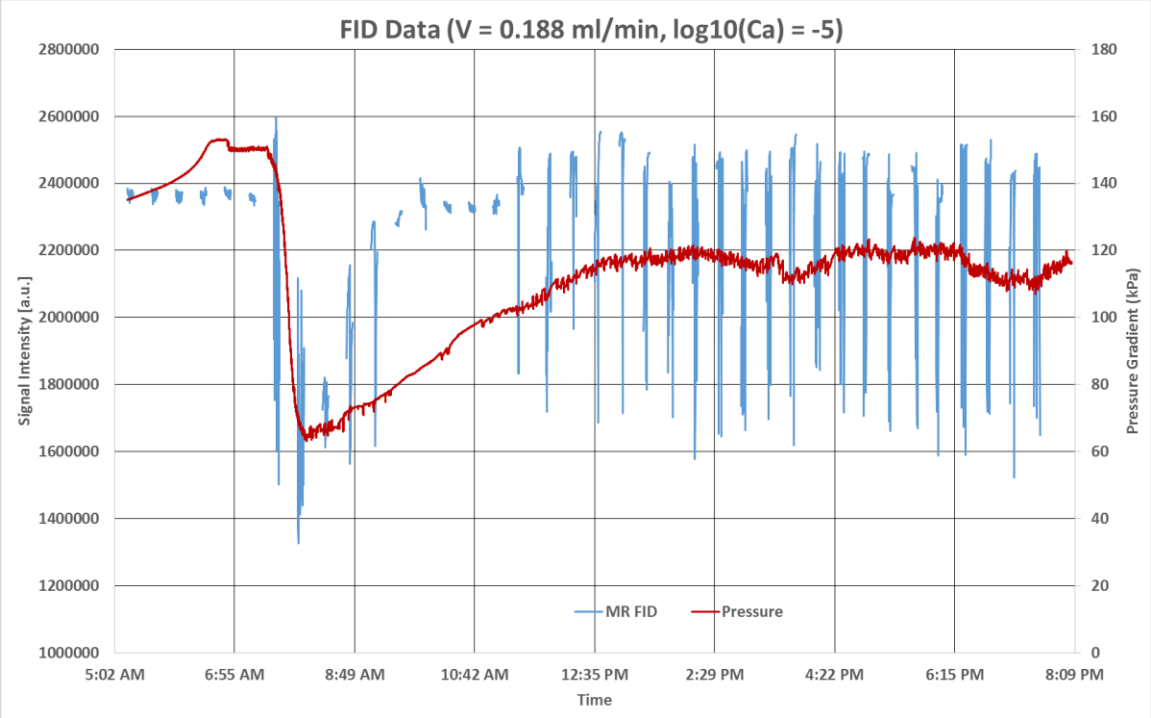


Figure 73: FID data (pressure overlaid) for V = 0.188 ml/min[10]

[10] Courtesy of Linn Thrane and Andrew Bender

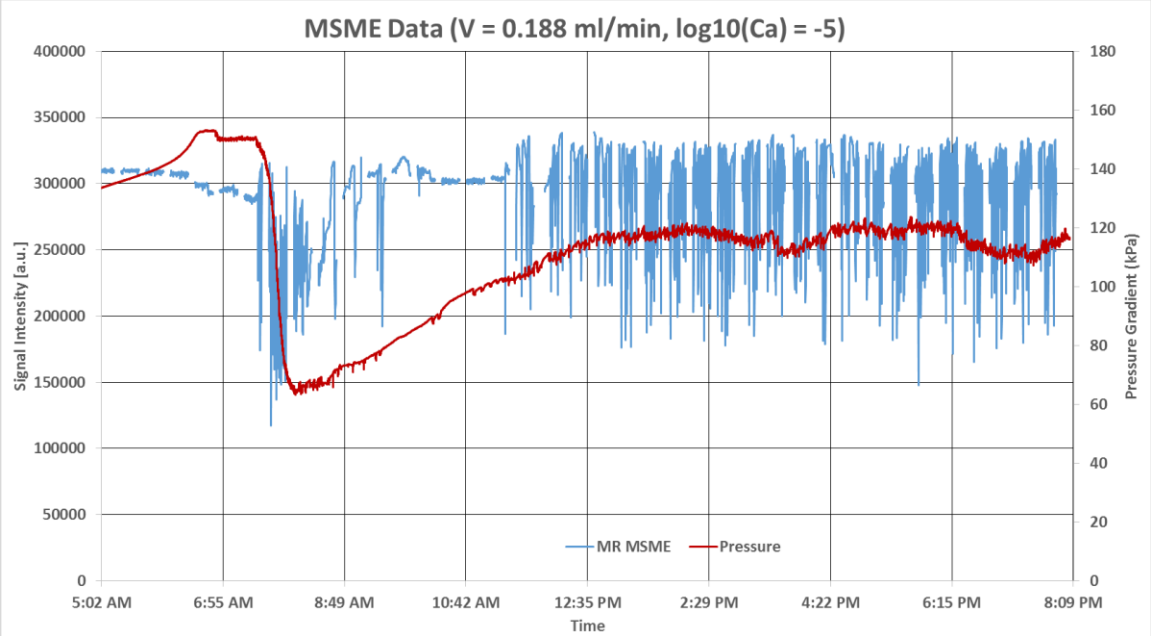


Figure 74: MSME data (pressure overlaid) for V = 0.188 ml/min)[11]

The data trends for the lowest flow rate match closely with the highest flow rate. There is an initial pressure spike until air is introduced into the bead pack at which point the pressure drops. Then the pressure increases while the air and water flow sporadically through the bead pack creating sporadic highs and lows in the signal intensity. Finally, the pressure stabilizes and the air and water fluctuate consistently between a high and low signal intensity.

When comparing the FID data from the two different flow rates, focusing on the steady state region, it appears that the faster flow rate, 0.595 ml/min, fluctuates around a slightly higher signal intensity than the slower flow rate, around about 2200000 as opposed to about 2100000. Also, it appears that both flow rates fluctuate around the same maximum signal intensity, about 2500000. This suggests the same water saturation

[11] Courtesy of Linn Thrane and Andrew Bender

maximum is being reach as the two phase flow is being pumped through the bead pack. However, the flow rates seem to fluctuate at different minimum signal intensities. The slower flow rate fluctuating around about 1700000 and the faster flow rate fluctuating around about 1800000. This means that the slower flow rate has larger overall saturation fluctuations and suggests that the slower flow rate drains the bead back to a lower saturation than the faster flow rate. The 1D imaging data also confirms these same larger fluctuations in the slower flow rate.

Conclusions and Future Work

In conclusion, NMR has proved its usefulness in elucidating saturation fluctuations and trends in two phase flow through a bead pack, and it shows great potential in determining different flow patterns, different trends at different Ca numbers, and its ability to provide further understanding of the transition region. The data shows that both flow rates exhibit very similar overall trends in both the pressure profile and in the saturation fluctuations. More importantly the steady state region exhibits consistent fluctuations in the saturation leading to the conclusion that there is a slug or possibly froth type flow pattern through the bead pack. Further experimentation needs to be done to validate and elucidate this hypothesis.

Future Work

As mentioned, further work needs to be done in order to validate the slug/froth type flow pattern that was hypothesized. This could be done by running experiments on a faster time scale, developing a method to acquire a quick 2D image, or possibly some

propagator or velocimetry imaging. This may lead to a better understanding of different flow patterns that may be present at different Ca numbers as well as elucidate the dynamics at the transition region.

As previously discussed, the threshold pressure obtained may not be representative of the steady state regime because the introduction of pure water and the pressure increase at the last segment would likely change the NW saturation. Therefore, experiments are currently being conducted in which the pumps are stopped during the steady state regime to avoid the surge of pure water and allow the system to come to equilibrium at a threshold pressure that would be consistent with the two phase flow steady state regime. This would verify whether or not there is a significant change is the threshold pressure that would alter the data.

Another experiment to be conducted is to run the same experiments but at a Ca number that is on the transition region. This data could be compared to the existing data at lower Ca number and possibly significant differences could lead to a better understanding of the dynamics surrounding the transition region. Furthermore, an experiment could be conducted on the steady state region but on a faster timescale, no 10 second delays but back to back scans, that would provide for higher resolution in the time domain. This would lead to a further understanding of the saturation fluctuations that are occurring and possibly elucidate any differences or trends at various Ca numbers.

REFERENCES CITED

1. Bachu, S., *CO(2) storage in geological media: Role, means, status and barriers to deployment.* Progress in Energy and Combustion Science, 2008. **34**(2): p. 254-273.

2. Klusman, R.W., *Evaluation of leakage potential from a carbon dioxide EOR/sequestration project.* Energy Conversion and Management, 2003. **44**(12): p. 1921-1940.

3. Carles, P., *A brief review of the thermophysical properties of supercritical fluids.* Journal of Supercritical Fluids, 2010. **53**(1-3): p. 2-11.

4. Rassi, E.M., S.L. Codd, and J.D. Seymour, *MR measurement of critical phase transition dynamics and supercritical fluid dynamics in capillary and porous media flow.* Journal of Magnetic Resonance, 2012. **214**: p. 309-314.

5. Benson, S.M. and D.R. Cole, *CO(2) Sequestration in Deep Sedimentary Formations.* Elements, 2008. **4**(5): p. 325-331.

6. Andrew, M., B. Bijeljic, and M.J. Blunt, *Pore-scale imaging of trapped supercritical carbon dioxide in sandstones and carbonates.* International Journal of Greenhouse Gas Control, 2014. **22**: p. 1-14.

7. Herring, A.L., et al., *Effect of fluid topology on residual nonwetting phase trapping: Implications for geologic CO2 sequestration.* Advances in Water Resources, 2013. **62**: p. 47-58.

8. Iglauer, S., et al., *Residual CO2 imaged with X-ray micro-tomography.* Geophysical Research Letters, 2011. **38**.

9. Pentland, C.H., et al., *Measurements of the capillary trapping of super-critical carbon dioxide in Berea sandstone.* Geophysical Research Letters, 2011. **38**.

10. Tanino, Y. and M.J. Blunt, *Capillary trapping in sandstones and carbonates: Dependence on pore structure.* Water Resources Research, 2012. **48**.

11. Wildenschild, D., et al., *Exploring capillary trapping efficiency as a function of interfacial tension, viscosity, and flow rate.* 10th International Conference on Greenhouse Gas Control Technologies, 2011. **4**: p. 4945-4952.

12. Neufeld, J.A., et al., *Convective dissolution of carbon dioxide in saline aquifers.* Geophysical Research Letters, 2010. **37**.

13. Deng, W., M.B. Cardenas, and P.C. Bennett, *Extended Roof snap-off for a continuous nonwetting fluid and an example case for supercritical CO2.* Advances in Water Resources, 2014. **64**: p. 34-46.

14. Roof, J.G., *Snap-Off of Oil Droplets in Water-Wet Pores.* Society of Petroleum Engineers Journal, 1970. **10**(1): p. 85-&.

15. Rossen, W.R., *Snap-off in constricted tubes and porous media.* Colloids and Surfaces a-Physicochemical and Engineering Aspects, 2000. **166**(1-3): p. 101-107.

16. Callaghan, P.T., *Translational dynamics and magnetic resonance : principles of pulsed gradient spin echo NMR*2011, Oxford ; New York: Oxford University Press. xvii, 547 p.

17. Roffmann, W.U., et al., *Small birdcage resonators for high-field NMR microscopy.* Journal of Magnetic Resonance Series B, 1996. **111**(2): p. 174-177.

18. Weiger, M., K.P. Pruessmann, and F. Hennel, *MRI with Zero Echo Time: Hard versus Sweep Pulse Excitation.* Magnetic Resonance in Medicine, 2011. **66**(2): p. 379-389.

19. Weiger, M., et al., *High-resolution ZTE imaging of human teeth.* Nmr in Biomedicine, 2012. **25**(10): p. 1144-1151.

20. Garwood, M., *MRI of fast-relaxing spins.* Journal of Magnetic Resonance, 2013. **229**: p. 49-54.

21. Hurlimann, M.D., et al., *Diffusion-relaxation distribution functions of sedimentary rocks in different saturation states.* Magnetic Resonance Imaging, 2003. **21**(3-4): p. 305-310.

22. Krynicki, K., *Proton Spin-Lattice Relaxation in Pure Water between Zero Degrees C and 100 Degrees C.* Physica, 1966. **32**(1): p. 167-&.

23. Smith, D.W.G. and J.G. Powles, *Proton Spin-Lattice Relaxation in Liquid Water and Liquid Ammonia.* Molecular Physics, 1966. **10**(5): p. 451-&.

24. Easteal, A.J. and L.A. Woolf, *Pressure and Temperature-Dependence of Tracer Diffusion-Coefficients of Methanol, Ethanol, Acetonitrile, and Formamide in Water.* Journal of Physical Chemistry, 1985. **89**(7): p. 1066-1069.

25. Jonas, J., T. Defried, and D.J. Wilbur, *Molecular Motions in Compressed Liquid Water.* Journal of Chemical Physics, 1976. **65**(2): p. 582-588.

26. Duan, Z.H. and R. Sun, *An improved model calculating CO2 solubility in pure water and aqueous NaCl solutions from 273 to 533 K and from 0 to 2000 bar.* Chemical Geology, 2003. **193**(3-4): p. 257-271.

27. Suekane, T., et al., *Application of MRI in the Measurement of Two-Phase Flow of Supercritical CO2 and Water in Porous Rocks.* Journal of Porous Media, 2009. **12**(2): p. 143-154.

28. Blunt, M.J. and H. Scher, *Pore-Level Modeling of Wetting.* Physical Review E, 1995. **52**(6): p. 6387-6403.

29. Zuo, L. and S.M. Benson, *Process-dependent residual trapping of CO2 in sandstone.* Geophysical Research Letters, 2014. **41**(8): p. 2820-2826.

30. Washburn, K.E. and P.T. Callaghan, *Tracking pore to pore exchange using relaxation exchange spectroscopy.* Physical Review Letters, 2006. **97**(17).

31. Jorand, R., et al., *Study of the variation of thermal conductivity with water saturation using nuclear magnetic resonance.* Journal of Geophysical Research-Solid Earth, 2011. **116**.

32. Liaw, H.K., et al., *Characterization of fluid distributions in porous media by NMR techniques.* Aiche Journal, 1996. **42**(2): p. 538-546.

33. Al-Raoush, R.I. and C.S. Willson, *A pore-scale investigation of a multiphase porous media system.* Journal of Contaminant Hydrology, 2005. **77**(1-2): p. 67-89.

34. Wardlaw, N.C. and Y. Li, *Fluid Topology, Pore-Size and Aspect Ratio during Imbibition.* Transport in Porous Media, 1988. **3**(1): p. 17-34.

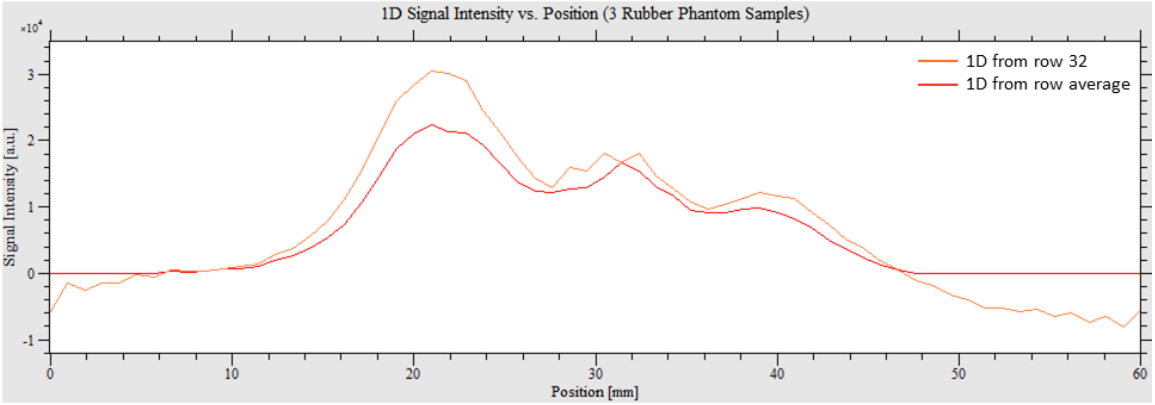
35. Sinha, S. and A. Hansen, *Effective rheology of immiscible two-phase flow in porous media.* Epl, 2012. **99**(4).

36. Rassi, E.M., S.L. Codd, and J.D. Seymour, *Nuclear magnetic resonance characterization of the stationary dynamics of partially saturated media during steady-state infiltration flow.* New Journal of Physics, 2011. **13**.

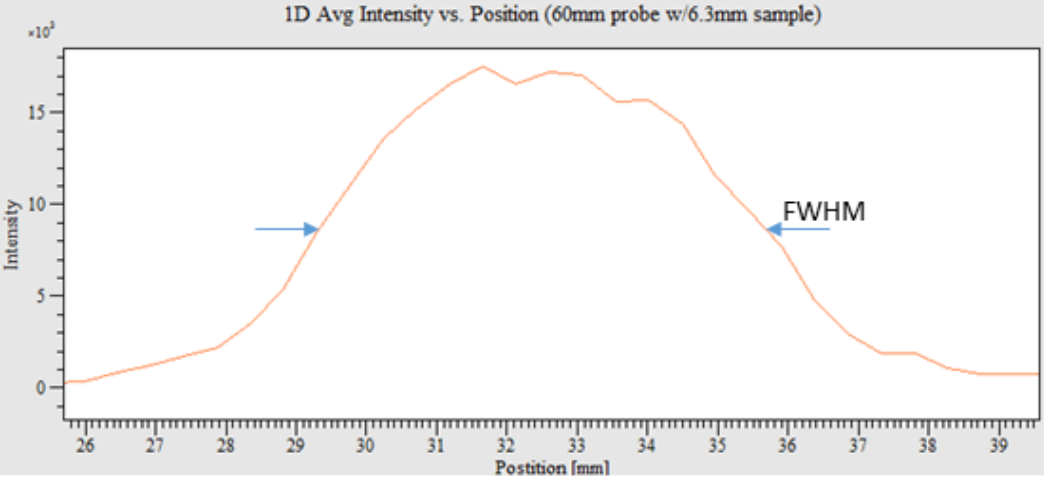
APPENDICES

APPENDIX A

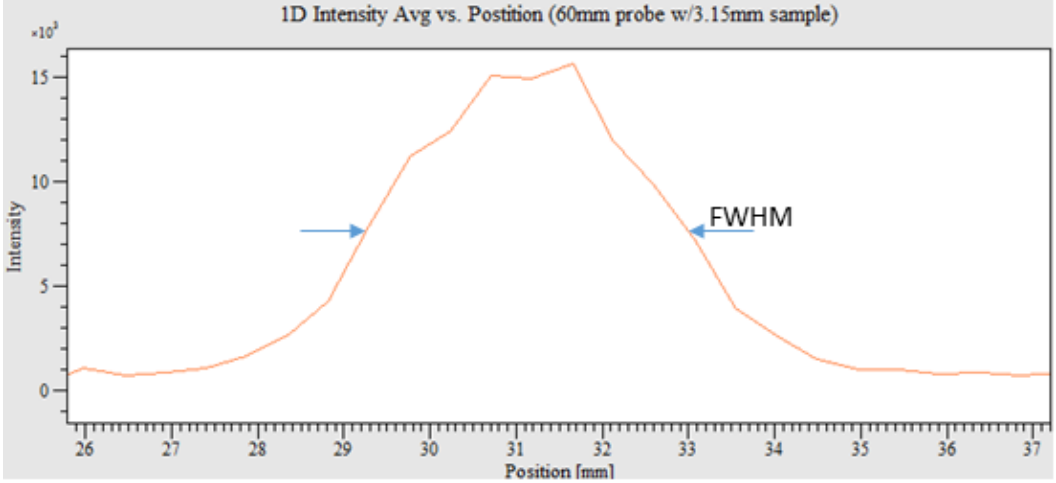
ZTE OPTIMIZATION DATA



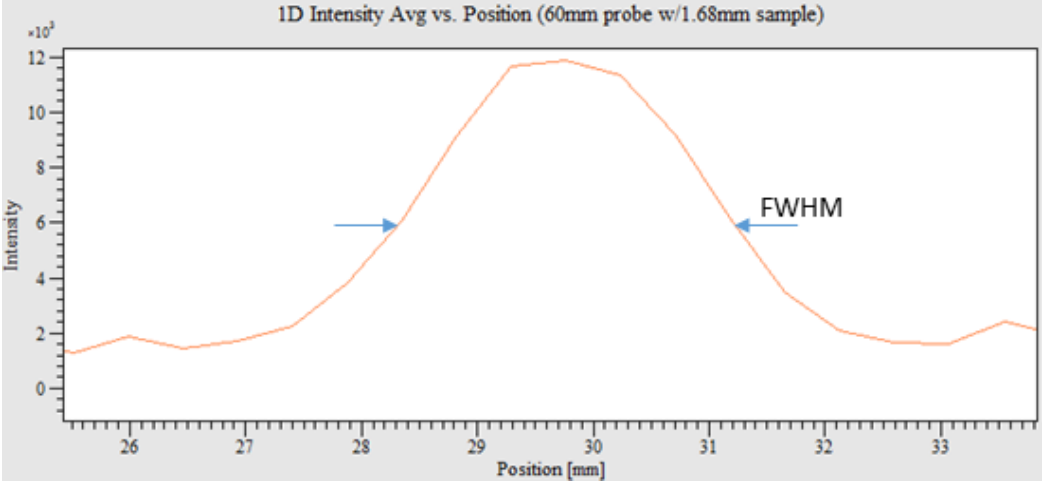
Stacked rubber phantoms of various size



6.3 mm rubber phantom



3.15 mm rubber phantom



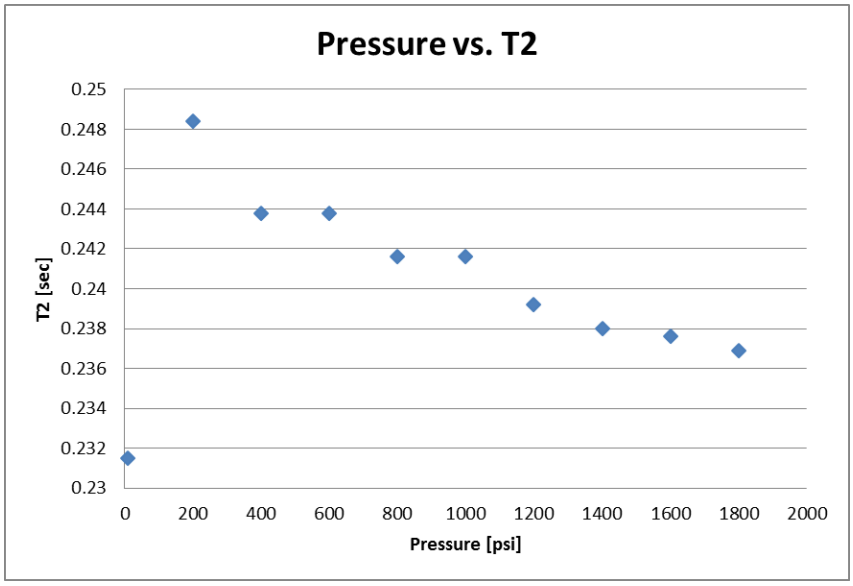
1.68 mm rubber phantom

60mm Probe	**6.3mm Sample**	**3.15mm Sample**	**1.68mm Sample**
FWHM	6.4mm	3.5mm	2.90mm
Error	1.59%	11.11%	72.62%

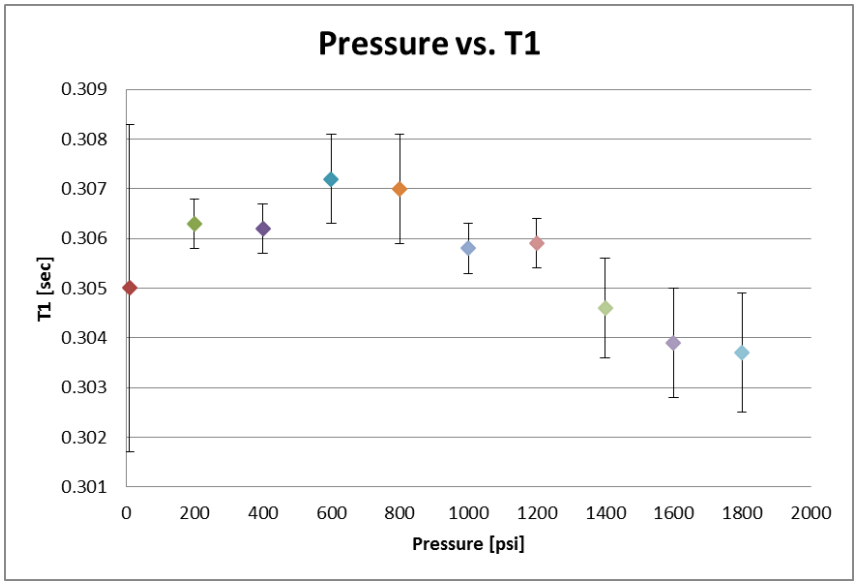
Phantom FWHM comparison to actual thickness

APPENDIX B

T1 AND T2 PRESSURE DEPENDENCE DATA



T2 change as pressure is increased



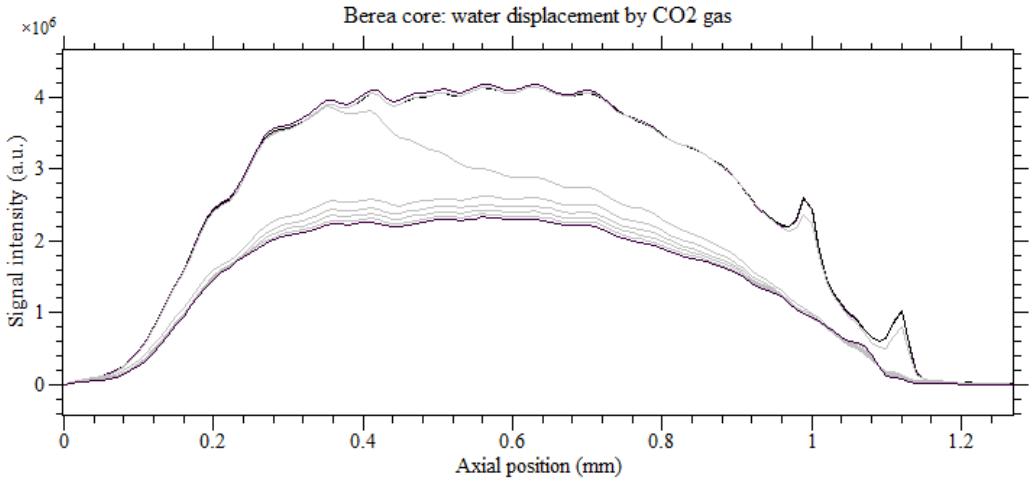
T1 change as pressure is increased

Pressure [psi]	T2 [sec]	T1 [sec]
10	0.2315	0.305
200	0.2484	0.3063
400	0.2438	0.3062
600	0.2438	0.3072
800	0.2416	0.307
1000	0.2416	0.3058
1200	0.2392	0.3059
1400	0.238	0.3046
1600	0.2376	0.3039
1800	0.2369	0.3037

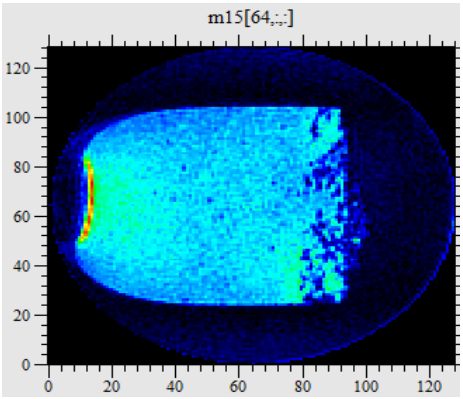
T1 and T2 values obtained at specified pressures

APPENDIX C

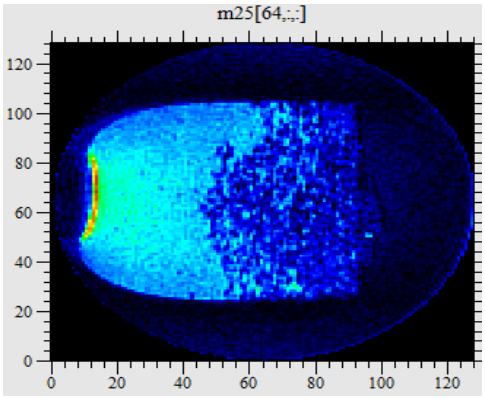
VISCOUS FINGERING DATA



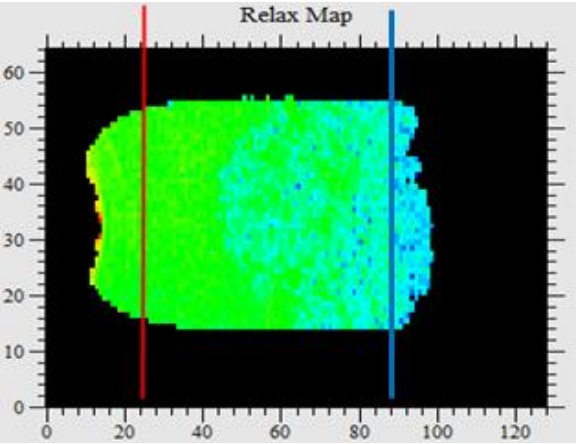
Water displacement by CO2 gas (uncropped)



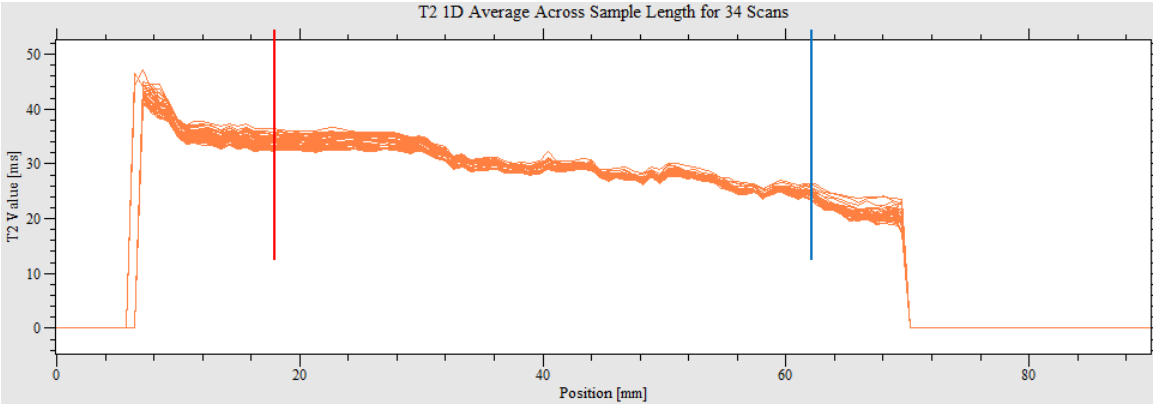
ZTE image of saturated bead pack



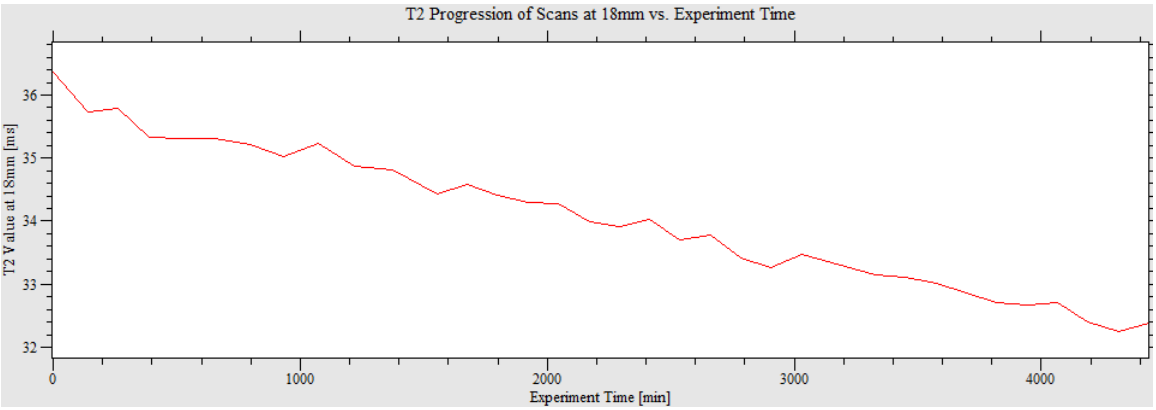
ZTE image of saturated bead pack after pressure inversion incident



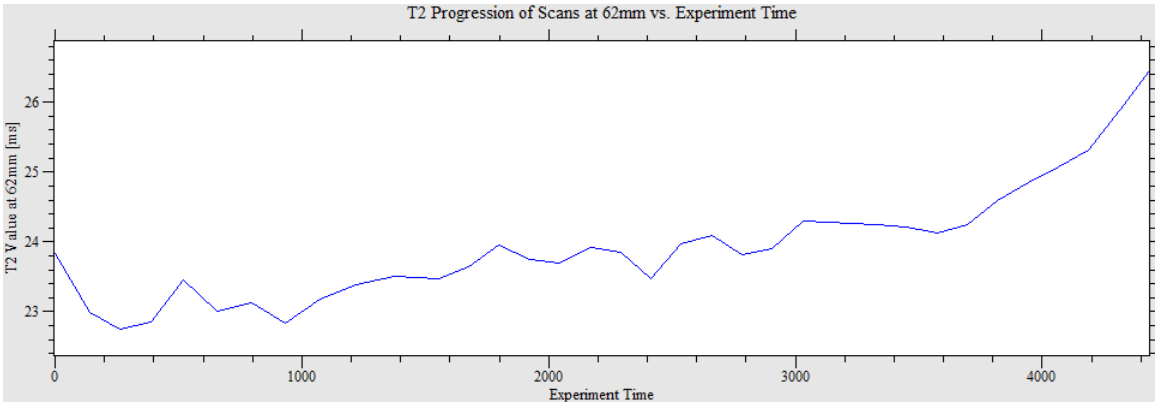
T2 relaxation map from MSME scans



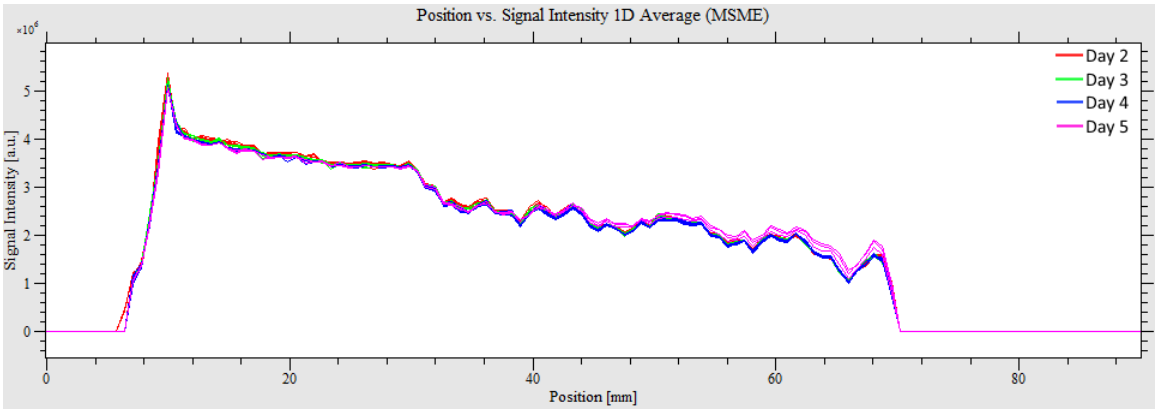
T2 1D profile for 34 sequential scans



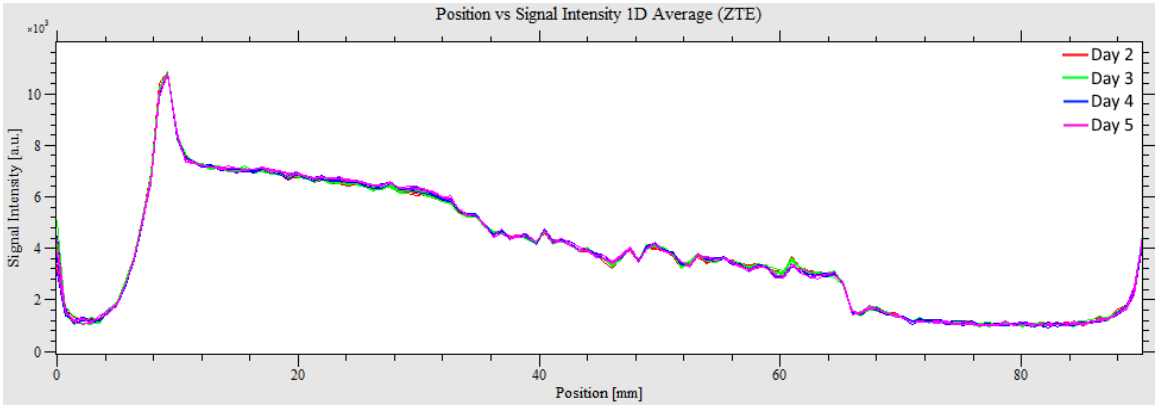
T2 progression for 34 sequential scans at 18 mm (red lines in figures above)



T2 progression for 34 sequential scans at 62 mm (blue lines in figures above)



1D average profile for MSME data



1D average profile for ZTE data

APPENDIX D

CAPILLARY TRAPPING DATA

Scan (Non-Wetting Phase)	**Normalized 1D Avg. Intensity from 28-54mm**					
Run	Air (AFLAS)	Air (FEP)	CO2 (FEP)	CO2 (FEP)	scCO2 (FEP)	scCO2 (FEP)
Fully Saturated	0	0	0	0	0	0
Drainage-1	0.00	0.01	0.02	0.02	0.40	0.30
Drainage-2	0.30	0.22	0.36	0.43	0.44	0.40
Drainage-3	0.35	-----	0.47	0.48	0.49	0.43
Drainage-4 ($S_{Initial}$)	0.41	0.42	0.51	0.51	0.51	0.47
Imbibition Final ($S_{Residual}$)	0.28	0.32	0.36	0.37	0.27	0.30
$S_{Residual}/S_{Initial}$	0.68	0.76	0.71	0.73	0.53	0.64

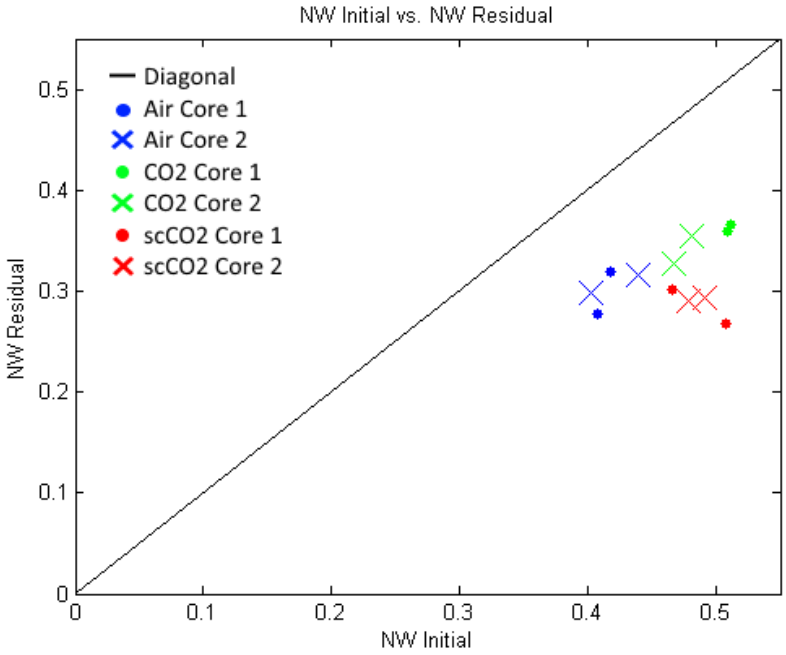
Data for rock core #2

Scan (Non-Wetting Phase)	**Normalized 1D Avg. Intensity from 28-54mm**					
Run	Air (FEP)	Air (FEP)	CO2 (FEP)	CO2 (FEP)	scCO2 (FEP)	scCO2 (FEP)
Fully Saturated	0	0	0	0	0	0
Drainage-1	0.10	0.03	0.01	0.04	0.19	0.18
Drainage-2	0.35	0.36	0.34	0.39	0.42	0.40
Drainage-3	0.38	0.40	0.41	0.44	0.44	0.42
Drainage-4 ($S_{Initial}$)	0.40	0.44	0.47	0.48	0.49	0.48
Imbibition Final ($S_{Residual}$)	0.30	0.32	0.33	0.35	0.29	0.29
$S_{Residual}/S_{Initial}$	0.75	0.73	0.70	0.73	0.59	0.60

Data for rock core #3

Scan (Non-Wetting Phase)	**Average values for all 4 runs of air, CO2, and scCO2 with standard deviation**		
Run	Air	CO2	scCO2
Drainage-4 ($S_{Initial}$)	0.42±0.02	0.49±0.02	0.49±0.02
Imbibition Final ($S_{Residual}$)	0.31±0.02	0.35±0.02	0.29±0.01
$S_{Residual}/S_{Initial}$	0.73±0.04	0.72±0.02	0.59±0.05

Summarized averages of all runs on both cores



Initial NW saturation fraction vs. residual NW saturation fraction

	Nitrogen	**Air**	**CO2**	**scCO2**	**Water(70F)**	**Water(95F)**
Viscosity [mPa*s]	0.0191	0.0192	0.0723	0.0225	0.972	0.719

Viscosities of fluids

Run	Air Water	CO2 Water	scCO2 Water
Surface Tension [mN/m]	72	30.84	28.35

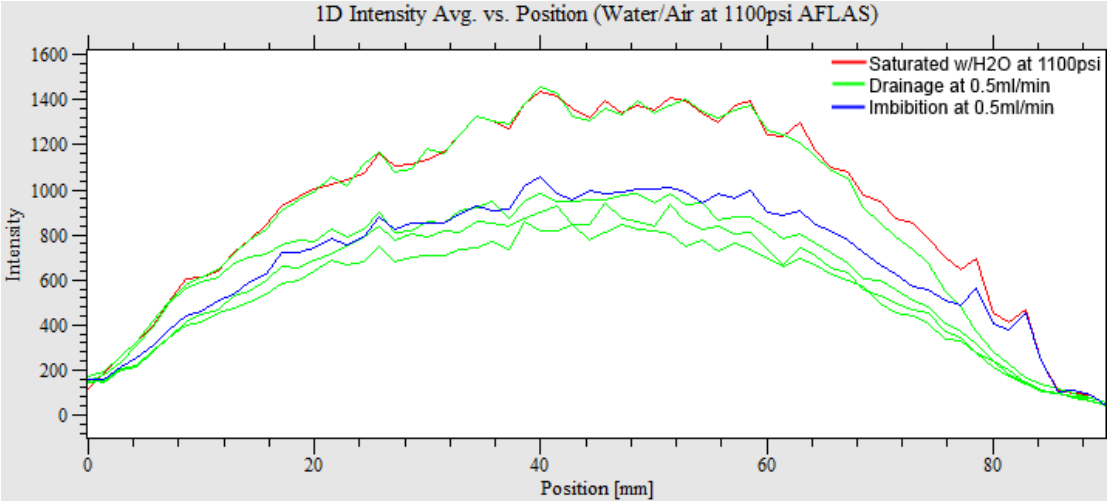
Surface tensions of fluids from Bachu et al

Name	Ca	logCa
Air	2.720E-08	-7.566
CO2	2.391E-07	-6.621
scCO2	8.094E-08	-7.092
Water (Air)	1.377E-06	-5.861
Water (CO2)	3.214E-06	-5.493
Water (scCO2)	3.497E-06	-5.456

Calculated Ca number for drainage/imbibition of invading fluid

Scan	Average Intensity of 2D Plot/1D Avg. 28-54	Integral (10^6)	FID Area
M9bs (fully saturated, Soriginal)	730/1320	2.99	12725
M10bs (Drainage-1)	705/1320	2.89	12465
M11bs (Drainage-2)	511/931	2.09	11770
M12bs (Drainage-3)	458/859	1.88	11675
M13bs (Drainage-4)	422/782	1.73	11609
M14bs (Imbibition)	529/955	2.17	11980
M7 (Empty)			10697

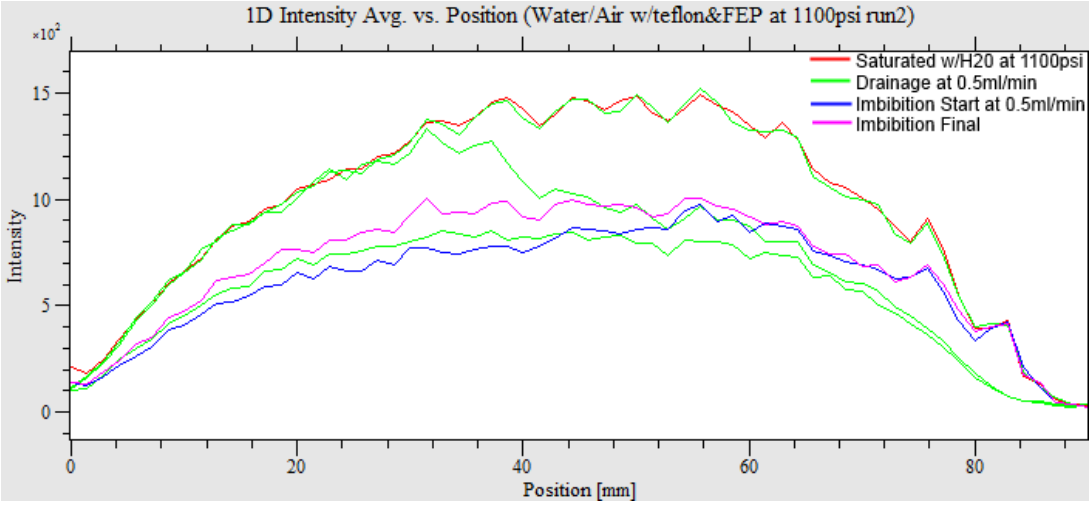
Air/water rock core #2, run 1 data



Air/water rock core #2, run 1 ZTE data

Scan	Average Intensity of 2D Plot/1D Avg. 28-54	Integral	FID Area
M23bs (fully saturated, Soriginal)	755/1400	3090000	12180
M24bs (Drainage-1)	747/1390	3060000	12095
M26bs (Drainage-2)	570/1090	2330000	11200
M28bs (End of drainage)	434/815	1780000	10545
M29bs (Imbibition Start)	462/808	1890000	~10744
M31bs (Imbibition End)	521/952	2130000	11015
M22 (Empty)			9595

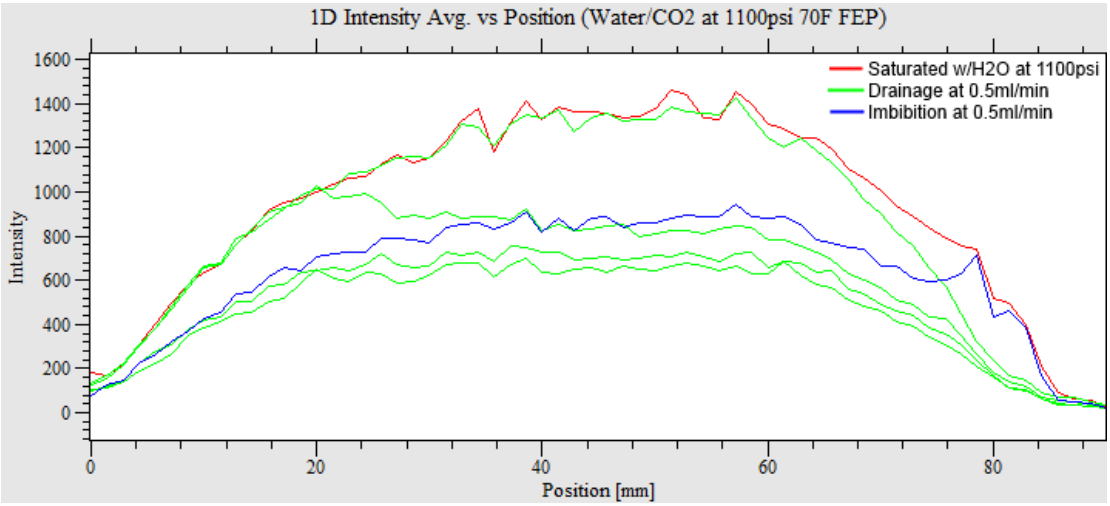
Air/water rock core #2, run 2 data



Air/water rock core #2, run 2 ZTE data

Scan	Average Intensity of 2D Plot/1D Avg. 28-54	Integral (10^6)	FID Area
M16bs (fully saturated, Soriginal)	735/1330	3.01	12004
M17bs (Drainage-1)	699/1300	2.86	11918
M18bs (Drainage-2)	493/855	2.02	10995
M20bs (Drainage-3)	388/709	1.59	10400
M21bs (Drainage-4)	353/653	1.44	10280
M23bs (Imbibition)	483/853	1.98	10796
M15 (Empty)			9560

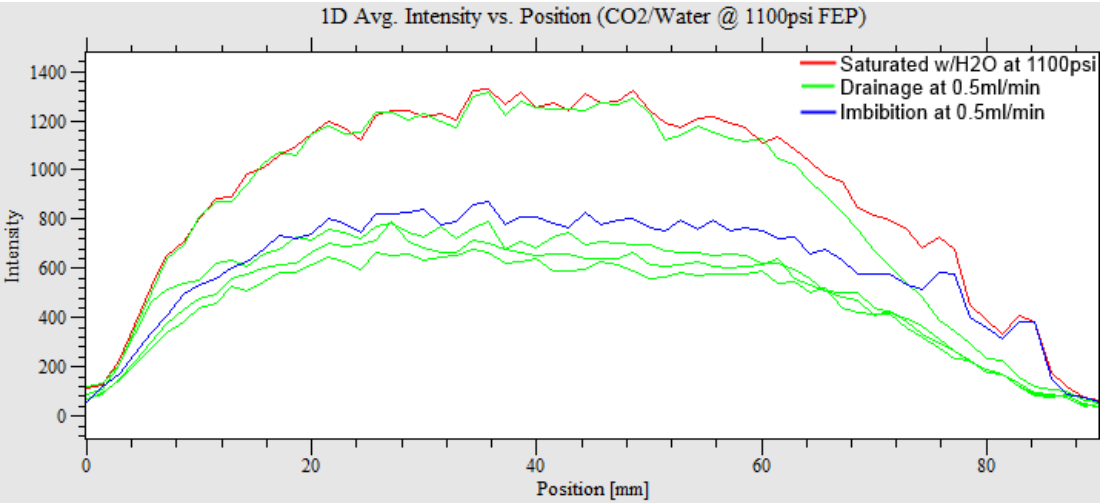
CO2/water rock core #2, run1 data



CO2/water rock core #2, run 1 ZTE data

Scan	Average Intensity of 2D Plot/1D Avg. 28-54	Integral (10^6)	FID Area
M5bs (fully saturated, Soriginal)	703/1260	2.88	11335
M6bs (Drainage-1)	664/1230	2.72	11071
M7bs (Drainage-2)	401/714	1.64	10096
M8bs (Drainage-3)	372/658	1.52	10035
M9bs (Drainage-4)	344/616	1.41	9985
M12bs (Imbibition)	465/799	1.91	10316
M3 (Empty)			9250

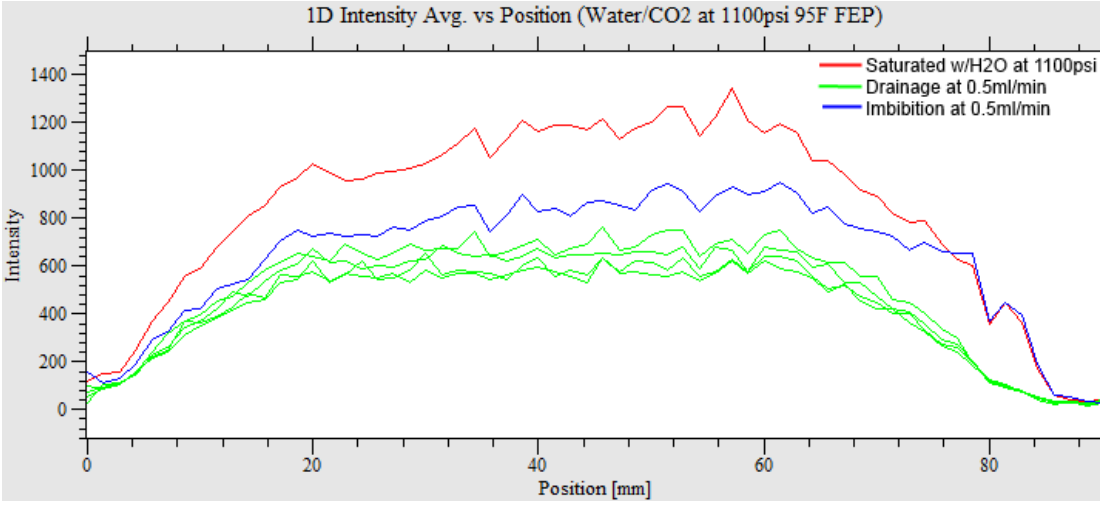
CO2/water rock core #2, run 2 data



CO2/water rock core #2, run 2 ZTE data

Scan	Average Intensity of 2D Plot/1D Avg. 28-54	Integral (10^6)	FID Area
M25bs (fully saturated, Soriginal)	640/1150	2.62	11455
M27bs (Drainage-1)	354/692	1.45	10151
M28bs (Drainage-2)	326/647	1.34	10125
M29bs (Drainage-3)	306/591	1.26	10100
M30bs (Drainage-4)	295/567	1.21	10072
M32bs (Imbibition)	475/843	1.95	10685
M24 (Empty)			9500

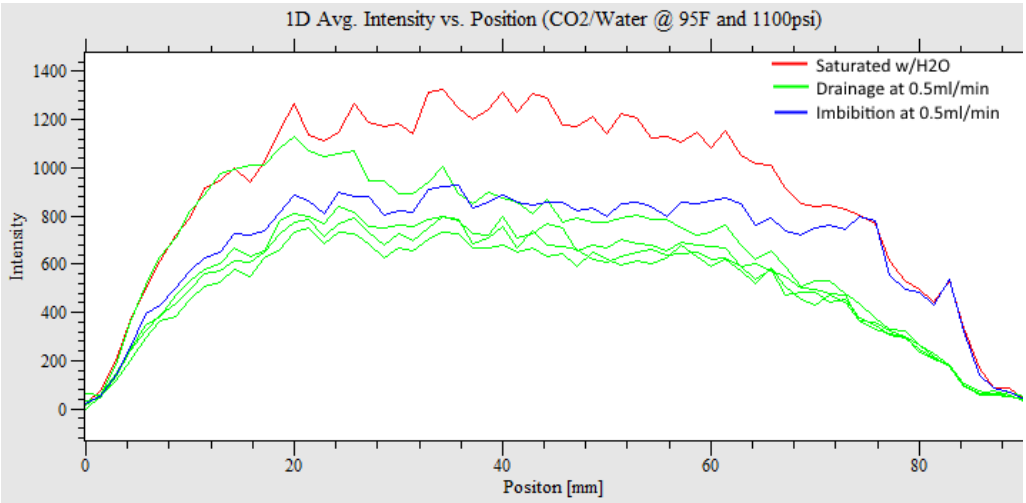
scCO2/water rock core #2, run 1 data



scCO2/water rock core #2, run1 ZTE data

Scan	Average Intensity of 2D Plot /1D Avg 28-54	Integral (10^6)	FID Area
M5bs (fully saturated, Soriginal)	635/1220	2.60	
M7bs (Drainage-1)	449/854	1.84	
M8bs (Drainage-2)	361/732	1.48	
M9bs (Drainage-3)	344/694	1.41	
M10bs (Drainage-4)	321/652	1.32	
M13bs (Imbibition)	460/852	1.88	
M4 (Empty)			

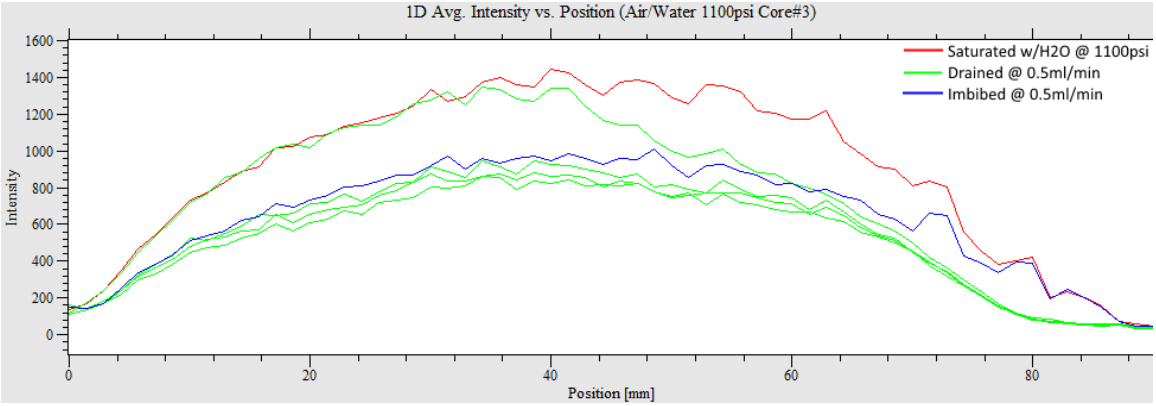
scCO2/water rock core#2, run 2 data



scCO2/water rock core #2, run 2 ZTE data

Scan	Average Intensity of 2D Plot / 1D Avg 28-54	Integral (10^6)	FID Area
M15bs (fully saturated, Soriginal)	708 / 1340	2.90	11475
M17bs (Drainage-1)	596/1200	2.44	11110
M18bs (Drainage-2)	445/872	1.82	10405
M19bs (Drainage-3)	424/827	1.74	10345
M20bs (Drainage-4)	403 / 801	1.65	10306
M21bs (Imbibition)	501 / 940	2.05	10667
M14 (Empty)			9370

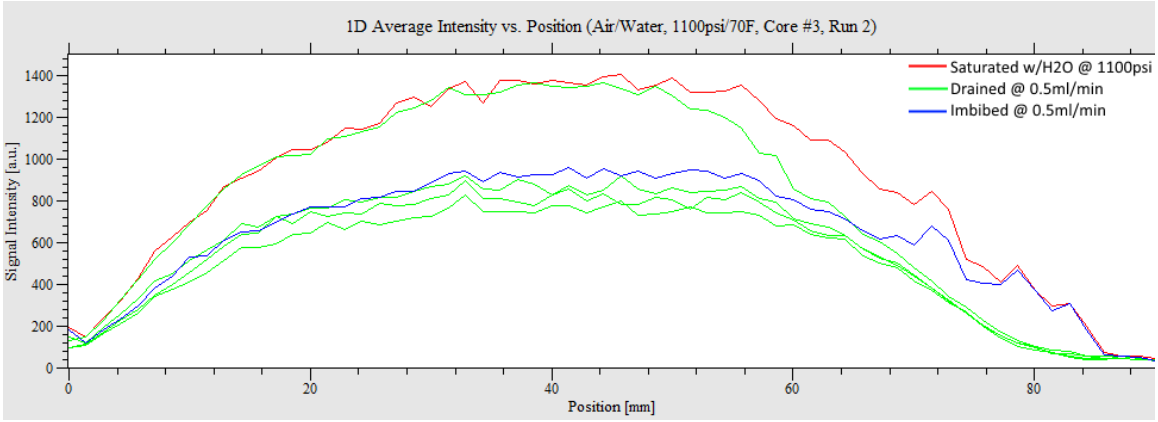
Air/water rock core #3, run 1 data



Air/water rock core #3, run 1 ZTE data

Scan	Average Intensity of 2D Plot / 1D Avg 28-54	Integral (10^6)	FID Area
M63bs (fully saturated, Soriginal)	712/1350		
M65bs (Drainage-1)	631/1310		
M66bs (Drainage-2)	450/865		
M67bs (Drainage-3)	426/813		
M68bs (Drainage-4)	393/757		
M69bs (Imbibition)	499/924		
M62 (Empty)			

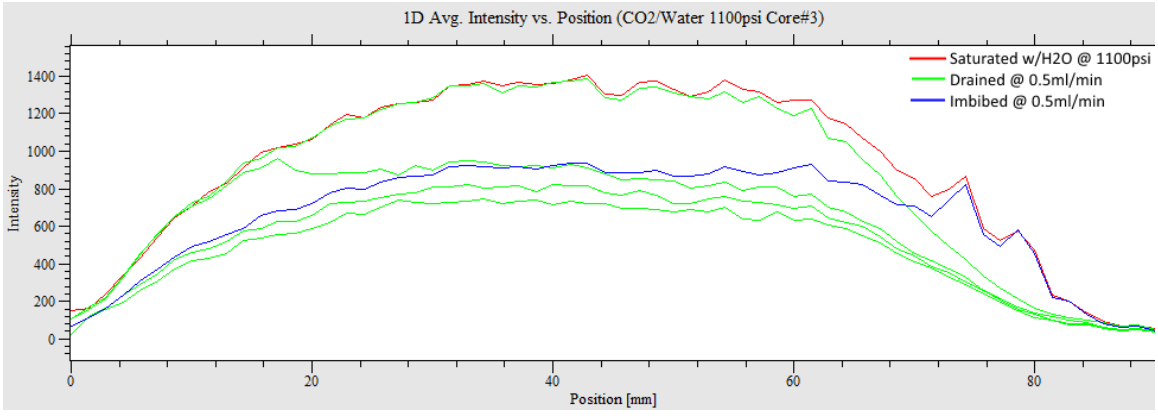
Air/water rock core #3, run 2 data



Air/water rock core #3, run 2 ZTE data

Scan	Average Intensity of 2D Plot / 1D Avg 28-54	Integral (10^6)	FID Area
M24bs (fully saturated, Soriginal)	727 / 1340	2.98	11586
M26bs (Drainage-1)	685/1330	2.81	11280
M27bs (Drainage-2)	490/889	2.01	10462
M28bs (Drainage-3)	415/786	1.70	10280
M29bs (Drainage-4)	378 / 714	1.55	10180
M31bs (Imbibition)	512 / 901	2.10	10675
M23 (Empty)			9340

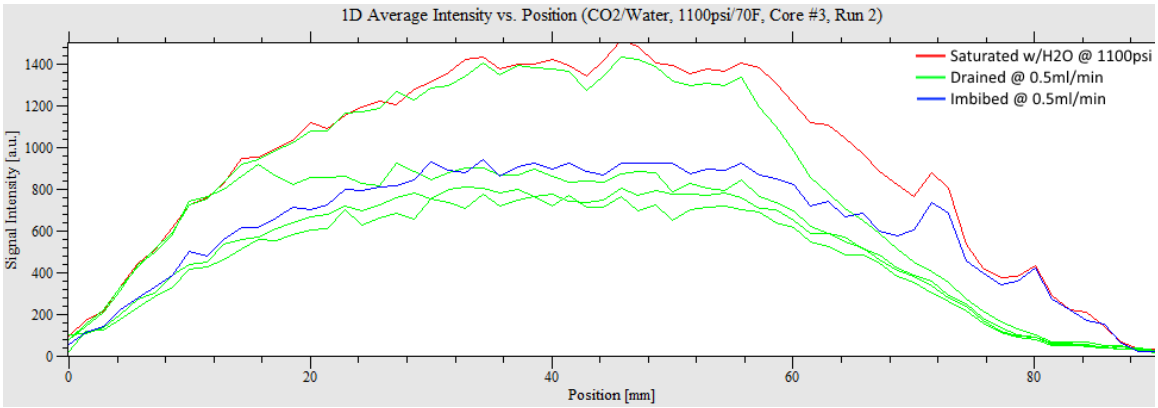
CO2/water rock core #3, run 1 data



CO2/water rock core #3, run 1 ZTE data

Scan	Average Intensity of 2D Plot / 1D Avg 28-54	Integral (10^6)	FID Area
M54bs (fully saturated, Soriginal)	728/1400		
M56bs (Drainage-1)	647/1350		
M57bs (Drainage-2)	456/858		
M58bs (Drainage-3)	394/780		
M59bs (Drainage-4)	359/726		
M60bs (Imbibition)	479/904		
M53 (Empty)			

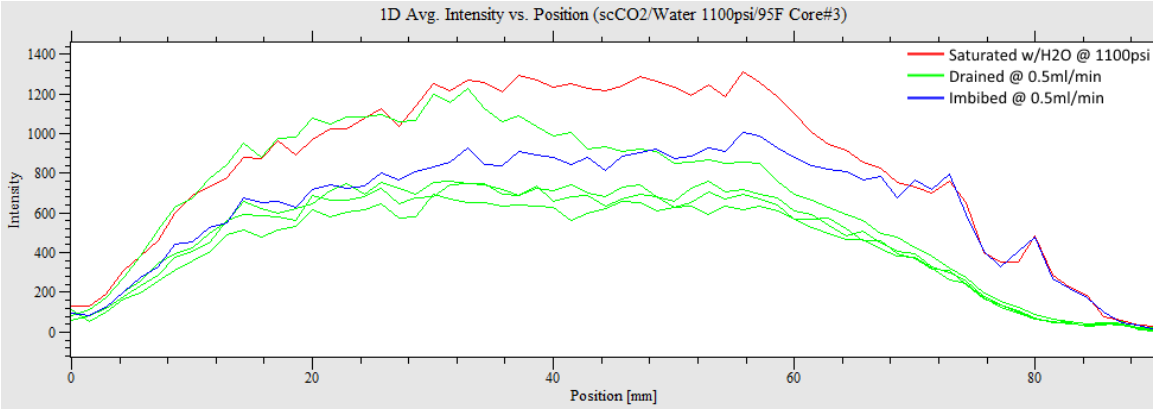
CO2/water rock core #3, run 2 data



CO2/water rock core #3, run 2 ZTE data

Scan	Average Intensity of 2D Plot / 1D Avg 28-54	Integral (10^6)	FID Area
M34bs (fully saturated, Soriginal)	643 / 1240	2.64	11010
M36bs (Drainage-1)	502/1000	2.06	10750
M37bs (Drainage-2)	360/720	1.47	9880
M38bs (Drainage-3)	342/689	1.40	9815
M39bs (Drainage-4)	313 / 631	1.28	9709
M41bs (Imbibition)	473 / 876	1.94	10199
M33 (Empty)			9130

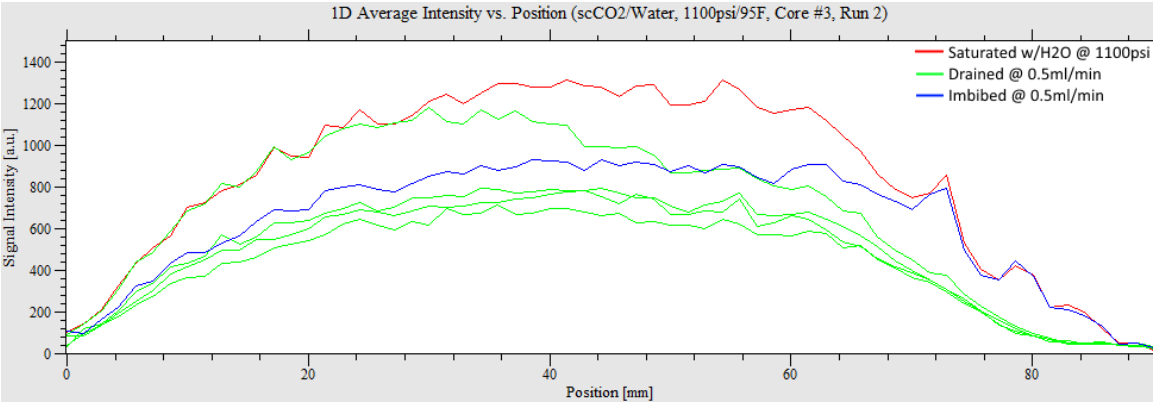
scCO2/water rock core #3, run 1 data



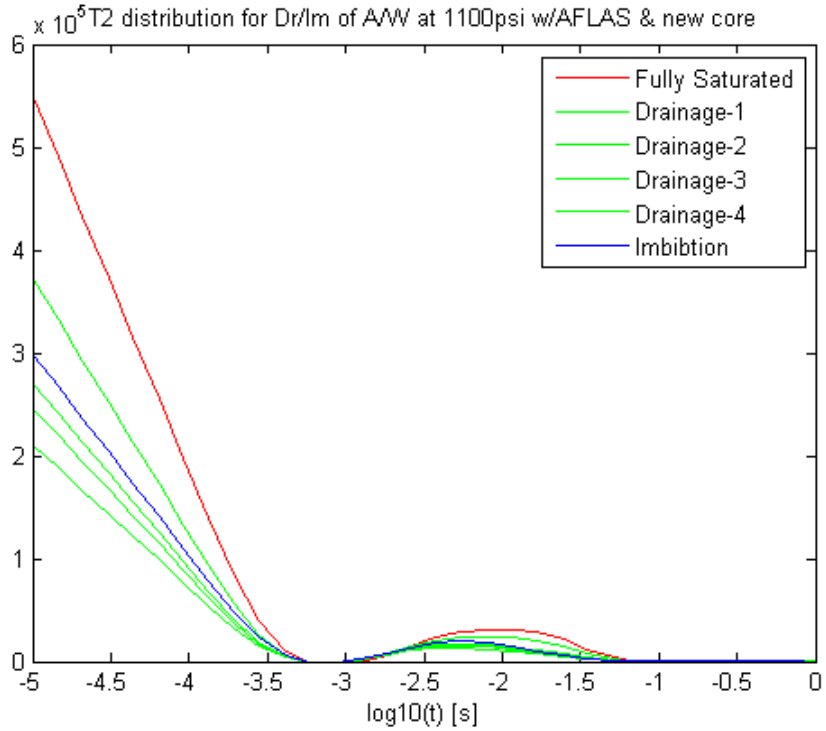
scCO2/water rock core #3, run 1 ZTE data

Scan	Average Intensity of 2D Plot / 1D Avg 28-54	Integral (10^6)	FID Area
M44bs (fully saturated, Soriginal)	663/1260		
M46bs (Drainage-1)	531/1040		
M47bs (Drainage-2)	387/759		
M48bs (Drainage-3)	363/726		
M49bs (Drainage-4)	334/659		
M51bs (Imbibition)	489/894		
M43 (Empty)			

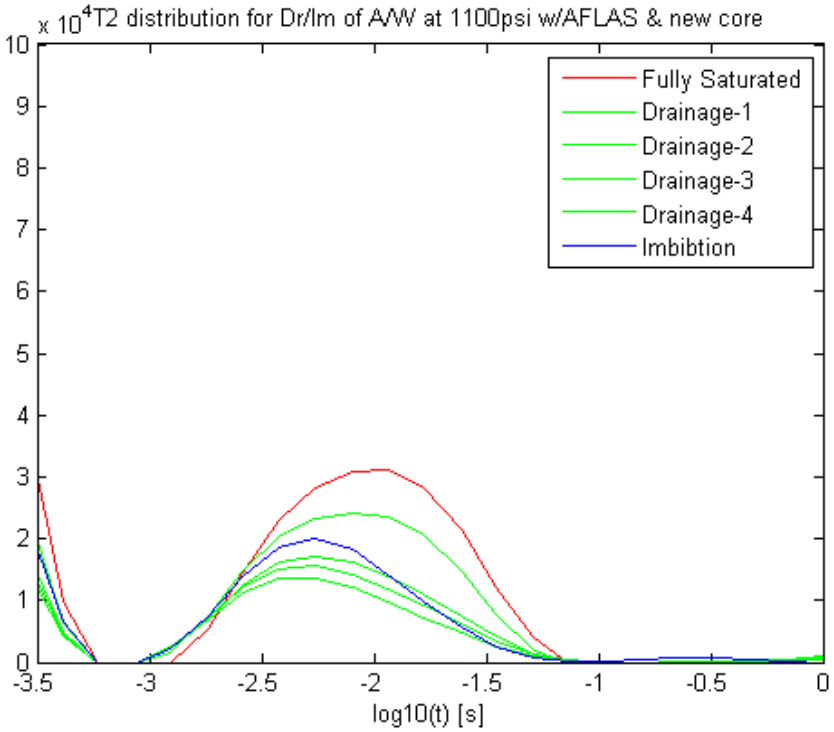
scCO2/water rock core #3, run 2 data



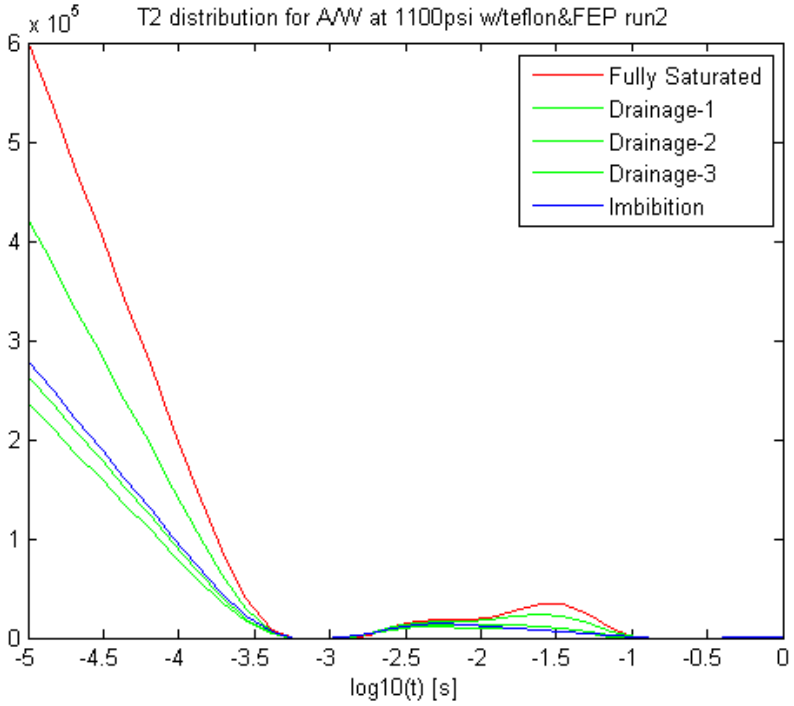
scCO2/water rock core #3, run 2 ZTE data



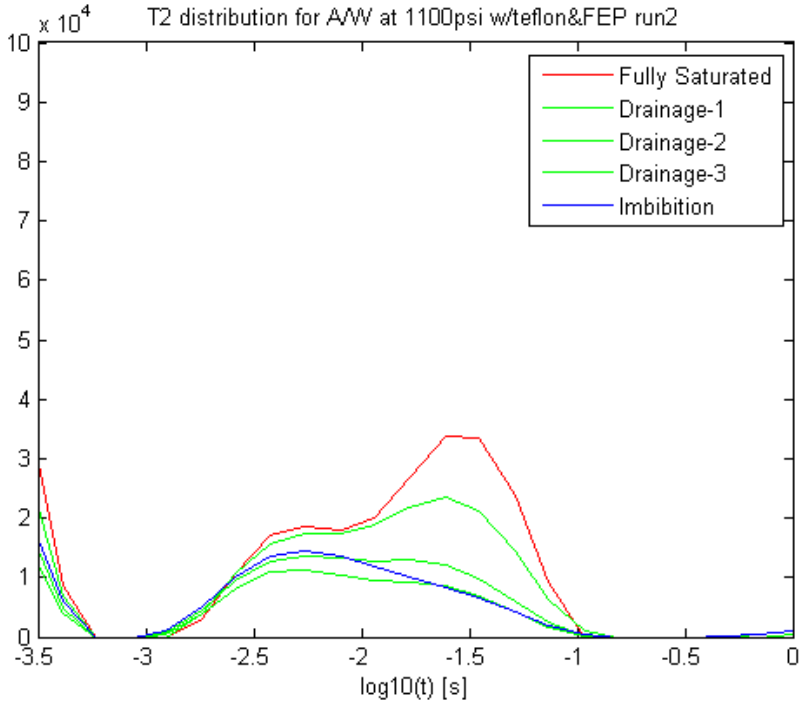
T2 distribution air/water rock core #2, run 1



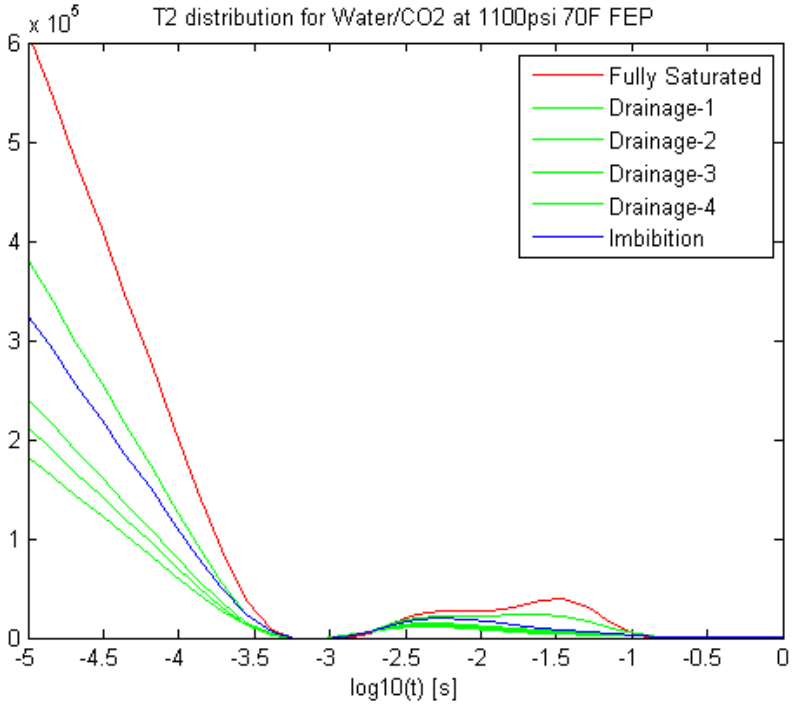
T2 distribution air/water rock core #2, run 1 zoomed



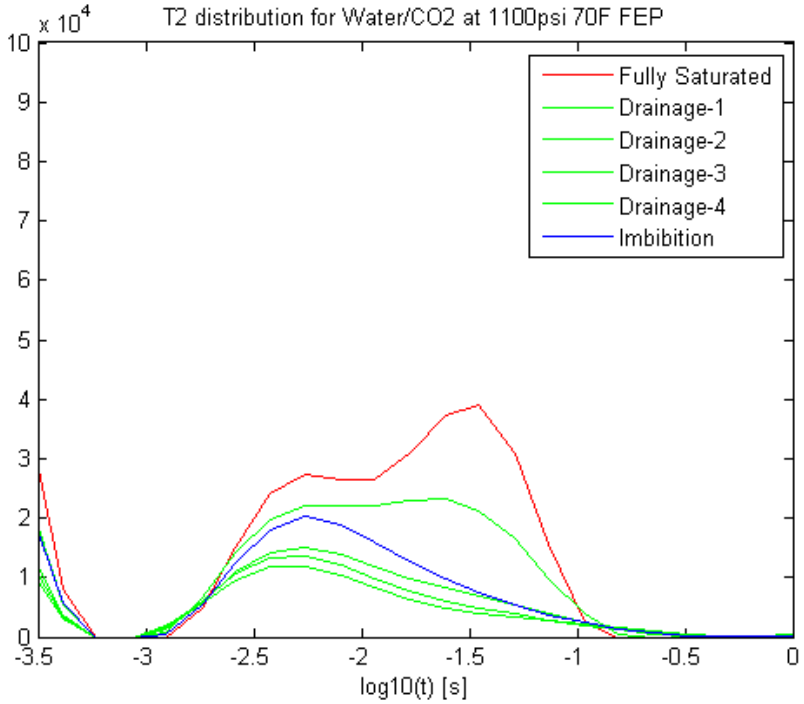
T2 distribution air/water rock core #2, run 2



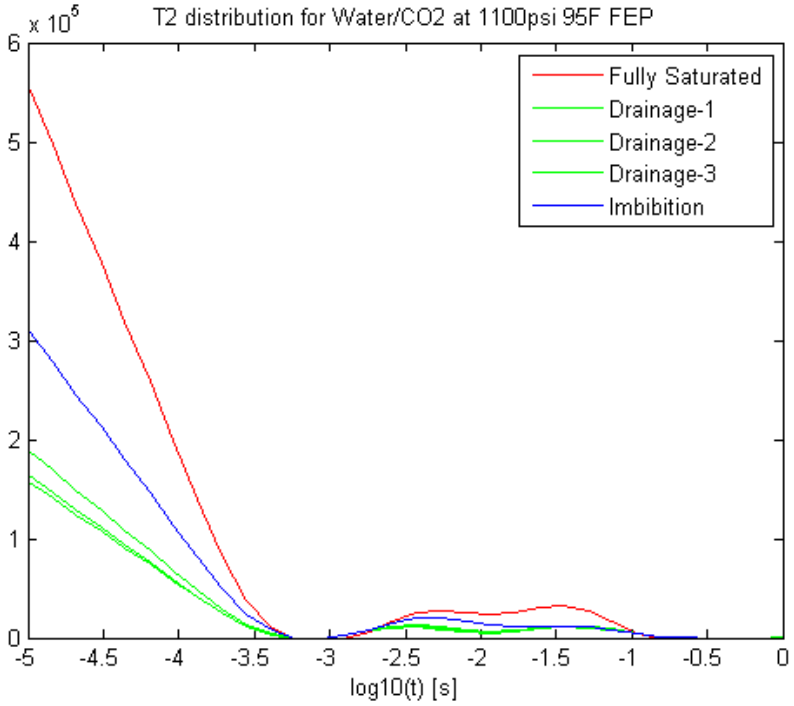
T2 distribution air/water rock core #2, run 2 zoomed



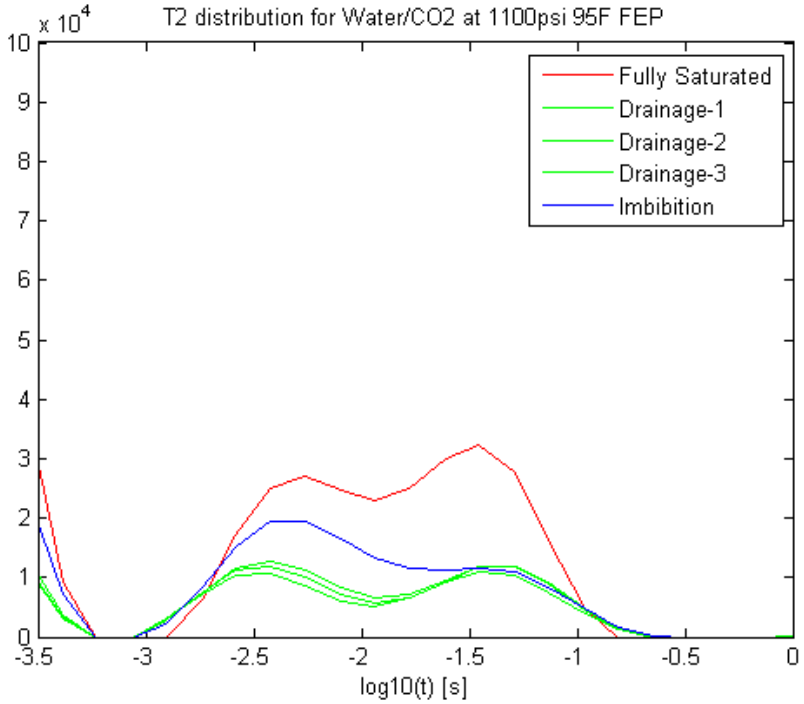
T2 distribution CO2/water rock core #2, run 1



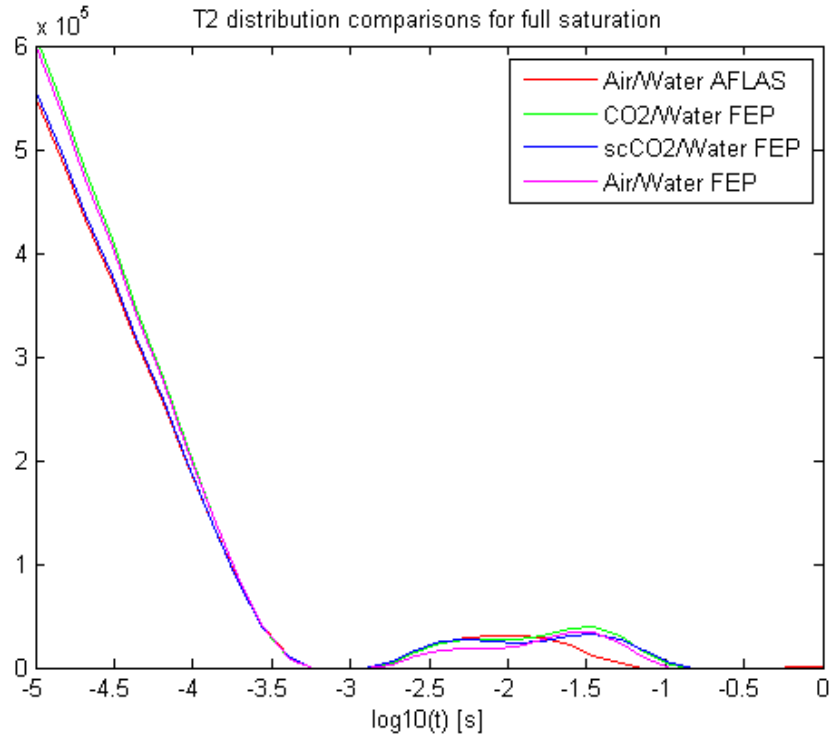
T2 distribution CO2/water rock core #2, run 1 zoomed



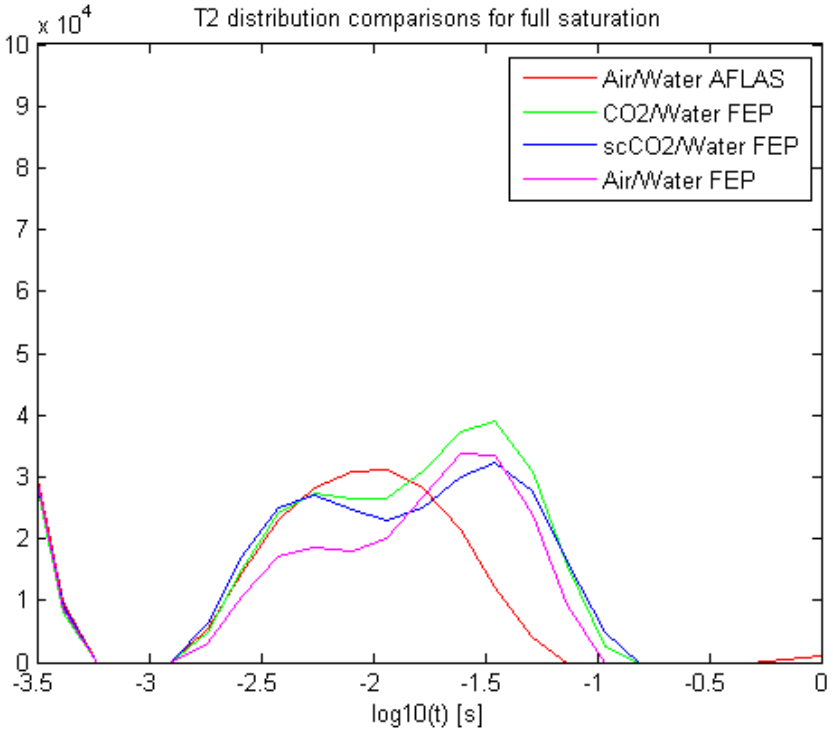
T2 distribution scCO2/water rock core #2, run 1



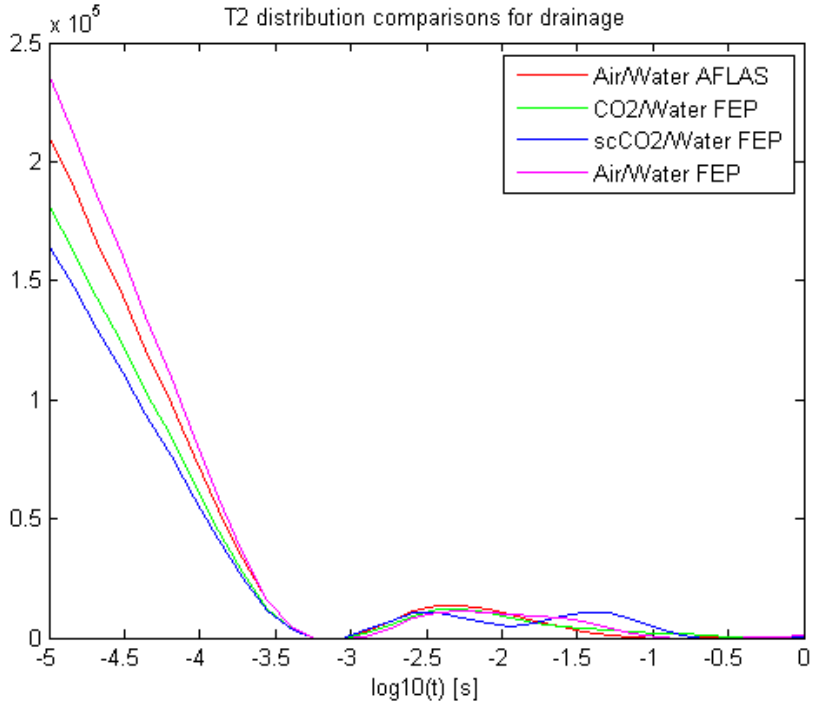
T2 distribution scCO2/water rock core #2, run 1 zoomed



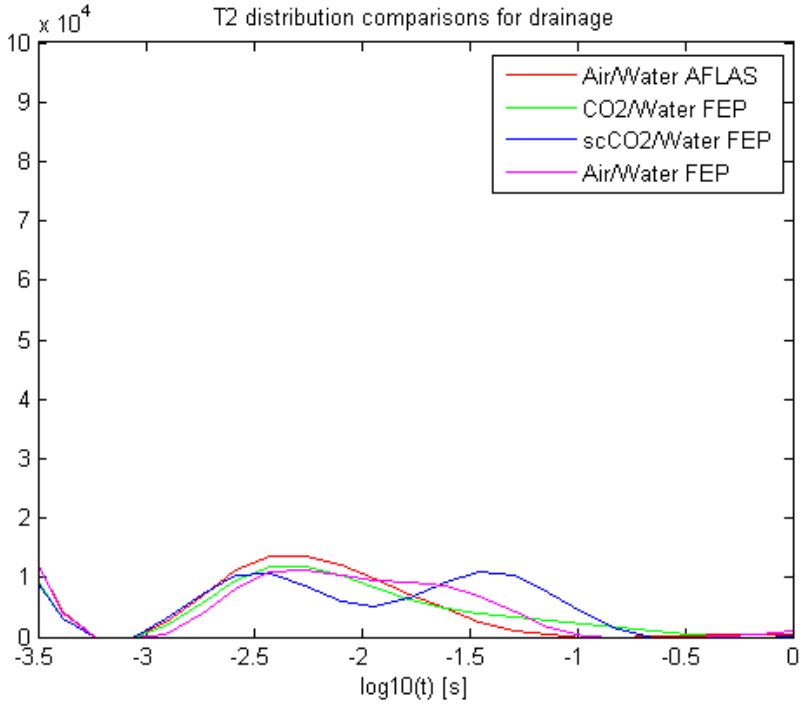
T2 distribution full saturation comparisons rock core #2, run 1



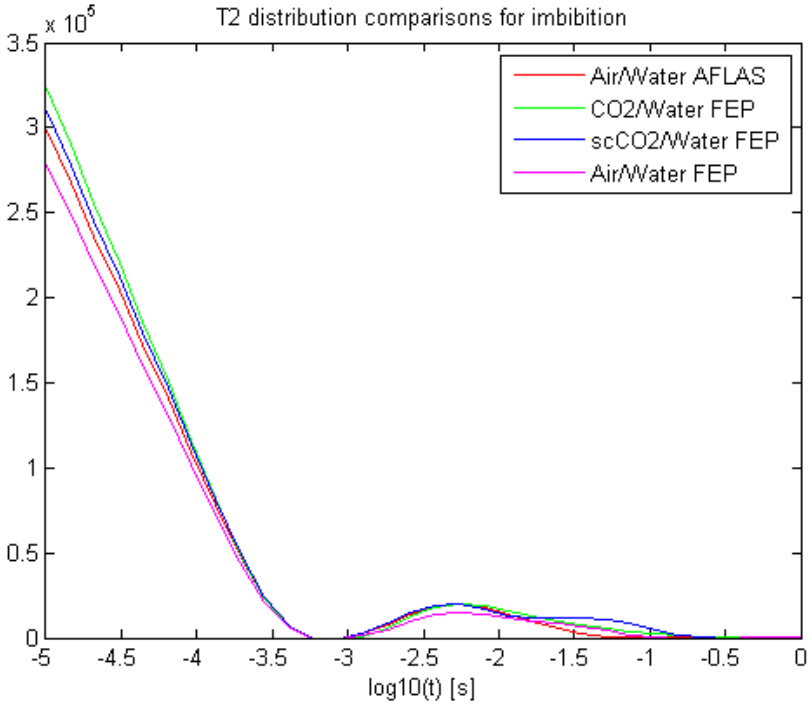
T2 distribution full saturation comparison rock core #2, run 1 zoomed



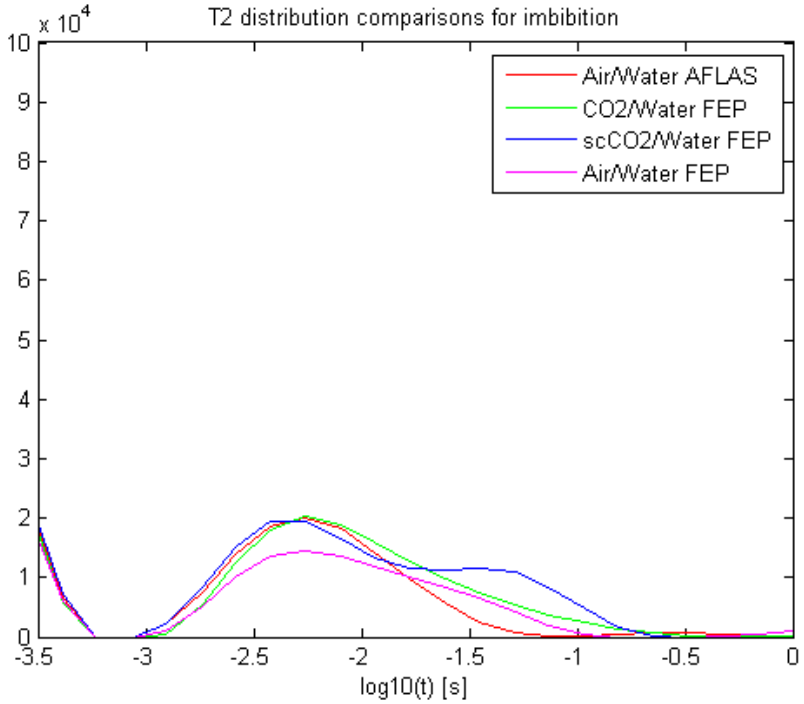
T2 distribution drainage comparison rock core #2, run 1



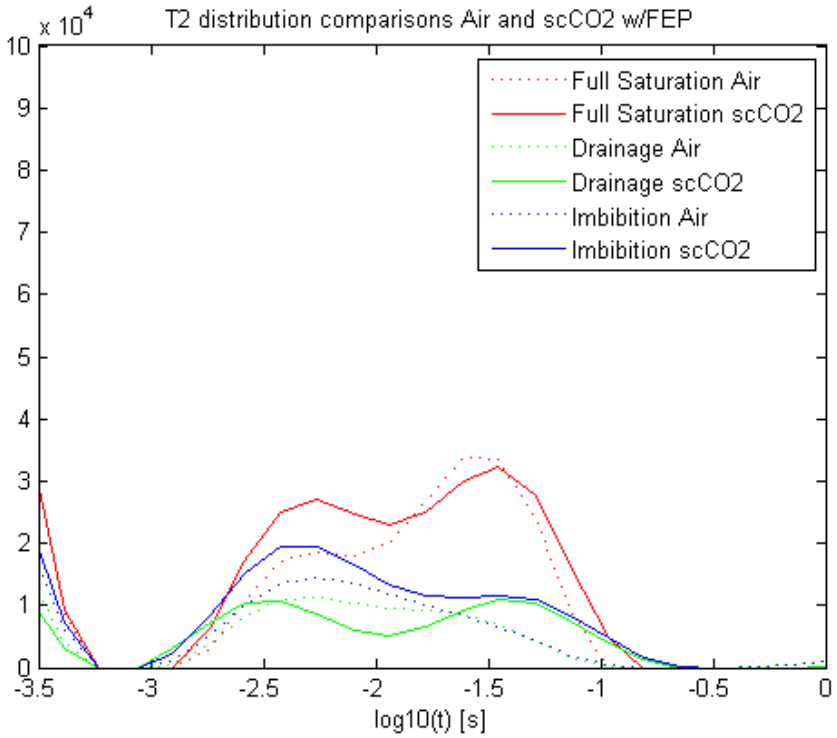
T2 distribution drainage comparison rock core #2, run 1 zoomed



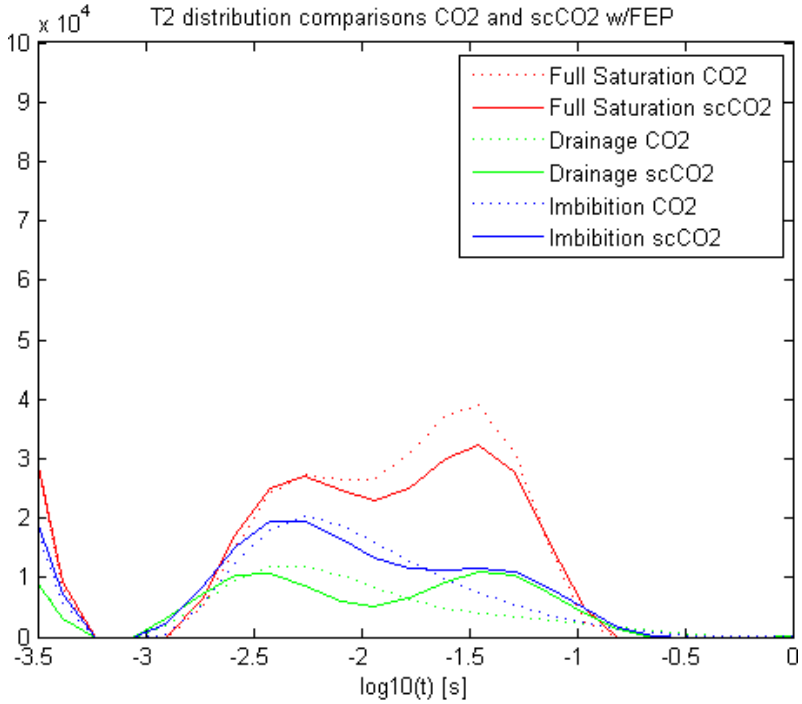
T2 distribution imbibition comparison rock core #2, run 1



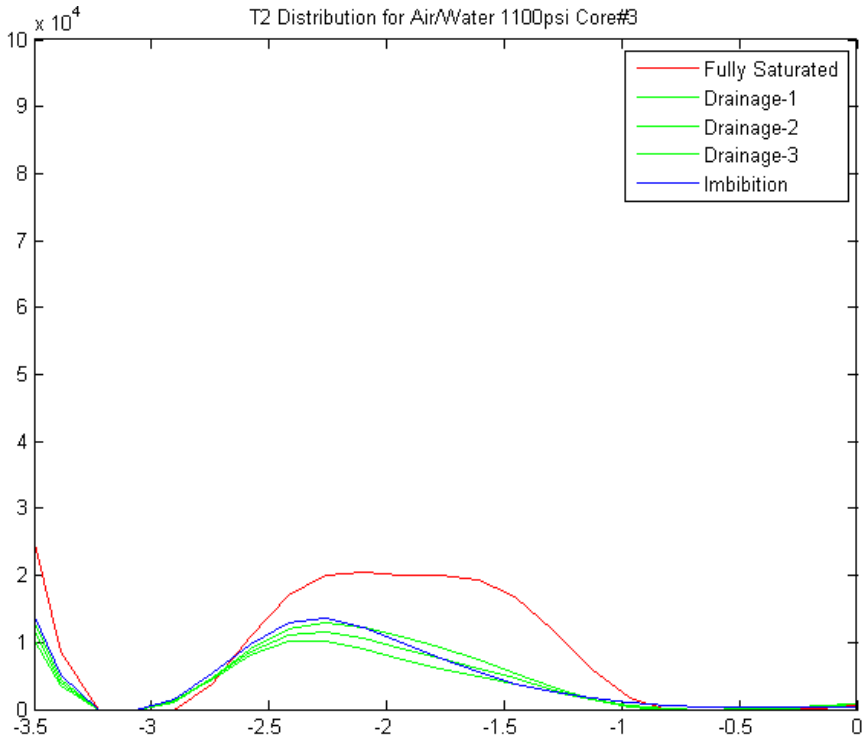
T2 distribution imbibition comparison rock core #2, run 1 zoomed



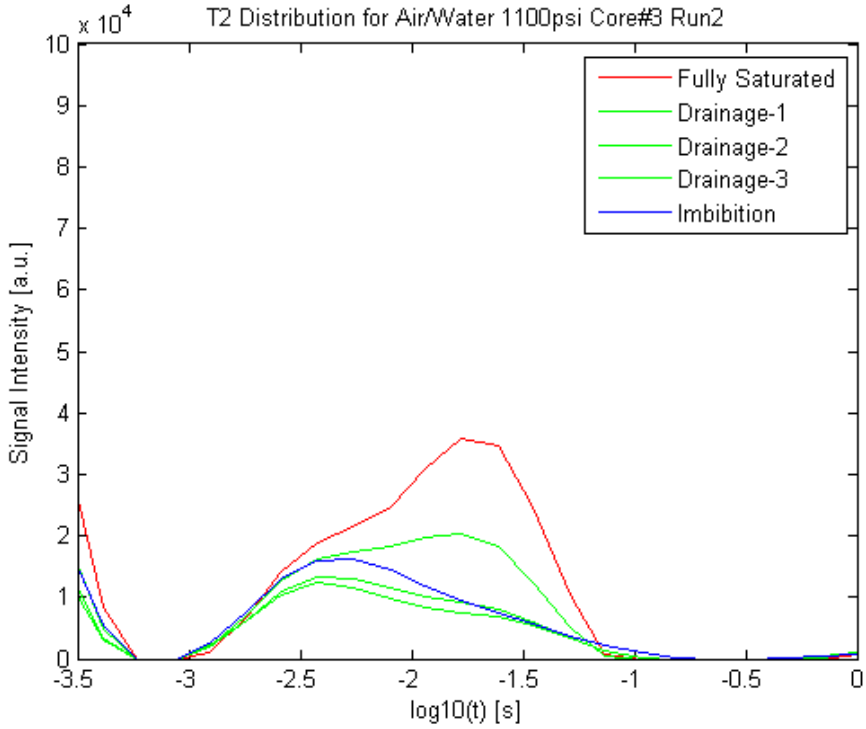
T2 distribution comparison between air and scCO2 rock core #2



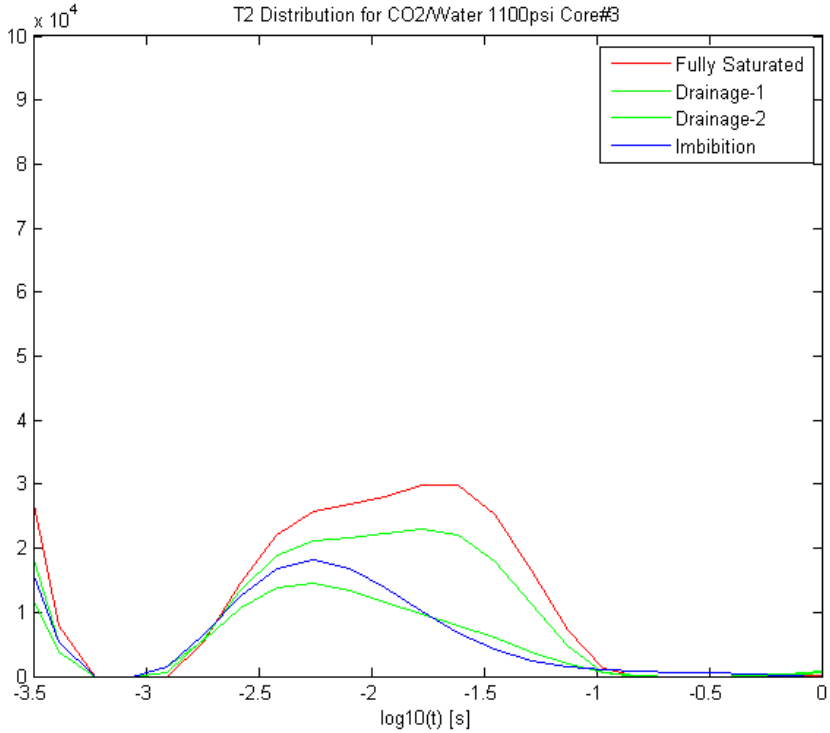
T2 distribution comparison between CO2 and scCO2 rock core #2



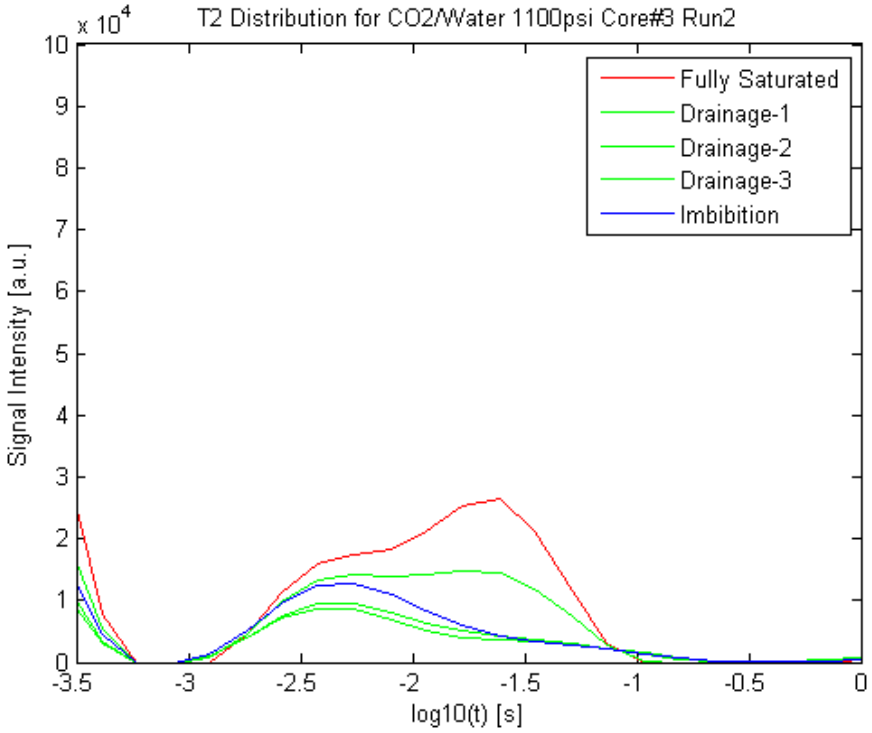
T2 distribution air/water rock core #3, run 1



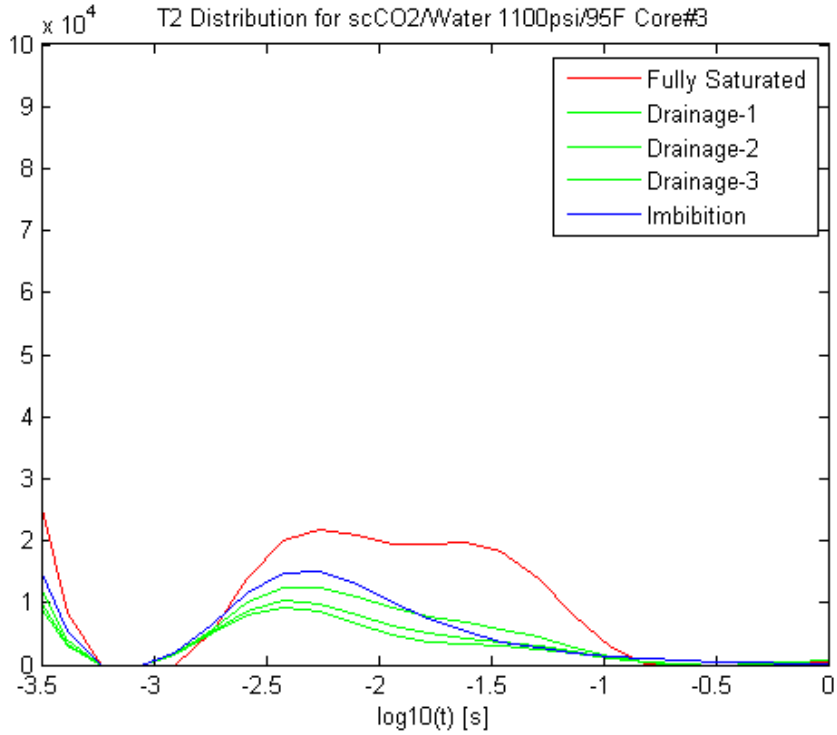
T2 distribution air/water rock core #3, run 2



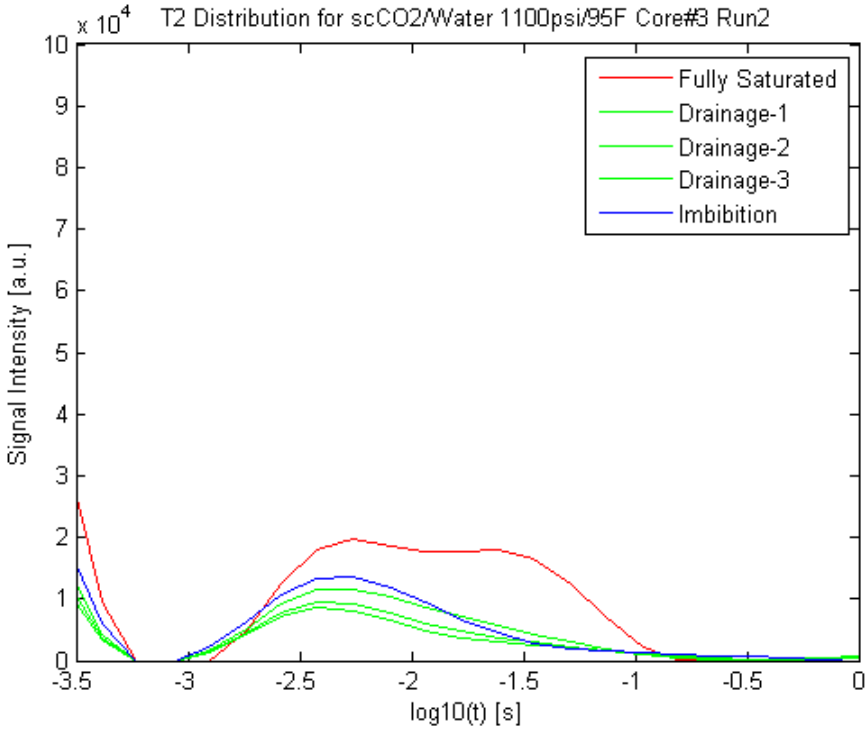
T2 distribution CO2/water rock core #3, run 1



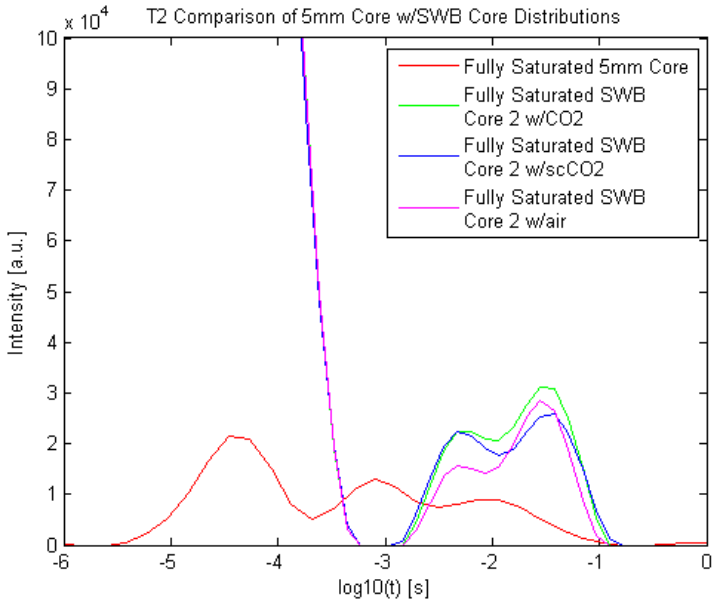
T2 distribution CO2/water rock core #3, run 2



T2 distribution scCO2/water rock core #3, run 1



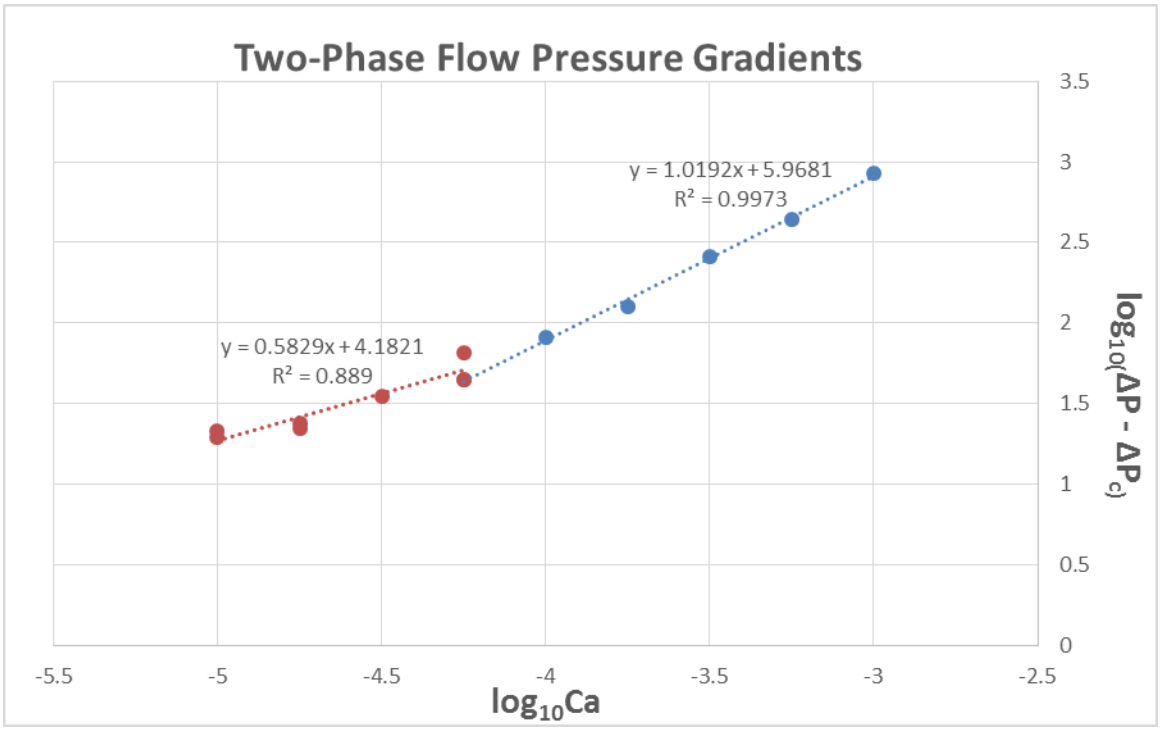
T2 distribution scCO2/water rock core #3, run 2



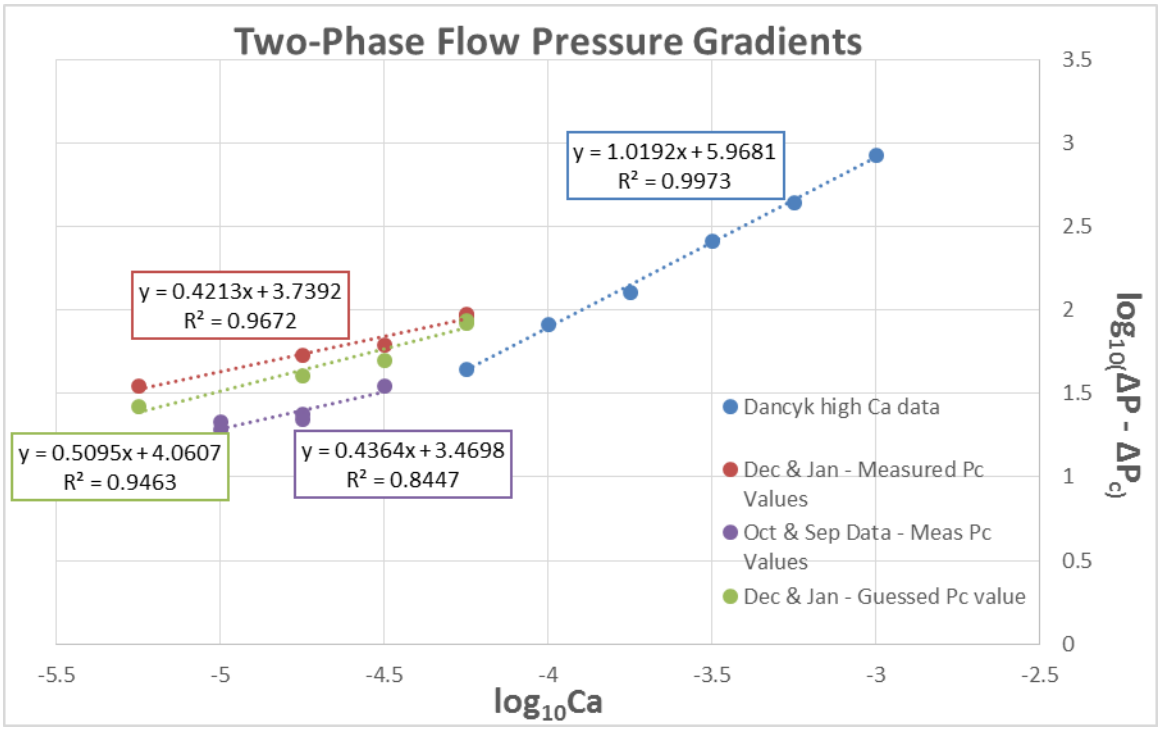
T2 distribution 5 mm core vs, 27 mm core

APPENDIX E

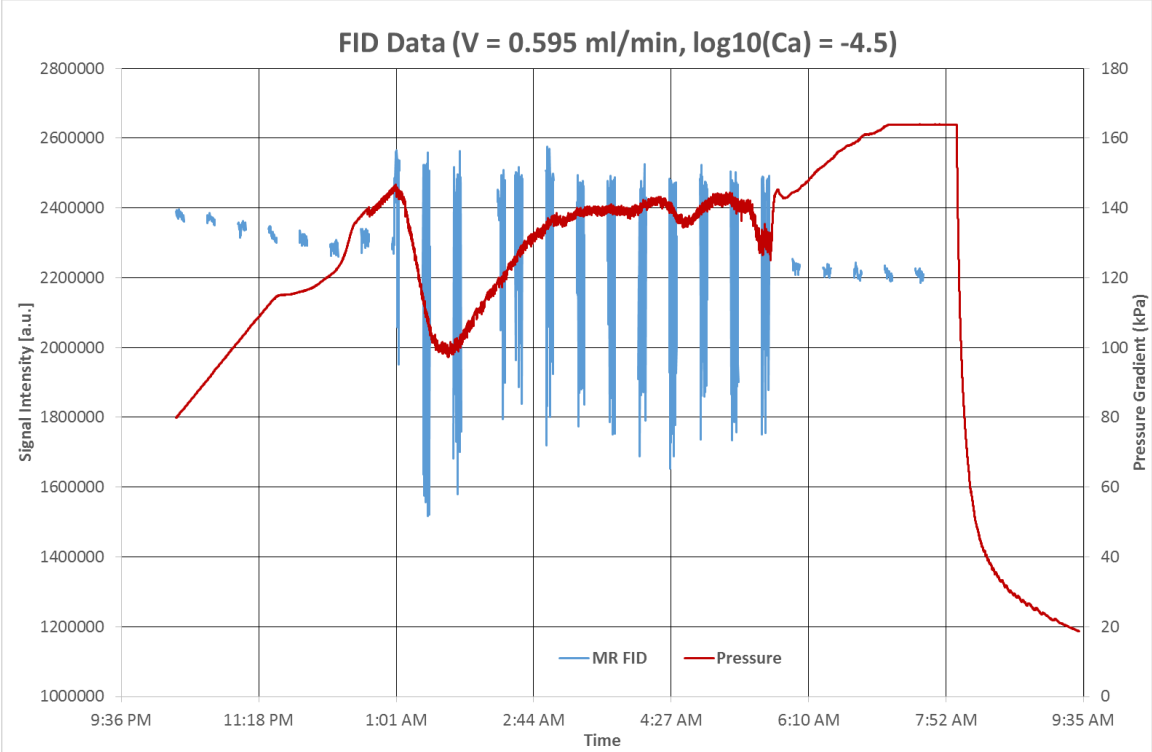
TWO PHASE FLOW DATA



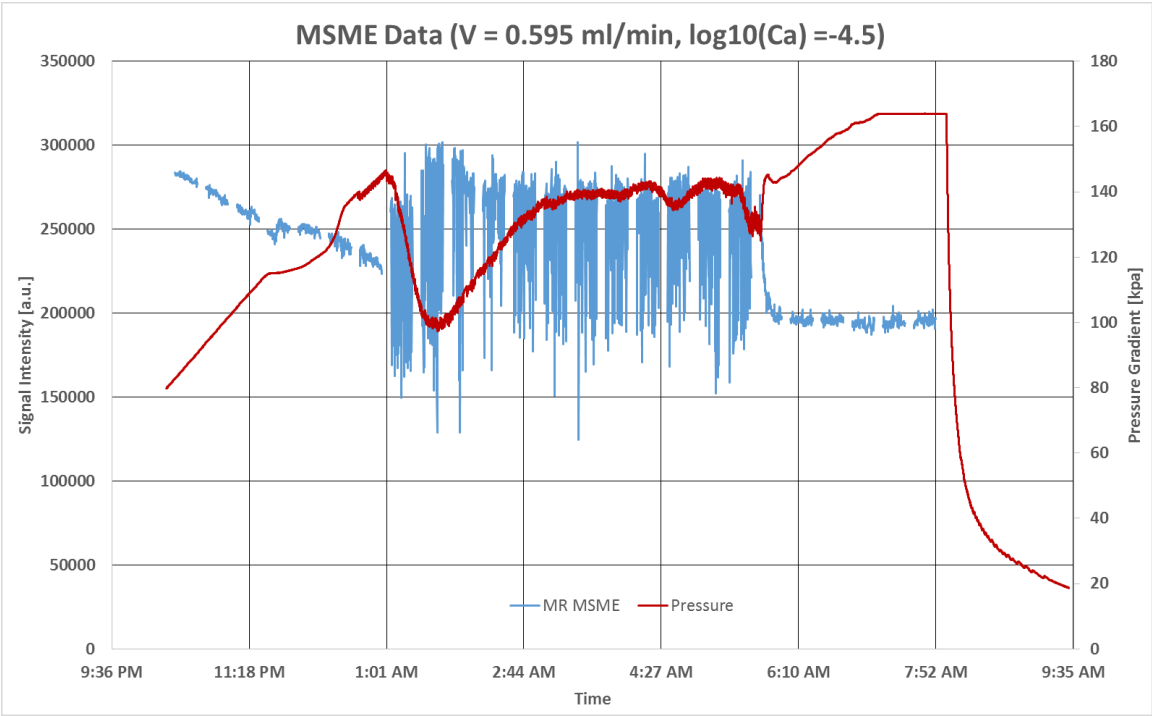
Pressure gradient vs capillary number (preliminary data)



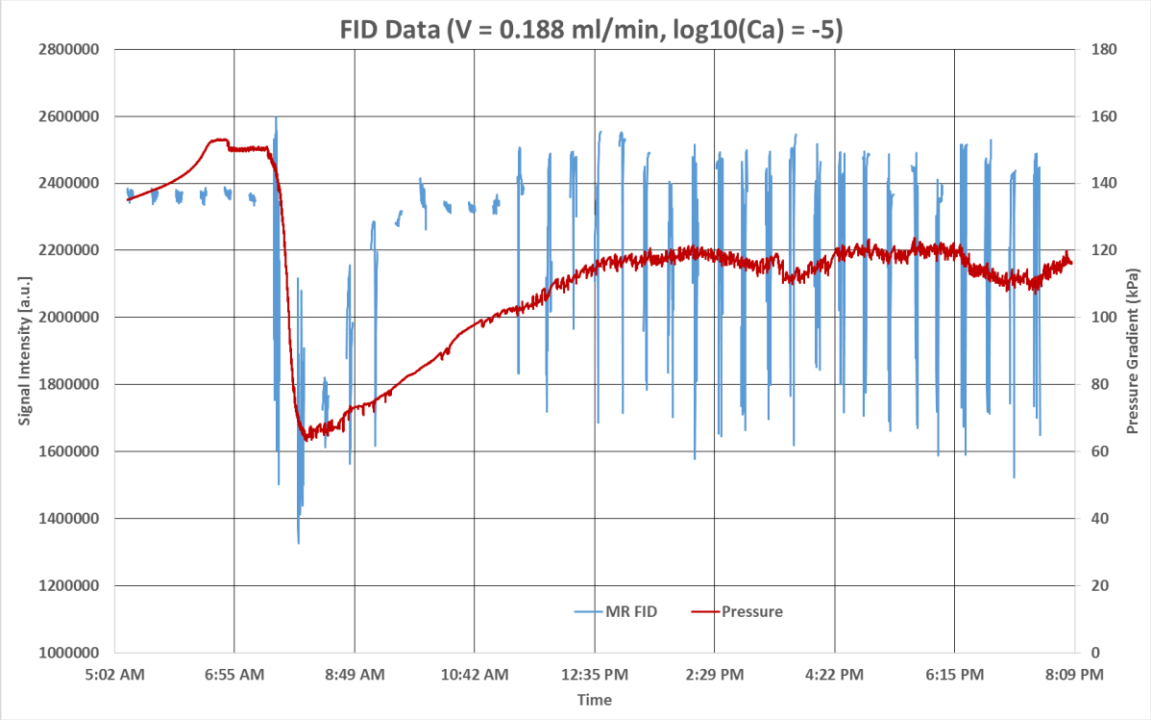
Pressure gradient vs capillary number (recent data)



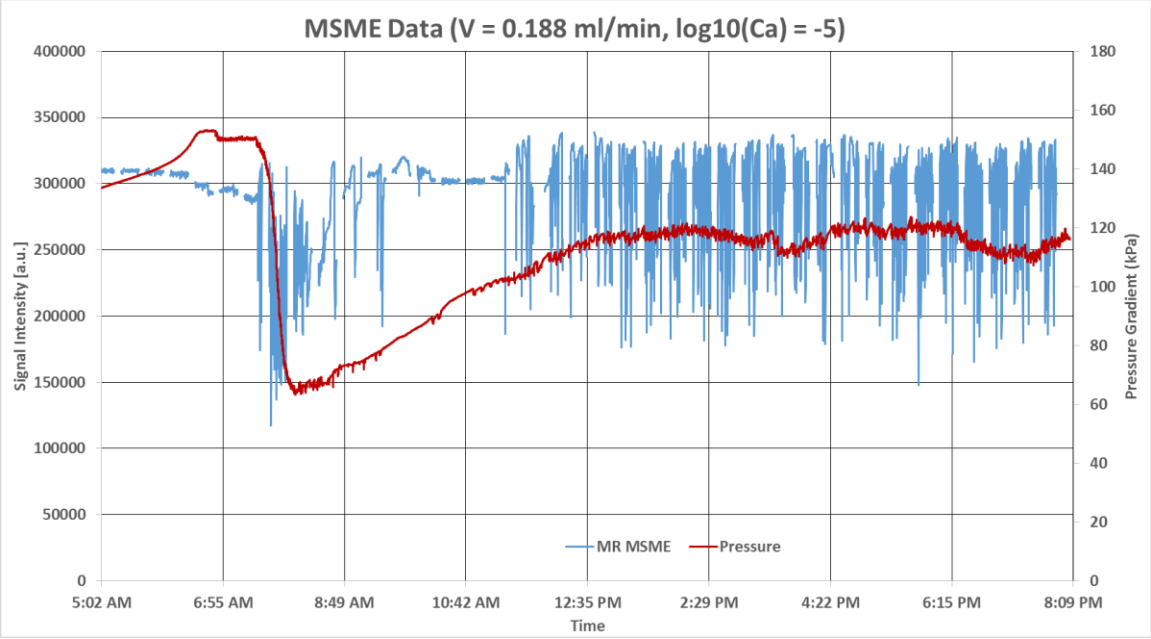
FID and pressure data for flow rate = 0.595 ml/min



MSME and pressure data for flow rate = 0.595 ml/min



FID and pressure data for flow rate = 0.188 ml/min



MSME and pressure data for flow rate = 0.188 ml/min